2023-08-29

Effect of Temperature on Asphaltene Deposition Mechanisms in Vertical Flow

Rodriguez, Maria Alejandra Gomez

UNIVERSITY OF CALGARY

Effect of Temperature on Asphaltene Deposition Mechanisms in Vertical Flow

by

Maria Alejandra Gomez Rodriguez

A THESIS
SUBMITTED TO THE FACULTY OF GRADUATE STUDIES
IN PARTIAL FULFILMENT OF THE REQUIREMENTS FOR THE
DEGREE OF MASTER OF SCIENCE

GRADUATE PROGRAM IN CHEMICAL ENGINEERING

CALGARY, ALBERTA

AUGUST, 2023

Abstract

Deposits of asphaltenes can cause significant problems in oil and gas facilities, pipelines, and wellbores. These deposits can lead to production losses and high treatment costs. To prevent deposition, models are used to predict the risk of asphaltene precipitation. When asphaltenes precipitate at near ambient temperatures, they form glassy particles that adhere to the surfaces of pipes or vessels. Several models have been developed to account for factors such as asphaltene aggregate size and concentration, shear conditions, fluid properties, and surface properties. However, asphaltene deposition at higher temperatures, such as those encountered in deep offshore production, has not yet been thoroughly researched. At higher temperatures, asphaltenes separate from crude oil as part of a heavy liquid phase (liquid droplets) and may deposit differently.

In a recent study, an asphaltene deposition apparatus was commissioned to investigate asphaltene deposition in horizontal laminar flow in both the glassy particle regime (< 100°C) and the liquid droplet regime (> 130°C). Asphaltene deposition in horizontal laminar flow was evaluated in a capillary tube for mixtures of bitumen and *n*-heptane at different flow rates and tube lengths. In the glassy particle regime, precipitated asphaltene particles formed a porous deposit near the inlet of the capillary tube with cycles of deposition and erosion occurring during the flow period. In the liquid droplet regime, asphaltene-rich heavy-phase droplets settled and coalesced to form a continuous heavy-phase layer leading to stratified flow with occasional temporary plugging.

The main objective of the current study was to use the asphaltene deposition apparatus to determine if the deposition mechanisms change in vertical flow. In the glassy particle regime, the deposition mechanism for vertical and horizontal flow was found to be similar. Porous deposits were formed near the inlet of the capillary tube, exhibiting cycles of blockage and blowout. The deposits were localized and occupied a maximum of 40% of the tube volume, with solvent contents of 82 ±10 wt%. The frequency of the blockages was higher in vertical flow compared to horizontal flow.

In the liquid droplet regime, the deposition mechanism was also found to be similar for horizontal and vertical flow. The heavy phase, with solvent contents of approximately 30 wt% in horizontal

flow and about 40 wt% in vertical flow, accumulated throughout the length of the tube. In horizontal flow, the flow regime was interpreted as stratified flow of a light-phase emulsion over a heavy-viscous liquid. In vertical flow, the flow regime was interpreted to begin as dispersed flow with a gradual accumulation of heavy phase at the tube wall leading to core-annular flow. The heavy phase accumulation caused a rise in pressure drop until the holdup reached 80%, then transitioning to slug flow with cycles of pressure build-up and blowout.

Acknowledgment

I am grateful for the chance to be a part of HOPP, the excellent research group led by Dr. Harvey Yarranton. Dr. Yarranton has been an exceptional guide, offering valuable insights and encouragement throughout the research process. His mentorship, devotion, and uplifting words have played a vital role in shaping me as a researcher and completing this work.

Additionally, I would like to express my appreciation to Florian Schoeggl for his generous sharing of knowledge, expertise, and time, providing me with guidance and mentorship during my academic journey. The conversations with him were incredibly fulfilling. Special thanks also go out to Elaine Baydack for her kindness, support, generosity, and thoughtful gestures, such as offering chocolates and candies that always brought a smile to my face. I would further like to extend my gratitude to my friend Nicson Do for sharing his knowledge, for the fulfilling discussions of asphaltene deposition in horizontal flow, and for his patience during my training.

I would like to extend my gratitude to NSERC for funding our research project, and to the University of Calgary for providing us with the necessary facilities to complete it successfully.

I would also like to express my appreciation to my dear friends Carolina, Marcela, Benjamin, Jose, Nicson, Keyner, Nicolas, Camilo, and Kaveh. Their support, encouragement, and engaging conversations have made this experience more enjoyable. Also, I am thankful to my family and David for their understanding, love, and support during challenging moments. They have given me the strength to persevere.

Dedication

To my mom, my family, and David.

Contents

List of Tables

List of Figures

List of Abbreviations and Symbols

Abbreviations

ADEPT	Asphaltene Deposition Tool
CO_2	Carbon Dioxide
ID	Inner Diameter
MRS	Modified Regular Solution
OD	Outer Diameter
SARA	Saturates Aromatics Resins Asphaltenes

Symbols

a_1 , a_2	Fluid specific parameters in effective density correlation
α_{C7}	Viscosity binary interaction parameter
β	Fluid specific parameter that correlates changes in density to changes in viscosity in Expanded Fluid Viscosity Model
β_{C7-Bit}	Density binary interaction parameter between solvent and bitumen
b_1 , b_2	Fluid specific parameters in effective density correlation
B_1	Adjustable constant in empirical fitting equation for asphaltene yield
B	Bitumen specific parameter in density correlation
c_2, c_3	Fluid specific parameters in Expanded Fluid Viscosity Model
C_1	Adjustable constant in empirical fitting equation for asphaltene yield
Ki	Partition coefficient for component i in Modified Regular Solution model
ρ_{bit}	Density of bitumen
ρ_{C7}	Density of *n*-heptane
ρ_{mix}	Density of mixture
ρ_s^0	Fluid specific parameter in Expanded Fluid Viscosity Model
ρ_s^*	Compressed state density
P	Pressure
T	Temperature
μ	Viscosity of the fluid

μ_D	Dilute gas viscosity
v_{bit298}	Specific volume of bitumen at 298 Kelvin
v_{C7298}	Specific volume of *n*-heptane at 298 Kelvin
γ	Activity coefficient
Y	Asphaltene yield
X	Mole fraction x
w_{C7}	Mass fraction of n-heptane in mixture
w_{bit}	Mass fraction of bitumen in mixture

Chapter 1: Introduction

Asphaltenes can precipitate and form deposits in open flow in wellbores, pipelines, and oil and gas facilities. These deposits can lead to production losses if left untreated. Deposition models are used to predict the conditions at which there is a risk of deposition. These models are used to guide chemical treatments. Asphaltene deposition models were designed based on data for asphaltene deposition at near ambient temperatures, where asphaltenes are commonly considered to precipitate as glassy particles. This type of deposition involves the adhesion and accumulation of asphaltene molecules, particles, and aggregates at the surface of a pipe or vessel. Several models have been developed for asphaltene deposition under these conditions, accounting for asphaltene aggregate size and concentration, shear conditions, fluid properties, and surface properties (Vargas *et al.* 2010; Eskin *et al.* 2011). However, asphaltene deposition at the higher temperatures encountered in deep, offshore production has not been rigorously investigated. At higher temperatures, asphaltenes separate from the oil as part of a heavy liquid phase (liquid droplets) rather than as glassy particles, and the mechanisms for deposition may not be the same.

In a recent study, an asphaltene deposition apparatus was commissioned to investigate asphaltene deposition in horizontal laminar flow in both the glassy particle and liquid droplet regimes (Do *et al.* 2022). The apparatus consisted of two transfer vessels, a co-axial nozzle-like static mixer, and a 1.7 mm ID capillary tube test section, all housed in an air bath. Metered positive displacement pumps were used to displace mixtures of bitumen and *n*-heptane through the capillary tube. The differential pressure across a capillary tube (an indicator of asphaltene deposition) was measured during the flow period in a deposition experiment. In addition, the capillary tube was removed after each experiment to measure the mass, solvent content, and location of the deposit.

In the above study, asphaltene deposition in horizontal laminar flow was evaluated for *n*-heptane contents ranging from 65 to 90 wt%, fluid flow rates from 2 and 4 cm^3/min, capillary tube lengths from 3 to 30 cm, and temperatures of 50, 90, and 130°C. It was found that, in the glassy particle regime (50 and 90°C), precipitated asphaltene particles formed a porous deposit near the inlet of the capillary tube with cycles of deposition and erosion during the flow period. In the liquid droplet

regime (130°C), asphaltene-rich heavy-phase droplets settled and coalesced to form a continuous heavy-phase layer, leading to stratified flow with occasional temporary plugging.

The conditions of the study differed from field conditions in several ways. First, the fluid in these experiments differed in composition from the depressurized crude oils encountered in a wellbore. However, the fluid resembled crude oils in the key aspect for this study; that is, it was a hydrocarbon mixture precipitating asphaltenes. The deposition mechanisms are expected to be the same as those applicable to crude oils. Second, the experiments were all in the laminar flow regime. Many field applications involve turbulent flow. However, even in turbulent flow, deposition occurs in the boundary layer of the wellbore where the flow is laminar (Vargas *et al.* 2010; Eskin *et al.* 2012). Hence, a study on laminar flow can offer valuable insights into asphaltene deposition mechanisms. Finally, only horizontal flow was considered. However, flow in wellbores is vertical and upwards. The flow orientation could alter some of the deposition mechanisms.

1.1 Objectives

The main objective of this thesis is to determine if the deposition mechanisms change in vertical flow. The specific tasks are as follows:

- adapt the previously commissioned Asphaltene Deposition Apparatus to evaluate vertical flow conditions.
- measure the pressure drop profiles the mass of the deposit, and the solvent content of the deposit for the glassy particle (50°C) and liquid droplet (130°C) regime for mixtures of bitumen and n-heptane at the following conditions:
    - feed composition from 65 to 90 wt% *n*-heptane,
    - flow rates of 2, 4, and 8 cm^3/min,
    - tube lengths from 3 to 30 cm.
- identify the deposition mechanisms in the glassy particle and liquid deposition regime in vertical flow.
- determine if and how the deposition mechanisms change from horizontal to vertical orientation by comparing the results with those of the previous study done by Do et al. 2022.

1.2 Thesis Structure

The thesis comprises six chapters, and the following five chapters are each briefly described below. Chapter 2 provides a review of the key concepts and mechanisms related to asphaltene deposition (or accumulation), including asphaltene chemistry, and phase behavior related to asphaltene precipitation (or asphaltene-rich heavy phase formation). Mechanisms related to deposition in the glassy-particle regime are discussed including aggregation, adhesion, and deposition. Fundamental concepts of liquid-liquid multiphase flow are explored to understand heavy phase accumulation in the liquid droplet regime.

Chapter 3 outlines the experimental methods used in this thesis. The deposition apparatus is presented and the modifications to the apparatus are discussed. The procedures for the deposition experiments are described. In addition, the property data required for the thesis but obtained from correlations or other sources is summarized.

Chapter 4 presents the results for asphaltene deposition in vertical flow from mixtures of bitumen and n-heptane in the glassy particle regime. The measured pressure drops, deposit mass, and solvent content of the deposit are presented, and the effects of tube length, feed solvent content, and flow rate are discussed. In addition, the deposition results in vertical flow are compared with previous findings for horizontal flow from Do et al. (2022).

Chapter 5 presents the results for asphaltene deposition in vertical flow for mixtures of bitumen and n-heptane in the liquid droplet regime. As in Chapter 4, the measured pressure drops, deposit mass, and solvent content of the deposit are presented, and the effects of tube length, feed solvent content, and flow rate are discussed. Finally, the deposition results in vertical flow are compared with previous findings for horizontal flow from Do et al. (2022).

Chapter 6 summarizes the key findings from this thesis and recommendations for future studies.

Chapter 2: Literature Review

In this chapter, the concepts related to asphaltene deposition are reviewed, starting with the chemistry of asphaltenes. The phase behavior related to asphaltene precipitation is discussed particularly the distinction between glassy-particle and liquid asphaltene-rich phases. Deposition in the glassy particle regime involves aggregation and adhesion, and therefore these topics are reviewed. Then, deposition in the glass particle regime is discussed in more detail. Deposition in the liquid droplet regime is essentially the accumulation of a heavy liquid phase. Therefore, the fundamentals of liquid-liquid multiphase flow are reviewed. Finally, the accumulation of asphaltene-rich phases is discussed.

2.1 Crude Oil and Asphaltene Chemistry

2.1.1 Crude Oil

Crude oils are liquid petroleum consisting of a wide range of hydrocarbons and other compounds containing variable amounts of sulfur, nitrogen, oxygen, and metals. Crude oils range widely in their volatility, specific gravity, and viscosity. They are an important energy source and raw material to produce various products, including fuels, lubricants, and petrochemicals (Speight, 2006).

Crude oil quality is defined by its boiling point, viscosity, and specific gravity (SG) relative to water. Crude oil is classified as extra light, light, medium, heavy, and extra heavy depending on its SG (Ramirez-Corredores, 2017), as shown in Table 2.1. Properties for each class of crude oil are also provided in Table 2.1. Heavy oil is an unconventional oil characterized by high viscosity, high density, a low H/C ratio, and high contents of asphaltenes, resins, and sulfur (Speight, 2019).

Crude oil has many compounds and isomers, making crude oil analysis impractical with traditional chemical characterization techniques. Several separation techniques and methodologies have been developed to characterize crude oils into a set of fractions with definable properties. These methods include gas chromatography (gives carbon number fractions or simulated boiling fractions), distillation (boiling cuts), and SARA fractionation (chemical families). SARA fractionation is often applied to heavy oils and the heavy ends of conventional oils.

SARA fractionation separates the oil into four main chemical families: saturates (S), aromatics (A), resins (R), and asphaltenes (A). The asphaltenes are separated by precipitation, and the other fractions by adsorption (liquid chromatography). The saturate fraction contains only aliphatic compounds such as paraffin and naphthene. The aromatic fraction contains structures with at least one aromatic group, which may also incorporate saturated and heteroatomic groups. Saturates and aromatics are the lowest molecular weight fractions of crude oil. The resins and asphaltenes are similar to aromatics but have progressively higher molecular weight, aromaticity, polarity, heteroatom, and metallic content (Gray, 2015). This thesis is concerned with asphaltenes.

Table 2.1. Selected properties of different types of crude oils.

Classification	*API Gravity (°)*	*Viscosity mPa·s*	*Density g/cm3*	*Mean Boiling Point (°C)*
Extra Light	>40	< 2	< 0.83	< 350
Light	30 - 40	2 – 10	0.87 – 0.83	250 - 450
Median	20 - 30	10 – 100	0.92 – 0.87	300 – 500
Heavy	10 - 20	100 - 5000	1.0 – 0.92	400 – 600
Extra Heavy	<10	>5000	> 1.0	> 500

2.1.2 Asphaltenes

Asphaltenes are defined as the fraction of crude oil soluble in an aromatic solvent (such as toluene) but insoluble in a paraffinic solvent (such as pentane or heptane). They are the highest molecular weight, densest, most aromatic, most polar, and most heteroatomic components of crude oils. Their content in crude oils ranges from less than a percent to as much as 20% (Shirokoff, *et al*., 1997). Even at low contents, they are the most troublesome oil fraction in many ways. They can be destabilized during oil production due to temperature, pressure, and oil composition variations (Mofidi and Edalat, 2006; Eskin *et al*., 2016; Kord *et al*., 2014). The precipitated asphaltenes can cause formation damage and deposit in wellbores and surface facilities. Asphaltenes also tend to stabilize water-in-oil emulsions (Czarnecki *et al.*, 2012) and are coke precursors in upgrading processes (Ashtari *et al*., 2016).

The average elemental composition and properties of asphaltenes vary relatively little between oils (Ramirez-Corredores, 2017; Speight, 2004). The carbon content of asphaltenes from different sources ranges from 82 to 88 wt% and their hydrogen/carbon (H/C) ratio varies between 0.5% and 1.15%. (Speight and Andersen 1999; Speight 2004). There is greater variation in the heteroatom content with oxygen ranging from 0.3 to 4.9 wt%, sulfur from 0.3 to 10.3 wt%, and nitrogen level from 0.6 to 3.3 wt% (Fahim *et al*., 2009; Speight, 2004). The average density of asphaltenes ranges from approximately 1100 to 1200 kg/m³ depending on the source and how the asphaltenes are extracted from the oil (Gray *et al.*, 2021).

Since asphaltenes are a solubility class rather than a single chemical compound, their molecular compositions and properties are distributed (Gray *et al*., 2021). For example, Chacon *et al*., (2020) demonstrated that the atomic ratios of asphaltene fractions differed significantly from the mean ratios of whole asphaltenes. In another example, Barrera *et al.*, (2013) found that the density distribution of asphaltenes from a Western Canadian bitumen with an average density of 1176 kg/m³ ranged from approximately 1100 kg/m³ for the most soluble asphaltenes to 1200 kg/m³ for the least soluble asphaltenes.

It has proven challenging to measure the molecular weight of asphaltenes, with notable inconsistencies in the results (Mullins, 2011; Gray, 2015). The main issue is that asphaltenes self-associate and reported molecular weights often include the contribution of the aggregates. Recent data suggest that asphaltene monomer molecular weights range from 400 to 1000 g/mol (Mullins, 2008; Yarranton *et al*., 2013).

Asphaltenes contain hundreds of thousands or more different chemical species (Chacon-Patiño *et al.*, 2018). Hence, it is challenging to analyze their molecular structure, even though many analytical techniques have been applied. The molecular structures of asphaltenes and their state in the oil are still a topic of debate. In general, asphaltenes consist of condensed polynuclear aromatic groups which incorporate some heteroatomic species (Semple *et al*., 1989). The polynuclear groups have some aliphatic side chains and can be linked via an aliphatic chain. Asphaltene molecules are thought to consist of islands (sometimes called continental) and/or archipelago-type structures, as shown in Figure 2.1. The island model consists of a polycyclic aromatic core with

alkyl side chains located at the periphery. The archipelago model consists of several smaller polynuclear aromatic cores linked by alkyl groups and with alkyl side chains at the periphery. The continental structure is the traditional view but is inconsistent with the distribution of reaction products obtained from asphaltenes (Gray *et al*, 2011; Strausz and Lown, 2003).

(a) (b)

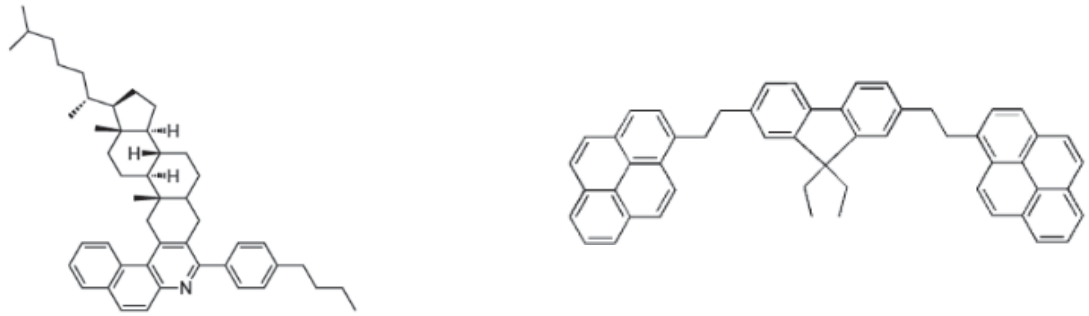

Figure 2.1. Example of asphaltene molecular structures: a) island (continental) model; b) archipelago model Adapted from Sabbagh *et al*. (2011).

It has been proven that asphaltenes tend to self-associate and create molecular nanoaggregates within the oil. Numerous techniques have been employed to investigate asphaltene association including vapor pressure osmometry (Yarranton *et al*., 2000; Barrera *et al.,* 2013), small-angle neutron scattering (Roux *et al.,* 2001), and small angle x-ray scattering (Eyssautier *et al.,* 2012). The individual nanoaggregates can range in size from dimers to structures of approximately 50,000 g/mol. The average nanoaggregate molecular weights of asphaltenes extracted from the crude oil range from approximately 3000 to 10000 g/mol based on vapor osmometry (Yarranton et al., 2013; Barrera *et al.,* 2013). The diameter of the aggregates is in the order of 10 to 50 nm (Yarranton *et al.,* 2013).

The self-association does not necessarily involve all asphaltene species and may be between specific types of molecules present in the asphaltene fraction (Moir, 2018; Mullins *et al.,* 2008; Mullins *et al.,* 2012). For example, Barrera *et al.* (2013) found that 90 wt% of the asphaltenes in a Western Canadian bitumen existed as nanoaggregates with similar densities, while the remaining 10 wt% were individual molecules (Gray *et al.,* 2021; Barrera *et al.,* (2013).

The self-association mechanism remains unclear. One view is that asphaltenes self-associate into colloidal stacks held together with π-π bonds between aromatic cores (Dickie and Yen, 1967). This view is consistent with the continental structure. Another view is that asphaltenes form oligomer-like macromolecular structures via various mechanisms including π-π stacking, acid-base interactions, and hydrogen bonding (Gray *et al.*, 2011; Agrawala and Yarranton, 2001). This view is consistent with both continental and archipelago structures.

2.2 Asphaltene-Related Phase Behavior

2.2.1 Observed Phase Behavior

Asphaltene precipitation from crude oils can occur with a change in pressure, temperature, or composition. For example, asphaltenes can precipitate from undersaturated light oils upon depressurization or after gas injection (Zanganeh *et al.,* 2012; da Silva Oliveira *et al.,* 2014). They can precipitate from conventional oils during CO2 floods (Parsaei *et al.,* 2020). They can precipitate when heavy oils are mixed with an incompatible solvent, such as an n-alkane (Tharanivasan *et al.,* 2012) and in refineries if incompatible oils are blended (Bambinek *et al.,* 2022).

Asphaltene phase separation is commonly termed "precipitation" because the asphaltene-rich phase often appears as glassy particles. However, the asphaltene-rich phase can also appear as liquid droplets or in a transition between the glass and liquid morphology. The nature of the asphaltene-rich phase depends on the temperature, pressure, type of solvent, and solvent content of the system (Sirota, 2005; Johnston *et al.,* 2017).

In this thesis, asphaltene precipitation is induced by adding an incompatible solvent (n-heptane). In mixtures of heavy oil diluted with n-pentane or higher carbon number n-alkanes at temperatures up to approximately 90°C, the asphaltene-rich phase also appears as glassy particles, as shown in Figure 2.2a. However, the asphaltene-rich phase reaches a glass transition at higher temperatures and appears as liquid droplets at approximately 130°C, as shown in Figure 2.2a (Johnston *et al.,* 2017). Between 90 and 130°C, the asphaltene-rich phase transitions from glassy particles to fully liquid. In less compatible solvents such as propane and n-butane, the glass transition occurs at lower temperatures and solvent contents (Mancilla-Polanco *et al.,* 2019; Perez Claro *et al.,* 2019).

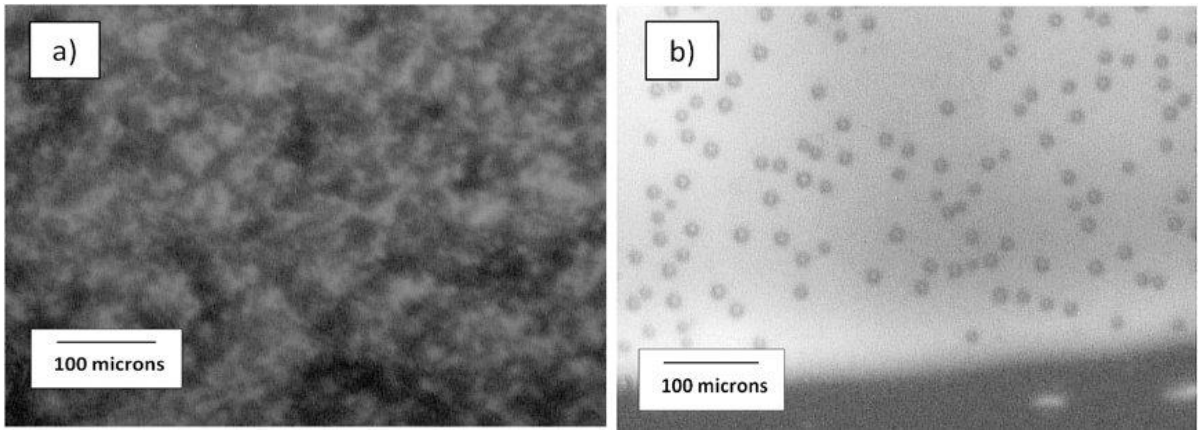

Figure 2.2. Asphaltenes precipitated from bitumen diluted with n-pentane, images captured by HPM: a) 23°C (glassy particles); b) 165°C (liquid droplets) (Johnston *et al.*, 2017).

2.2.2 Asphaltene Precipitation Models

Models of asphaltene precipitation can be divided into two groups: the colloidal approach and the solubility approach. The colloidal approach assumes asphaltenes to exist in the crude oil as colloidal particles stabilized by resins absorbed on their surfaces. Asphaltene precipitation is considered to be caused by resin desorption (Sanchez and Mansoori, 1997). This approach is inconsistent with the liquid phase behavior observed at higher temperatures. The solubility approach assumes that asphaltenes are dissolved in the crude oil and phase separate with a conventional liquid-liquid equilibrium (Ting *et al.*, 2003). This approach is consistent with the observed phase behavior and is the basis of most asphaltene precipitation models. The two main solubility approaches to asphaltene precipitation are equations of state (EoS) and the Modified Regular Solution (MRS) model.

Equations of State

Classic cubic equations of state (CEoS) are commonly used because they are well-established in the oil industry, are available in process and reservoir simulators, and can describe vapor-liquid and liquid-liquid equilibria (Castellanos Diaz *et al.*, 2011). The limitation of the CEoS is its inability to consider the effect of polar or association effects like hydrogen bonding. While the CEoS can match phase boundaries, they provide poor predictions of the phase compositions in the liquid-liquid region. Cubic-Plus Association (CPA) EoS introduces additional terms to a CEoS to

describe the self-association and cross-association between molecules (Li and Firoozabadi, 2010; Arya *et al.*, 2016). The CPA model can capture asphaltene yields and phase boundary data but loses accuracy near and above the critical temperature of the solvents (Zhang *et al.*, 2003).

The Statistical Association Fluid Theory (SAFT) equation of state estimates the Helmholtz energy of a system as a departure from the ideal gas value (Chapman, 1989). The departure function, also known as the residual Helmholtz energy, accounts for contributions arising from short-range and long-range molecular interactions, the formation of chemical bonds, and molecular association. The SAFT EoS has been successfully applied to model the vapor-liquid equilibria, density, and the onset of asphaltene precipitation for crude oils.

Modified Regular Solution Model

The Modified Regular Solution (MRS) approach has been used for modeling asphaltene precipitation from n-paraffin-diluted heavy oil (Yarranton and Masliyah, 1996; Alboudwarej *et al.*, 2003; Akbarzadeh *et al.*, 2005; Ramos-Pallares and Yarranton, 2020). This model calculates the activity coefficient of a component in a mixture from an enthalpic contribution arising from a regular solution and an entropic contribution caused by mixing molecules of different sizes. The MRS model assumes that, at a solvent content above the onset of asphaltene of precipitation, the system is in liquid-liquid equilibrium where components partition between two phases: a light phase and a heavy phase. The first versions of the MRS model assumed that only asphaltenes and resins partition into the heavy phase, but recently Ramos-Pallares and Yarranton, (2020) extended the MRS model to account for the partitioning of all components into the heavy phase. The updated model can predict the mass and compositions of the light and heavy phases formed in mixtures of an n-alkane and bitumen. However, these models are limited to liquid-liquid equilibria.

2.3 Asphaltene Aggregation

2.3.1 Observed Asphaltene Aggregation

When asphaltenes precipitate as glassy particles, the particles tend to aggregate. Asphaltene aggregation has been studied from mixtures of n-alkanes with various model oils and as a function of the precipitant (incompatible solvent) content, shear, and temperature. The size distributions of asphaltene aggregates have been examined with laser time transition methods, laser reflectance

technique focused-beam reflectance measurement (FBRM), confocal laser-scanning microscopy (CLSM), and micrographic methods (Rastegari *et al.,* 2004; Calles *et al.,* 2008); Hoepfner *et al.,* 2013; Seifried *et al.,* 2013; Duran *et al.,* 2018). These studies have shown that the precipitated asphaltenes are first observed as primary particles (approximately one μm diameter particles). These particles tend to aggregate over seconds to hours to form large porous structures with diameters up to several hundred micrometers. Figure 2.3 shows an example of asphaltenes aggregates in bitumen diluted with n-heptane.

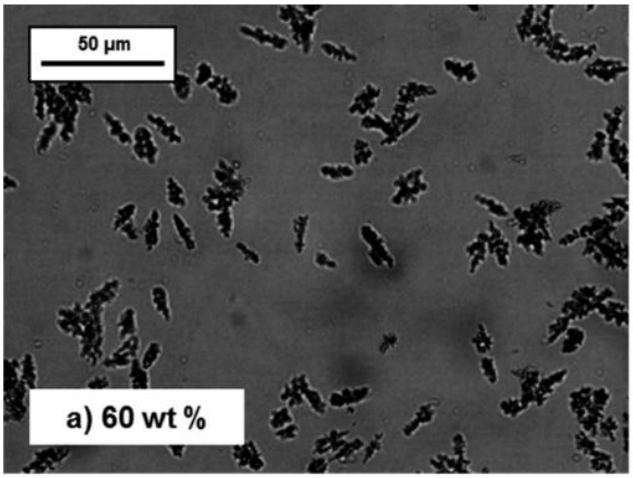

Figure 2.3. Asphaltene aggregates from n-heptane-diluted Western Canadian bitumen (Duran *et al.,* 2018).

The asphaltene aggregates are considered to be fractal structures (Hoepfner *et al.,* 2013). The fractal dimension quantitatively measures how the primary particles occupy the aggregate interior space. For instance, a fractal dimensions close to 2 indicates either a planar structure or a highly porous structure (Duran *et al.,* 2018). As the fractal dimension increases, the structure become more three-dimensional and less porous. The two-dimensional fractal dimensions of cross-sections of asphaltenes aggregates can be determined through optical microscopy (Rastegari *et al.,* 2004; Rahmani *et al.,* 2005; Duran *et al.,* 2018). This method involves taking images of individual flocs and correlating their area (or diameter) with their perimeter. Fractal dimensions obtained through the micrographic method range from 1.3 to 2.8 (Rastegari *et al.,* 2004; Rahmani *et al.,* 2005; Duran *et al.,* 2018). Duran *et al.,* (2018) determined the three-dimensional fractal dimension from the

sediment volume of settled aggregates. They found dimensions between 2.55 and 2.85 depending on the particle concentration.

Above the onset of asphaltene precipitation in n-heptane bitumen, the average diameter and the fractal dimension of the asphaltene aggregates increased with increasing n-heptane content until the maximum primary particle concentration was reached at an n-heptane content of 70 to 80 wt% (Duran *et al.,* 2018). The increase in fractal dimension and images of the aggregates suggested that the aggregates were becoming less planar and more three-dimensional. Above the maximum concentration, the average diameter remained nearly constant, but the fractal dimension decreased with increasing n-heptane content. The decrease in fractal dimension and images were consistent with more porous aggregates. Ferworn *et al.* (1993) also found that the average size of asphaltene aggregates reached a plateau as solvent content increased in a series of both light and heavy crude oils diluted with n-heptane. The maximum number of particles and the largest diameters occurred in solvents with lower molecular weight (Calles *et al.,* 2008; Seifried *et al.,* 2013).

Asphaltene aggregation is partially sensitive to shear. Soleimani-Khormakala *et al.,* (2018) observed that the impact of fluid shear on the fragmentation of asphaltene aggregates was greater than its effect on their aggregation. They found that the average diameter of asphaltenes aggregates reached a steady state size due to a balance of aggregation versus fragmentation kinetics. Fragmentation was favored at higher shear rates, leading to more but smaller aggregates (Rahmani *et al.,* 2003; Rahmani *et al.,* 2004). Nguyen *et al.* (2020) confirmed that applying shear stress increased the aggregation and fragmentation kinetics of asphaltene particles. The aggregation process dominated at early times and caused a decrease in fractal dimension of the particles leading to a higher diameter and effective volume fraction and the diameter of the asphaltene aggregates over time. At still longer times, the shear stress caused the larger asphaltene clusters to break into smaller fragments. This breakage process reduced the diameter of asphaltene aggregates, and their volume fractions approached an equilibrium size.

Duran *et al.* (2018) observed that an increase in shear rate led to a decrease in the initial aggregate size. However, after a few minutes and at lower n-heptane contents, the asphaltene aggregate size changed negligibly over time at the investigated shear rates. In other words, the compact

aggregates formed at low n-heptane contents were resistant to fragmentation. At higher n-heptane contents, the porous aggregates formed at these conditions could be fragmented under sufficient shear. However, they did not reaggregate even at low shear rates. Duran *et al.* (2018) showed that the precipitated asphaltenes were sticky for only a few minutes after precipitation, consistent with the observation that asphaltenes only form aggregates when they first precipitate.

2.3.2 Asphaltene Aggregation Models

Asphaltene aggregation is commonly modeled based on the population balance approach originally proposed by Smoluchowski (Rahmani *et al.,* 2003; Rastegari *et al.,* 2004; Solaimany-Nazar and Rahimi; 2008; Torkaman *et al.,* 2018; Soleimani-Khormakala *et al.,* 2018). A population balance model predicts a distribution of aggregates in terms of the number of primary particles in the aggregate. The model assumes a dynamic equilibrium between the rate of aggregation and fragmentation of the aggregates, implying that an increment in shear rate would break the flocs but the flocs would be restored if the original shear conditions were reestablished. At steady conditions, a constant average aggregate size is predicted.

Solaimany-Nazar and Rahimi (2008) developed a model to predict the size distribution of asphaltene aggregates in a heptane-toluene mixture under shear. The mass fractal dimension was modeled by a time-dependent function, and the average diameter of aggregates had a maximum value beyond which the fragmentation rate overcame the aggregation. Maqbool *et al.* (2011) developed a population balance model to simulate the growth of asphaltenes aggregates in the presence of n-heptane from the nanometer-scale primary particles to micrometer-sized aggregates. Duran *et al.* (2019) adapted the model by Maqbool *et al.* to account for initial rapid asphaltene precipitation observed at early times and the sharp increase in aggregate size observed almost immediately upon contact with the precipitant. The adapted model successfully matched both yield and aggregate size distribution over time.

2.4 Asphaltene Adhesion

The force attaching asphaltene particles to the wall is typically termed adhesion. Strictly speaking, the tube surface is almost certainly initially coated with a molecular layer of adsorbed asphaltenes

(Alboudwarej *et al.,* 2005); hence, the attachment force is more accurately termed a cohesive force. Here, the term adhesion is retained to be consistent with the literature.

2.4.1 Observations of Asphaltene Adhesion

In the glassy particle regime, asphaltene aggregate formation and deposition involves asphaltene adhesion between asphaltene molecules and between asphaltene molecules and/or aggregates and surfaces. Adhesion is driven by various forces, including van der Waals, Coulombic, and repulsive exchange interactions (Murgich, 2002; Adams, 2014). Although individually, these forces are quite weak, they can be quite strong when combined (Gray *et al.*, 2011). Asphaltene adhesion has been examined in the laboratory with different techniques such as atomic force microscopy (AFM), surface force apparatus measurements (SFA), quartz crystal microbalance measurements (QCM), X-ray photoelectron spectroscopy tests, and UV-vis spectrophotometry (Ducker *et al.*, 1992; Alboudwarej *et al.*, 2005; Xie and Karan, 2005; Israelachvili *et al.,* 2010).

The behavior of asphaltenes in crude oil depends largely on the oil composition but also on the molecular interactions between asphaltenes and asphaltenes with the surrounding medium. In an aqueous solution, Abraham *et al.* (2002) observed that a repulsive force developed over time between asphaltene and silica surfaces, suggesting that there were molecular rearrangements at the asphaltene-water interface. Increasing the salinity decreased the range and magnitude of the repulsive force, suggesting an electrostatic nature for these forces. Increasing pH increased the range and magnitude of the repulsive asphaltene-silica interactions, implying the presence of pH-dependent ionizable groups on the surface.

In an organic medium that is a good solvent for asphaltenes such as toluene, it was found that asphaltene films experience a weak attraction to each other after contact during the initial separation. However, they repeal each other at long distances. The repulsive interaction forces between asphaltene films originate from a steric force sufficient to overcome the attractive van der Waals forces (Wang *et al.*, 2010; Natarajan *et al.,* 2014; Zhang *et al.,* 2016). In a solvent like n-heptane, Wang *et al.* (2010) found that the adhesion force between asphaltenes was almost null and rapidly increased with increasing n-heptane content. At intermediate n-heptane contents, nearly constant adhesion was found. Similarly, Zhang *et al.,* (2016) showed that interactions

between asphaltenes change from pure repulsion in a good solvent (toluene) to weak adhesion in a poor medium (heptol) and that the adhesion force increased with increasing n-heptane content.

The attraction between asphaltene films can be characterized based on van der Waals forces. The adhesion force gradually weakens over time, suggesting that asphaltene molecules on the surface reorient themselves such that steric effects increase between the approaching asphaltene films. Compared to asphaltene films in toluene, those in n-heptane are more rigid and less swollen. When the surrounding environment changes from miscible to partially miscible, the interactions between asphaltene films change from repulsive to adhesive.

Adsorption of asphaltenes on various solid surfaces has been explored in the literature, including minerals, metals, and stainless-steel surfaces. The adsorption of asphaltenes on metals depends on the type of surface, the type or source of the asphaltenes, the temperature, the asphaltene concentration, and the liquid medium (Alboudwarej *et al.,* 2005; Dudasova *et al.,* 2008; Balabin *et al.,* 2011; Adams, 2014; Ortega-Rodriguez *et al.,* 2016). Alboudwarej *et al.* (2005) determined that surface morphology is critical in defining a metal's adsorption capacity. Asphaltenes preferentially adsorb onto the following metals in decreasing order: gold > stainless steel> iron > aluminum (Xie and Karan, 2005; Alboudwarej *et al.,* 2005). However, Balabin *et al.* (2011) reported a different value for the iron absorbed mass density, being higher than stainless steel and aluminum, concluding that the results can be affected by the solvent used and the diffusion effects due to the dispersed structure of the adsorbed material.

Alboudwarej *et al.* (2005) found that asphaltene adsorption on metals follows Langmuir (Type I) isotherms, indicating that asphaltenes saturated the surface area available for adsorption as a monolayer. However, multilayer asphaltene adsorption has been observed in QCM experiments at later times (Xie and Karan, 2005; Abudu and Goual, 2009; Zahabi *et al.,* 2012). An increase in the concentration of asphaltenes results in a proportional increase in the amount of asphaltene adsorption onto metal and mica surfaces (Xie and Karan, 2005; Rudrake *et al.,* 2009; Natarajan *et al.,* 2014). The initial adsorption rate is diffusion controlled and is higher at higher asphaltene concentrations, leading to a shorter time to reach equilibrium. In addition, the amount of asphaltene adsorption increases when the surrounding environment becomes a poorer solvent for asphaltenes.

Several studies have reported that asphaltene adsorption decreased with increasing temperature. Temperature changes may influence the asphaltene aggregate size in the solution altering their spatial disposition over the adsorbent surface and decreasing their intermolecular forces (Alboudwarej *et al.,* 2005; Cortes *et al.,* 2016). However, other studies have reported that temperature does not affect overall adsorption and is only important at short reaction times (Xing *et al.,* 2010).

2.4.2 Asphaltene Adhesion Models

Xie and Karan (2005) developed a thermodynamic framework that models the asphaltene adsorption onto QCM crystals and considers the diffusion-convective mass transport and adsorption phenomenon. The initial adsorption process is controlled by the diffusion of asphaltenes from the bulk solution to the surface. However, comparing their findings with literature values, the apparent diffusion coefficient of asphaltenes in toluene solutions at early times and the estimated diameter of the asphaltenes particles from this approach are inconsistent. It was concluded that QCM measurements are unreliable for this purpose (Abudu and Goual, 2009; Zahabi and Gray, 2012).

Later, Liu *et al.* (2020) studied the asphaltene adsorption from crude oil onto stainless-steel surfaces using QCM-D with a dissipation technique. Their model is based on a two-step adsorption ZG model (Zhu and Gu, 1990). First, asphaltene monomers adsorb onto the substrate, and second, asphaltene molecules adsorb onto the previously adsorbed molecules and form nanoaggregates. The ZG model proved accurate in predicting the amount of molecules adsorbed on the surface (Mendoza de la Cruz *et al.,* 2009). Liu *et al.* (2020) implemented the ZG model fitted with the experimental data, the maximum surface coverage, and the adsorption parameters to find the adsorbed mass from asphaltene solutions of crude oil in pure toluene as a function of asphaltene concentrations.

Ortega-Rodriguez *et al.* (2016) used AFM to determine the adhesion force of asphaltenes to metallic surfaces of aluminum (Al) and iron (Fe). They also developed a calculation method for the force of adhesion and interaction between spherical asphaltenes particles and iron and aluminum metallic surfaces. This method was based on Lindhard's continuum planar potential

(CPP) approximation that incorporates the effect of the solvent and has no fitting parameters. The experimental results were in good agreement with the modeled data.

2.5 Asphaltene Deposition in the Glassy Particle Regime

2.5.1 Observed Asphaltene Deposition

Asphaltene deposition has been studied in different geometries such as capillary tubes, the Taylor-Couette cell, packed bed column, porous media, and micromodels. Most studies have used capillary tubes or the Taylor-Couette cell. In the capillary tube method, asphaltene deposition is induced by mixing the n-alkanes with the crude oil samples. Deposition on the inner surface of the metallic pipe decreases the cross-sectional area of the capillary. The flow restriction can be monitored by measuring the pressure drop across the capillary tube (Broseta *et al.,* 2000; Wang *et al.,* 2004). The Taylor-Couette cell consists of two concentrical cylinders. The inner cylinder rotates and particles deposit on the outer immobile wall. At the end of the experiment, the free oil is drained, deposit is recovered using dichloromethane, and its mass determined (Eskin *et al.*, 2001; Akbarzadeh *et al.,* 2011). Both horizontal and vertical flow configurations have been examined with these techniques.

<u>Horizontal Flow</u>

Broseta *et al.* (2000) applied the capillary tube method to measure asphaltene deposition. They concluded that it is an effective method to investigate asphaltene deposition on the capillary walls due to their sensitivity in detecting changes in pressure. This method allows the detection of deposits in fluid with a very low asphaltene content (0.04 wt%). They found that the percentage of asphaltenes deposited was 5% of the total quantity injected with a 4 μm/hour deposition rate. They hypothesized that the asphaltenes aggregates had low diffusion coefficients leading to low deposition rates.

Wang *et al.* (2004) investigated asphaltene deposition in a capillary tube from mixtures of stock-tank and n-alkanes. The considered the effects of temperature (20 to 60°C), the degree of asphaltene instability, and the precipitant molar volume. They concluded that the deposition rate was greater for higher carbon number n-alkanes than for lower carbon numbers. The rate of deposition was unaffected by flow rate and capillary tube length.

Nabzar and Aguilera (2008) investigated the formation of asphaltene deposits in porous media and capillary tubes. They found a relation between the asphaltene deposition rate and the flow rate, which was not influenced by the origin of the crude oil. They also determined that there are critical shear conditions under which asphaltenes will not deposit. Below this critical point, the asphaltene deposition follows diffusion-limited deposition, but above this critical point, the shear rate begins to impede multilayer deposition.

Hoepfner *et al.* (2013) investigated asphaltene deposition in capillary tubes containing crude oils and n-heptane. They observed that sub-micrometer asphaltene aggregates likely dominate asphaltene deposits and that large and mature aggregates do not contribute to deposition. In a subsequent study, Chaisoontornyotin *et al.* (2016) reported that similar asphaltene deposition behavior was obtained using various n-alkanes, normalizing the differences by adjusting for asphaltene solubility, mixture viscosity, and capillary geometry.

Do *et al.* (2022) used a 1.7 mm ID capillary flow apparatus to investigate asphaltene deposition in horizontal laminar flow for mixtures of bitumen and n-heptane, with n-heptane contents ranging from 65 to 90 wt%, fluid flow rates from 2 and 4 cm^3/min, capillary tube lengths from 3 to 30 cm, and temperatures of 50, 90, and 130°C. After each experiment, they removed the capillary tube to measure the deposit's mass, solvent content, and location. They found that, at 50 and 90°C, precipitated asphaltene particles formed a porous deposit near the inlet of the capillary tube with cycles of deposition and erosion occurring during the flow period. At higher temperatures, the asphaltenes phase separated as a liquid, as discussed in Section 2.6.

Vertical Flow

Akbarzadeh *et al.* (2009, 2012) employed a flow-through variation of the Taylor-Couette cell to quantify the rate of asphaltene deposition under different temperatures and pressure conditions using oil samples from a Gulf of Mexico oil field. They examined the influence of various factors, including shear, the residence time of fluid in the cell, pressure, and chemical injection, on asphaltene deposition rates. In contrast to batch experiments, flow-through experiments showed a continuous increase in deposits over time due to the fresh oil passing through the deposition cell.

Also, the deposition rate has a strong shear dependency; more deposit was formed at a lower shear rate.

Vilas Boas Favero *et al.* (2016) used a packed bed of stainless-steel beads over which a mixture of oil and n-heptane is flown and the asphaltene deposit monitored. After a specified amount of run time, the column was drained, and the retained asphaltenes were collected by injecting chloroform through the bed and quantified after evaporating the chloroform. It was found that the asphaltene deposition process can be explained by a diffusion-limited deposition of nanoparticles. A higher concentration of unstable asphaltenes led to a higher rate of asphaltene deposition.

Later, Kuang *et al.* (2018) used a multi-section packed bed system to study asphaltene deposition on metallic surfaces at high temperatures and pressures. They found that the temperature could impact the deposition rate due to changes in the solubility of asphaltenes, the diffusion of the precipitated asphaltenes, and the formation of the aged asphaltenes. Also, the deposition rate was greater for asphaltenes destabilized by n-pentane than n-heptane.

2.5.2 Asphaltene Deposition Models

Vertical Flow

Ramirez-Jaramillo *et al.* (2006) developed a simple deposition model based on the assumption that molecular diffusion and shear removal are competing mechanisms that determine the radial diffusion rate and the deposition rate of asphaltene particles at a wellbore surface. They considered both turbulent and laminar flow. In their analysis, the radial diffusion rate was related to the radial temperature gradient which induced a radial concentration gradient in the liquid phase. One limitation of this model is that it did not consider particle growth.

The Asphaltene Deposition Tool (ADEPT) Model is a more rigorous model developed using data from capillary experiments where the fluid flow was in a laminar regime. This model includes sub-models describing particle precipitation, aggregation, transport, and deposition on the wall (Vargas *et al.*, 2010). The ADEPT model assumed that only primary asphaltene particles participate in the deposition process because inertia causes the aggregates to be carried away by the fluid flow, as was observed experimentally. Later, Kurup *et al.* (2011) modified the existing ADEPT simulator

Vargas *et al.* (2010) to effectively predict the deposition in capillary flow experiments and simulate the turbulent flow observed in the field. This modified model considers an axial dispersion instead of the diffusivity constant used in the original version. The axial dispersion includes Brownian and turbulent diffusion, which enables the successful application of this model for turbulent flow conditions. The field application of the modified ADEPT model was implemented by Kurup *et al.* (2012) in a subsea pipeline in the Gulf of Mexico. The deposition simulator correctly identified the location of the peak deposition and the calculated pressure drops in the wellbore were in the range of the field-measured pressure drops.

Another asphaltene deposition model was developed for a Couette device (Eskin *et al.*, 2009; Eskin *et al.*, 2011). This model included three major modules: particle precipitation, particle size distribution, and particle transport to the wall. The particle precipitation was modeled using an equation of state. The particle size distribution was evaluated with a force balance on the asphaltene particles attached to the wall. They considered the following forces: van der Waals, drag force, lift force, and friction force. The module for particle transport to the wall was based on calculating the particle flux to the wall caused by the Brownian motion. Also, a shear removal term is included in the particle transport module. The model assumed that relatively large particles do not deposit on the wall and therefore a critical particle size was introduced as a model parameter in the deposition process. Lab-scale data was used to validate this model (Akbarzadeh *et al.*, 2011).

Vilas Boas Favero *et al.* (2016) showed that a mass-transfer-limited one-dimensional deposition model can explain the asphaltene deposition of nanometer-sized unstable asphaltenes in the viscous flow regime for measuring the asphaltene deposition in a packed bed apparatus. This model uses a mass transfer coefficient correlation and does not require tuning parameters. Guan *et al.* (2017) also developed a one-dimensional model for asphaltene deposition in wellbores or pipelines. This model includes a thermodynamic module and the transport module. The thermodynamic module used the Peng-Robinson EOS to model asphaltene precipitation, and the transport module included the modeling of fluid transport, particle transport, and asphaltene deposition. A reasonably accurate prediction of the asphaltene deposit layer profile was attained.

Horizontal Flow

Mirzayi *et al.* (2013) developed a model for asphaltene deposition in horizontal flow including the effect of gravity settling, thermophoresis, buoyancy, Brownian diffusion, drag force, and shear removal. They used this model to predict the asphaltene deposition rates under different flow conditions and study the effects of particle size, temperature gradient, and fluid velocity. They concluded that the gravitational and thermophoresis forces played a significant role in the deposit formation under flow conditions.

Recently Alhosani and Daraboina (2020) developed a model to predict the deposition for single-phase flow by applying a mass balance on asphaltene particles based on their size. The model included precipitation, aggregation, and deposition mechanisms. They verified the model performance with experimental data.

2.6 Fundamentals of Multiphase Flow

In the liquid droplet regime, deposition is a misnomer. Rather, there is liquid-liquid flow with the potential for the heavy liquid phase to accumulate. While gas-liquid multiphase flow has been studied extensively, liquid-liquid multiphase flow is less well understood. The discussion below will focus mainly on the research conducted on oil and water systems because these liquid-liquid systems have been studied in the literature. Two flow orientations are of relevance to the oil industry: horizontal flow (pipelines) and ascending vertical flow (wellbores). Each is reviewed below. Core annular vertical flow is of particular interest to this thesis because this flow pattern was used to interpret the asphaltene deposition experiments at high temperatures performed in this thesis. This flow pattern is discussed in more detail separately.

Horizontal Flow

When two immiscible liquids flow together in a horizontal pipeline, they form a flow pattern. The flow patterns describe the internal configuration and relative position of the phases in the flow. Generally, the classification of flow patterns starts from completely separated to fully dispersed flows. In separated flows, both phases retain their continuity. In dispersed flows, one of the phases is discontinuous (Brauner, 2003; Piroozian, *et al.*, 2017). The categorization of flow patterns in liquid-liquid horizontal pipes has been assigned different names by different researchers and the

number of flow patterns identified has also varied. Figure 2.4 shows the most recognized patterns, which include the following (Elseth, 2001; Ibarra *et al.*, 2015):

- Bubbly flow: Droplets of one liquid are heterogeneously or homogeneously dispersed in the other liquid.
- Slug flow: Large slugs or pockets of one liquid travel intermittently through the pipeline, separated by regions of the other liquid.
- Churn flow: Two immiscible liquids form elongated slugs each with emulsified droplets of the other phase. The droplets are continuously agitated and churned by the flow.
- Stratified flow: Both liquids flow as separate layers with the heavier liquid at the bottom. This flow pattern can be subdivided into stratified smooth (SS) and stratified wavy (SW).
- Annular flow: one liquid flows in an annulus around the pipe circumference and the other liquid flows in the core of the pipe. Mainly encountered in high oil viscosity in which water is the annular liquid. Also termed core annular flow.
- Dual continuous: Like stratified flow, each liquid forms a continuous phase along the pipe; however, an emulsion(s) is also present. This flow pattern includes several sub-categories such as an oil layer with an oil-in-water emulsion layer, a water layer with a water-in-oil emulsion layer, and a three-layer flow.

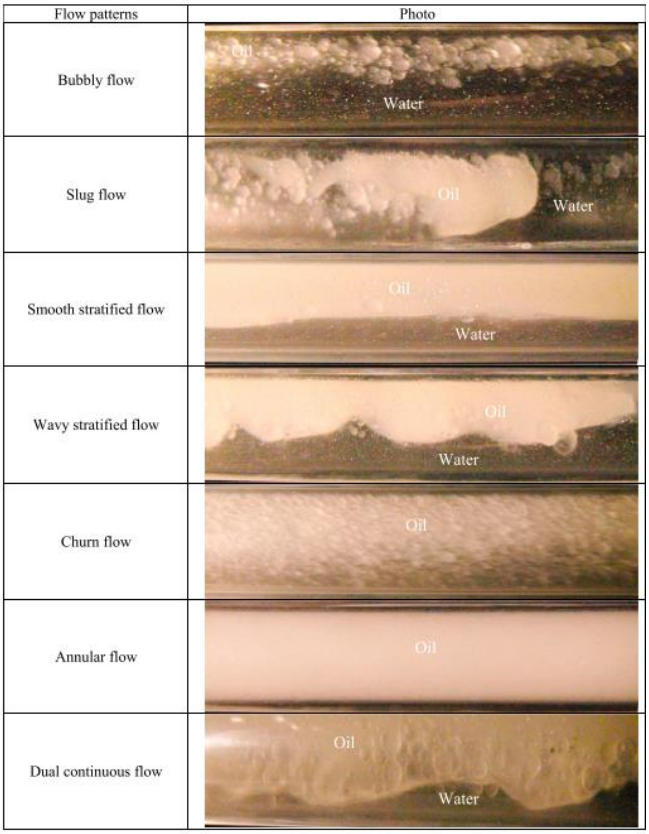

Figure 2.4. Photos of oil-water two-phase flow patterns in a 20 mm ID horizontal pipe (Hanafizadeh *et al.*, 2015).

Experimental determination of flow patterns is the key to modeling liquid-liquid flow because all design variables depend on the flow pattern. Flow patterns for mixtures of oil and water have been identified using high-speed cameras, conductivity probes, laser diffraction, and gamma-ray densitometry (Ahmed and John, 2018). Oil phases include mineral oil, kerosene, paraffin oil, and various crude oils. Pipe materials include stainless steel, acrylic resin, and glass. The pipe diameters in these studies vary from 5.6 mm to 101.2 mm. The ratios of oil to water viscosity and density range from $0.7 \leq \mu o/\mu w \leq 12550$, and $0.684 \leq \rho o/\rho w \leq 1$. The interfacial tension ranges from 0.017 N/m to 0.05 N/m (Ahmed and John, 2018; Osundare *et al.*, 2020).

In general, the flow pattern depends on the balance of inertial, gravity, buoyant, and interfacial forces. However, determining the exact flow pattern solely based on physical properties is challenging. While some physical properties can provide insights into the expected flow behavior, the flow pattern depends on numerous factors, including the operating conditions (such as

temperature, pressure, flow directions, flow rates, and flow rate ratios), properties of the fluids (such as density, viscosity, surface or interface tension, and mutual solubility), and the characteristics of the channel (including its geometry, size, and orientation). The main effect of the operating temperature and pressure is on the physical properties of the fluids (Huang *et al.*, 2011). The effects of the other factors are discussed below.

Effect of Superficial Velocity

Superficial velocity relates to the inertial force. Hanafizadeh *et al.* (2015) observed that horizontal flow patterns depended on the superficial velocity of each phase, as shown in Figure 2.5. At low superficial water velocity and low superficial oil velocity, stratified flow was observed. At this condition, the velocity was not enough to induce turbulence with which to disperse the oil. Gravity forces dominated allowing the the denser fluid to settle. As the oil velocity increased, the stratified flow transformed from smooth to wavy flow due to the increased drag at the interface. At an even higher superficial velocity of oil, dual continuous flow was identified. Both phases remained continuous, but the turbulence was sufficient to partially emulsify the liquid. Hence, one or both liquids included emulsified droplets of the other liquid. In some cases, the emulsion flowed in a distinct third layer. At high superficial water velocity and low superficial oil viscosity, bubbly flow was observed. At this condition, the high-water velocity created a turbulent environment that completely emulsified the relatively small volume of oil. At higher superficial oil velocity, there was too much oil to fully emulsify it, and the oil formed slugs. At high superficial velocities of both oil and water, core annular flow was observed. In effect, the oil slugs joined into a continuous core flow.

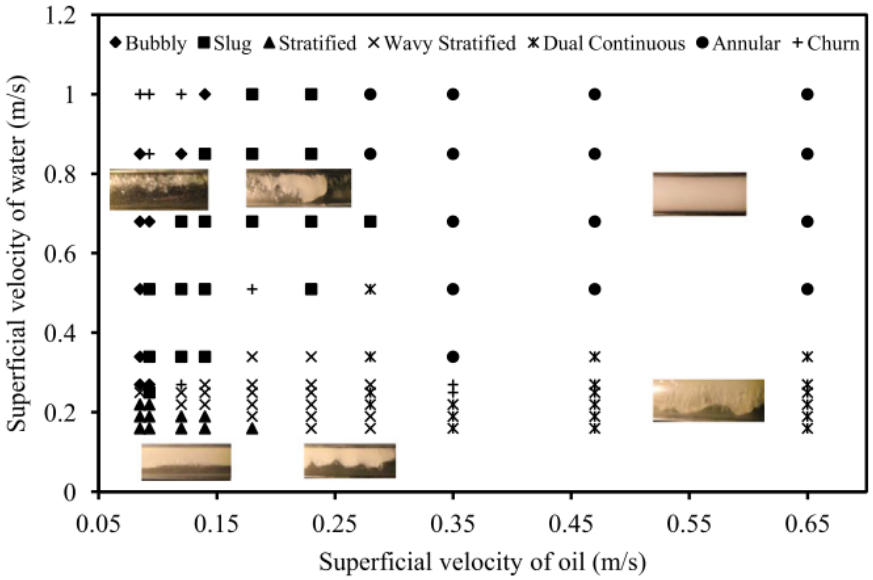

Figure 2.5. Flow patterns map of two-phase oil–water flow in a horizontal pipe (Hanafizadeh *et al.*, 2015).

Effect of Density

The way in which fluids flow can be affected by gravity and buoyancy forces which depend on the density difference between the two liquids (Hanafizadeh *et al.*, 2015). When two immiscible liquids flow together in a pipe, they tend to stratify at low superficial velocities. However, the greater the difference in density, the more effective this separation becomes (Charles *et al.*, 1961; Al-Wahaibi *et al.*, 2012). In liquid-liquid flows with low-density differences, the impact of gravity is reduced, and the flow pattern is greatly affected by wetting and surface tension properties (Cai *et al.*, 2012). In this case, dispersed flow patterns are more likely to occur.

Effect of Viscosity

An important factor in multiphase flow is the stability of the interface between the two liquids. Here, stability refers to the resistance of the interface to deformation and its ability to restore the original condition after deformation. More formally, the growth in the amplitude of deformations is suppressed. Stability depends mainly on the viscosity ratio of the two fluids and the interfacial tension. The higher the viscosity difference between the two liquids, the more unstable the interface and the more likely wavy or dispersed flow is to occur (Al-Wahaibi *et al.*, 2012). For systems with a high viscosity ratio, at low superficial water velocity and increasing oil velocity,

stratified flow transformed into bubbly (superficial water velocity less than 0.1 m/s) and dual continuous flows (superficial water velocity higher than 0.1 m/s) as described previously. However, at lower oil viscosity, only a transition from stratified to dual continuous flow was observed.

Effect of Interfacial Tension

The ability of two phases to mix or form an emulsion depends on their interfacial tension. The lower the interfacial tension, the less stable the interface. Mixing and emulsification are facilitated because coalescence is reduced, and droplet breakup is promoted. Hence, lower interfacial tension results in smaller droplet sizes and increased dispersion, making dispersed flows more likely to occur. In contrast, higher interfacial tension increases the likelihood of phase separation between the two liquids, making stratified flows more likely to occur (Al-wahaibi, *et al.*, 2011; Al-wahaibi, *et al.*, 2012; Al-wahaibi, *et al.*, 2014).

Abubakar *et al.* (2015) studied the flow characteristics for a medium-viscosity oil/water two-phase flow with low interfacial tension (12.9 mN/m). They observed stratified, dual conditions, and dispersed flow. They found that stratified flow was only present at low mixture velocities (< 0.2 m/s). The dominant flow pattern was dispersed flow. They also found that low interfacial tension led to higher pressure gradients at almost all input oil volume fractions due to the formation of dispersions.

Effect of the Pipe Wettability

Contact angle measurements show that steel could be either oil or water wet depending on the conditioning of the surface; that is, it was previously oil or water wetted, respectively. Acrylic pipes were preferentially wetted with oil in all cases (Angeli and Hewitt, 1999). Paolinelli (2018) researched the impact of wetting hysteresis on carbon steel horizontal pipes, which indicates that the surface exhibits either hydrophobicity or hydrophilicity depending on the first fluid it comes into contact with, be it oil or water, respectively.

The wettability of the pipe affects the location of the core and annular liquid in core annular flow patterns, favoring annular films of water on hydrophilic pipes and oil on hydrophobic pipes

(Hasson *et al.*, 1970). Angeli and Hewitt (1998) found that the wall material also affected other flow patterns. They found that the flow patterns were more dispersed in steel pipe sections than in acrylic sections, even with the same velocities and water fractions. The steel tube also exhibited higher pressure gradients than the acrylic tube. They concluded that both wettability and wall roughness could influence flow patterns.

Effect of Pipe Geometry

Al-Wahaibi *et al.* (2012) studied the effect of pipe diameter in 25.4- and 19-mm ID acrylic test sections on flow patterns with oil and water. They observed that the pipe diameter considerably influenced the transition between stratified and non-stratified flow in horizontal oil-water flow. Two regions were observed in the transition boundaries of this flow. In the first region (up to superficial oil velocity = 0.14 m/s) the transition to non-stratified flow occurred at lower superficial water velocities in the smaller pipe diameter (19 mm). As the velocity of water increased and the velocity of oil decreased, the thickness of the oil layer decreased, and the turbulence of the water layer increased. This caused the oil layer to break into droplets. The droplets formed earlier in the smaller pipe because the inertial forces acting on the fluids were higher. In smaller pipe diameters, the oil layer was thinner, and a transition from stratified to bubble flow occurred earlier. In the second region (superficial oil velocity > 0.14 m/s), a transition to dual continuous flow was observed at a lower superficial water viscosity in the 25.4 mm ID pipe compared to the 19 mm ID. At higher oil velocity, the oil layer was thick enough to resist the formation of droplets. However, as the water velocity increased, the relative movement of the two layers increased, which destabilized the interface and caused the wave to grow in amplitude until droplet formation was observed.

Hanafizadeh *et al.* (2015) investigated flow patterns of two-phase oil-water flow varying the inclination of the pipe between -45 and +45°. They found that pipe inclination influences the interaction between the dominant forces (inertia, gravity, and buoyancy), which can delay or accelerate the emergence of a flow pattern. They observed bubbly, slug, smooth stratified, wavy stratified, churn, core annular, and dual continuous flow. They noted that non-stratified flows such as bubbly and slug flows were dominant in upward flows and stratified flows were dominant in the downward flows.

2.6.1 Ascending Vertical Flow

In vertical ascending liquid-liquid flow, flow patterns have been classified into six main types (Flores *et al.,* 1997; Foroughi and Kawaji, 2011; Guo *et al.,* 2018) as shown in Figure 2.6:

- Dispersed flow: flow of one liquid with very small, emulsified droplets of the other liquid; droplet sizes of similar magnitude.
- Bubbly flow: similar to dispersed flow but with droplets of varied sizes.
- Slug flow: flow of one liquid with large blobs (slugs) of the other liquid.
- Creep flow: large elongated or spherical slugs of one liquid eccentrically attach to the pipe.
- Churn flow: similar to slug flow but with an elongated wake flow consisting of droplets at the tail of the slugs, with entrainment of small droplets of the continuous phase liquid.
- Annular flow: The outer liquid is pushed against the conduit wall, forming a thin ring around the inner liquid. Also termed core annular flow.

Flow pattern maps are used to describe the physical phenomena of two-phase flows and the transition between them. Velocity is the main factor that influences the transition from one pattern to another in liquid-liquid two-phase flow. Therefore, these flow patterns are shown as a function of the velocities of the two phases (Osundare *et al.,* 2020). The boundary between the subsequent flow patterns is not well-defined. As a matter of fact, transitions are a quite subjective phenomenon, which depends sometimes on the observer's interpretation (Bannwart *et al.,* 2004).

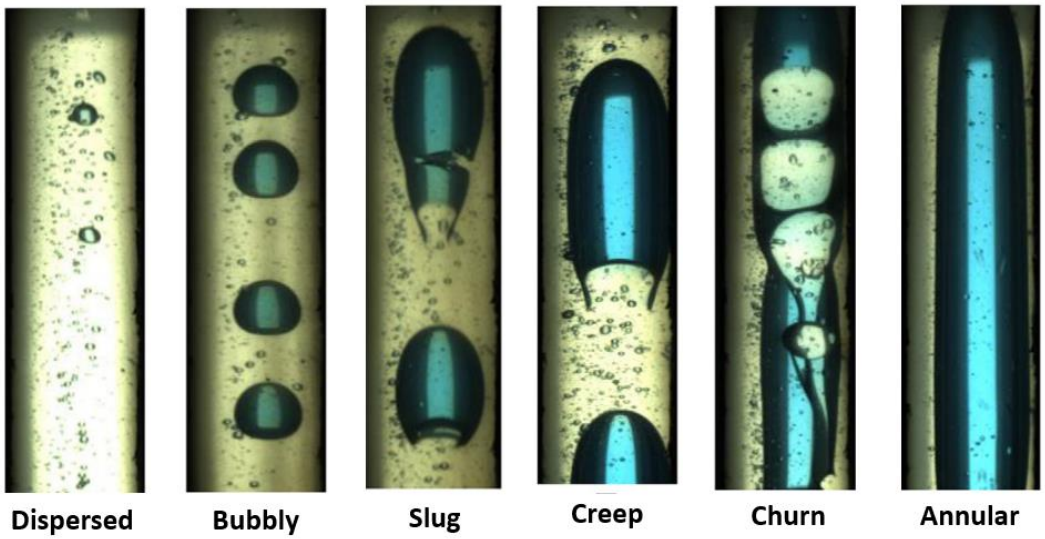

Figure 2.6. Oil-water two-phase upward vertical flow patterns were observed under room temperature and atmospheric pressure. Yellow: naphthenic oil; blue: water dyed with methylene blue (Adapted from Guo *et al.,* 2018).

As with horizontal flow, the flow pattern depends on numerous factors, including operating conditions (such as temperature, pressure, flow directions, flow rates, and flow rate ratios), the properties of the fluids (such as density, viscosity, surface or interface tension, and mutual solubility), and the characteristics of the channel (including its geometry, size, and orientation). The impact of these factors in vertical flow is less well delineated than in horizontal flow. Some observations for flow patterns in a vertical configuration are discussed below.

Effect of Superficial Velocity

Guo *et al.* (2018) varied the input water fraction from 10 to 90 vol% at room temperature, atmospheric pressure, and a fixed mixture velocity of 0.03 m/s. The observed flow patterns were shown in Figure 2.6. At lower water inputs, single-phase flow was observed. At a low input water fraction (10 vol%), there was sufficient turbulence to emulsify all of the water, and water-in-oil dispersed flow was observed with very small uniform water droplets. As the input water fraction increased (20 to 30 vol%), the turbulence was not high enough to disperse the water phase, leading to the coalescence of water droplets into large droplets (water-in-oil bubbly flow). The droplet sizes were varied but less than the pipe I.D.

At intermediate water input fractions, discontinuous two-phase flow occurred. At input water fractions of 40 to 50 vol%, the size of water droplets increased and the bubbly flow transformed into water-in-oil slug flow. Water-in-oil slug flow is characterized by large elongated or spherical water slugs in the center of the pipe, with elongated water slugs formed by the coalescence of adjacent spherical water slugs. At an input water fraction of 60 vol%, the diameter of the water slugs continued to increase and the slugs flowed eccentrically along the pipe surface (creep flow). At input water fractions of 70 to 80 vol%, the slugs grew an elongated tail-like wake consisting of water bubbles, with small oil droplets or oil bubbles entrainment (churn flow). The wake formed when the relative velocity between the dispersed and continuous phases was high and interfacial instabilities occurred due to density and viscosity differences.

At an input water fraction of 90 vol%, a two-phase flow was observed. The water slugs united into a continuous core flowing inside an annulus of oil (core annular flow). The conditions at which each flow pattern appears depends on other factors as well. For example, a water-wet pipe surface is expected to produce an annulus of water at high oil fractions. Nonetheless, a similar set of patterns would be observed.

Similarly, Mydlarz-Gabryk *et al.* (2014) observed that when the water's superficial velocity was low, and the oil's superficial velocity was high, the water tended to pass through the channel in drops with varying sizes and shapes. The oil occupied the entire cross-section of the channel and remained in contact with the pipe wall. When the superficial velocity of water increased, the droplets coalesced leading to slugs.

Effect of Temperature and Pressure

As with horizontal flow, the main effect of temperature and pressure is on the properties of the liquids, particularly the viscosity ratio and interfacial tension. Guo *et al.* (2018) evaluated the effect of temperature at 50, 90, and 130°C. The effect of pressure on oil-water vertical flow patterns was investigated at a fixed temperature of 130°C from atmospheric pressure to 20.2 MPa. They found that when the oil-water interfacial tension decreased (higher temperature), less energy was needed to create a new interface, resulting in smaller water droplets. In addition, a lower oil/water viscosity ratio (higher temperature and lower pressure) destabilized the interface more quickly than a higher ratio.

2.6.2 Core Annular Vertical Flow

The core annular flow pattern can occur with two immiscible liquids with very different viscosities. The density of the liquids need not necessarily be the same. Depending on the pipe wettability, the more viscous fluid can occupy either the annulus or the core (Bannwart, 2001; Guo *et al.*, 2018; Paolinelli, 2018). High interfacial tension favors the core annular configuration; however, the impact of interfacial tension decreases at large pipe sizes (Bannwart, 2001). The interface in the core annular flow is wavy as discussed below.

The wave pattern with oil in the core was found to depend on the flow direction: bamboo waves in up-flow and corkscrew waves in down-flow. Up-flow is relevant to this thesis. The bamboo waves result from the shear stabilization of capillary instabilities in up flow, leading to a regime of wavy flow in trains of sharp crests connected by long filaments. The filaments which connect the crests thicken as the oil velocity is increased for a fixed water velocity, and the average length of the waves decreases. Yet further increases in the oil throughput lead to much thicker and shorter stems and the bamboo crests become very jagged, irregular, and non-axisymmetric (Bai *et al.*, 1992).

Bamboo waves in up flow are stretched due to the combined action of buoyant and shear forces. The buoyancy part of this mechanism is simply that the oil is lifted by gravity relative to the heavier water which is stationary on the pipe wall. Therefore, the crest of a wave on the oil must move forward relative to the water. The wave is nearly stationary because the oil is so viscous. The shear force acts against the buoyant force creating waves that form a single pattern traveling at constant speed and wavelength depending on the flow rates, orientation, and fluid properties (Bannwart, 1998). Wavy core annular flow can be disturbed with an increase in the velocity of the core and would then evolve toward slug flow (Bannwart *et al.*, 2004).

Rodriguez and Bannwart (2006) investigated the interfacial waves observed in upward vertical core annular oil-water flow. They used a vertical glass pipe and measured the wave speed, shape, and wavelength to determine the in-situ oil volume fraction, as shown in Figure 2.7. They found that, as expected, the oil core flowed 55% faster than the surrounding water annulus due to buoyancy. The interface waves moved slower than the mixture velocity and the difference was attributed to interfacial shear. They found that the wave amplitude sharply decreased until the ratio of oil superficial velocity to water superficial velocity reached approximately 5. However, when the oil core started filling the pipe volume, the amplitude decrease became slower. The wavelength of the oil-water mixture also decreased as the water flow rate increased.

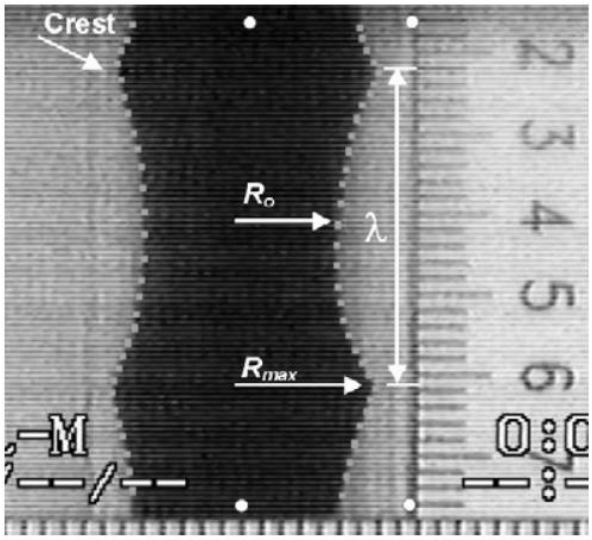

Figure 2.7. Typical image of upward vertical core annular flow showcasing the geometric structure of the interface between water and oil. The annulus contains water, while the core holds oil (Rodriguez and Bannwart, 2006).

Vuong *et al.* (2009) investigated oil-water flows in horizontal and vertical pipes with a 50.8 mm ID pipe. They focused on the flow pattern, pressure gradient, and water holdup. They observed core annular flow with oil film on the pipe wall for vertical flow. Oil flowed in the core while water flowed as an annulus next to an oil film attached to the pipe wall. The oil film remained at the wall due to the high oil viscosity and the oil-wet pipe surface. They found that the flows with an oil film on the pipe wall tended to have higher pressure gradients than water-wetted pipes. Increasing the superficial water velocity increased the shear stress near the pipe wall. The high shear stress thinned the oil film at the pipe wall and broke it into droplets.

2.6.3 Liquid-Liquid Flow Models

Bannwart (1998) used the kinematic wave theory to model the speed of interfacial waves observed in core annular flows of viscous oils with water. Since the core was viscous, the dynamic effect on the interfacial wave was assumed to be negligible. A general model was developed for the volumetric fraction (holdup) of the core annular flow. He fitted the model parameters to match the measured wave speed and superficial velocities for core annular flow of oil-water in horizontal and vertical flow. This model includes the effect of fluid properties and can be applied to upward, downward, and horizontal flows.

Bannwart (2001) developed phenomenological models for the core volume fraction (holdup) and the pressure drop gradient during liquid-liquid flow through horizontal and vertical pipes. The volume fraction (holdup) was determined based on the measured interfacial wave speed (Bannwart, 1998), and an additional parameter was introduced to account for the effect of shear at the walls on dispersion. The model can determine the volume fraction or holdup using fluid properties and superficial velocities. The model equation includes adjustable constants that can be adjusted to match their experimental wave speed data. In addition, equations were developed for specific scenarios, such as horizontal core flow or equal density and vertical flow with an infinitely viscous core. The calculated volume fraction (holdup) agreed with experimental data from Bai (1995).

The pressure drop gradient model was based on mass and momentum balances and accounted for the effects of turbulence in the annular fluid, a wavy interface, and buoyancy (for the vertical system). The model was tested on experimental data from Bannwart (1998), Oliemans (1986) for horizontal flow, and Bai (1995) for vertical flow. The standard deviation between calculated and measured pressure drops ± 14% for horizontal flow and ± 25% for vertical flow.

Rodriguez and Bannwart (2006) developed a more general method for determining the holdup as an extension of the model proposed by Bannwart (1998). A correlation was established for the oil holdup in turbulent flow and compared to direct experimental photographic measurements. The correlation matched the measured hold up to within ±5%. The conclusion was that the kinematic wave model accurately represented interfacial wave speed in a turbulent flow.

2.7 Asphaltene-Rich Phase Accumulation in the Liquid Droplet Regime

Asphaltene-rich phase accumulation in the liquid droplet regime has not received much attention. Most studies have been centered around fouling in heat exchangers. One recent study specifically examined the accumulation of an asphaltene-rich phase in the liquid droplet regime. No models of this accumulation were found in the literature.

Asphaltene deposition in a heat exchanger at surface temperatures from 185 to 310°C has been investigated with a flow loop apparatus. Heavy oil was blended with the following diluents: fuel

oil, Paraflex lubrication oil, and heavy vacuum gas oil. The temperature of the bulk fluid was held constant at 85°C. The main findings from this study were that asphaltene deposition increased with diluents precipitation induction and that the initial asphaltene deposition rate increased with increases in surface temperature. (Watkinson, 1968; Asomaning and Watkinson, 2000; Watkinson, 2007; Hong and Watkinson, 2009).

Do, *et al.* (2022) used the capillary flow apparatus described in Section 2.5 to investigate asphaltene-rich phase accumulation in horizontal laminar liquid-liquid multiphase flow. They examined mixtures of bitumen and n-heptane at 130°C. They found that the asphaltene-rich heavy-phase droplets settled and coalesced to form a continuous heavy-phase layer leading to stratified flow with occasional temporary plugging.

2.8 Summary

Asphaltenes have the potential to precipitate either as glassy particles (at temperatures below approximately 90°C) or as part of a viscous asphaltene-rich heavy phase (at temperatures above 130°C). The glassy particles are initially in the order of 1 mm in diameter but rapidly aggregate into fractal structures that are hundreds of micrometers in diameter. The size and fractal dimension of the structures depend on the type and amount of solvent. After formation, the structures can be fractured with sufficient shear but do not reform. In capillary tube tests performed with mixtures of bitumen and n-heptane, the glassy particles formed porous deposits which underwent cycles of deposition and erosion.

In the liquid droplet regime, a two-phase flow occurs with the potential for accumulation rather than deposition. Flow patterns in two-phase flow are dictated by the balance of inertial, gravity, buoyant, and interfacial forces. However, it is challenging to predict the flow pattern. In capillary tube tests performed with bitumen and n-heptane, asphaltene-rich heavy-phase droplets settled and coalesced to form a continuous heavy-phase layer leading to stratified flow with occasional temporary plugging. With the high viscosity contrast between an asphaltene-rich phase and a solvent-rich phase, core annular flow is anticipated in a vertical configuration.

Chapter 3: Experimental Methods

In this chapter, the experimental methods used in this thesis are outlined. The deposition apparatus and procedures are presented. In addition, the property data required for this thesis but obtained from other sources or correlations are summarized.

3.1 Materials

The Canadian Bitumen sample used in this thesis is labeled as WC-B-A3 (8) where “WC” denotes Western Canada, “B” indicates bitumen, and “A3” denotes the reservoir source. This sample came

from a steam-assisted gravity drainage process and was supplied by Japan Canada Oil Sands. The bitumen sample had been treated to remove water and solids prior to receipt and had a residual water content of less than 1.5 wt% (Paniagua Fernandez, 2021). Selected properties and the SARA assay of the bitumen are provided in Table 3.1. The solvents used in this thesis were *n*-heptane (99.5% purity) and toluene (99.5% purity) purchased from Fisher Scientific. Industrial grade nitrogen (99.5% purity) and cyclohexane (99.0% purity) were purchased from Air Liquide Canada Ins and Millipore Sigma, respectively.

Table 3.1. Properties and SARA assay of WC-B-A3 bitumen (Grimaldo-Aguilar, 2018).

Property	Units	Value
Density at 20°C and 1 atm	g/cm³	1.009
Viscosity at 20°C and 1 atm	mPa·s	358000
Molecular weight	g/mol	570
Saturates	wt%	19.2
Aromatics	wt%	41.0
Resins	wt%	18.2
C5-asphaltenes	wt%	20.2
C7-asphaltenes	wt%	15.4

3.2 Asphaltene Deposition Measurements

An existing Asphaltene Deposition Apparatus, previously commissioned for horizontal flow (Do *et al*., 2022), was adapted for vertical flow. The changes made to the apparatus include reconfiguring the fittings before the capillary tube, reorienting the capillary tube, changing location pressure transducer legs, and modifying the waste collector to have a top waste discharge. The apparatus provides pressure drop profiles over time for deposition in a capillary tube. In addition, the capillary tube can be removed at the end of an experiment to determine the deposit's location, mass, and solvent content.

3.2.1 Asphaltene Deposition Apparatus

A schematic of the deposition apparatus, after modification for vertical flow, is shown in Figure 3.1. The apparatus components are listed in Table 3.2. Two blind cells contain feeds (one with *n*-heptane and one with pre-diluted bitumen). A third blind cell contains the cyclohexane used after the end of the experiment. The two independently operated positive displacement pumps are used

to displace each feed using hydraulic oil. The static mixer design is described in more detail in Appendix A. It creates a crossflow between the pre-diluted bitumen and *n*-heptane streams to promote effective mixing, as verified previously (Do *et al*., 2022). Deposition is monitored in the vertical capillary tube where the differential pressure gauge is used to measure the pressure drop over time. The back pressure regulator (BPR) is used to control the pressure of the system. All fluids and the capillary tube are housed inside an air bath (dotted line in Figure 3.2) to maintain the temperature within ± 0.1 °C.

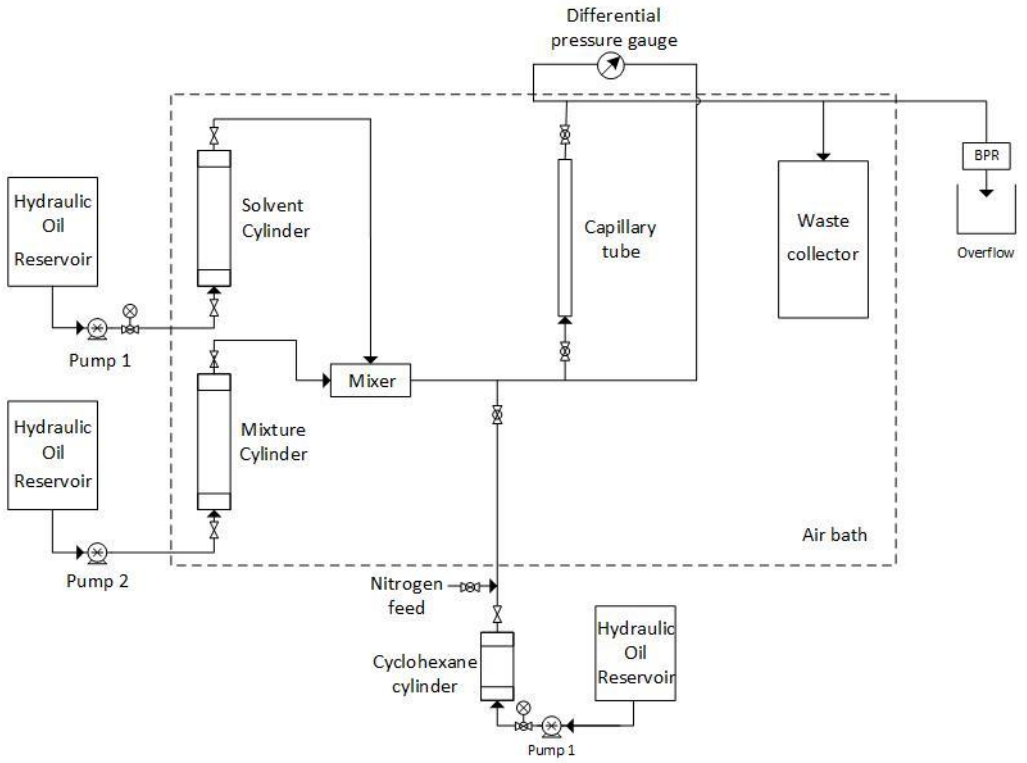

Figure 3.1. Schematic of the asphaltene deposition apparatus.

Table 3.2. Main components of the asphaltene deposition apparatus.

Equipment Component	**Specification**
Cylinders	Each blind cell is equipped with a piston and has a maximum capacity of 450 cm³.
Pump 1: Demi 2510S	Variable volume positive displacement pump with a range of 0.01 to 10.00 cm³/min. The maximum operating pressure is 17.2 MPa. The flow rate accuracy is ±1% of the set point.
Pump 2: Quizix SP-5200	Variable volume positive displacement pump with a range of 0.0001 to 15.0000 cm³/min. The maximum

Equipment Component	Specification
	operating pressure is 69 MPa. The flow rate accuracy is 0.005 cm^3/min.
Static mixer	Custom-made design to create crossflow between pre-diluted bitumen and solvent to promote better mixing (Do, 2021).
Capillary tube	Stainless steel Swagelok ® tube with an internal diameter of 1.75 mm and a length of 30 cm.
Swagelok ® Ball valves	3 valves: one located on each end of the capillary tube and another at the cyclohexane inlet.
Rosemount 1151 differential pressure transducer	Gauge is precise to ± 0.0025 kPa with a maximum pressure drop limit of 69.0 kPa and a maximum pressure rating of 25.0 MPa.
Blue M POM-136B-1 air bath	Controls the oven temperature with a self-tuning temperature controller to within ± 0.1°C.
Back pressure regulator (BPR)	Pressure control valve accurate to 1% of the setting value.

3.2.2 Asphaltene Deposition Procedure

Pretest Procedure

The sample of bitumen used for each experiment is pre-diluted to 50 wt% *n*-heptane (below the onset of precipitation) to reduce its viscosity and promote rapid mixing in the static mixer. A known mass of bitumen is added to a beaker and heated in an oven at 60°C for 15 minutes to reduce its viscosity. Then, a specified mass of *n*-heptane is added as follows: 1) 10% of the specified mass is added dropwise to further reduce the viscosity; 2) the solution is mixed with a 4-blade impeller mixer at 200 rpm; 3) while mixing, the remaining *n*-heptane is added at a rate of 1 cm^3/min using a Quizix Pump model Q52000. During the mixing, some of the solvent may evaporate, which can affect the final composition. Therefore, once the mixing process is completed, the mass of the mixture is measured and, if necessary, *n*-heptane is added to reach the specified mass.

A new capillary tube is cut from Swagelok tubing and deburred to smooth out any visible roughness near the cuts. The individual nuts and ferrules required to connect the capillary tube to the apparatus are attached. The mass and length of the capillary tube including the fittings are measured and recorded.

Pre-measured masses of *n*-heptane and pre-diluted bitumen are placed into two separate blind cells. Hydraulic oil is pumped into each blind cell to expel any residual air in the blind cells, and the cells are connected to the previously assembled apparatus. Then nitrogen is introduced into the system to bring the apparatus to experimental pressure and dilute the oxygen in the system. A snoop test is performed to check for leaks. The air bath is then turned on and set to the experimental temperature. The apparatus is left at the set temperature for a minimum of four hours to allow the nitrogen filled system to attain thermal equilibrium. Then, approximately 30 cm^3 of *n*-heptane is injected to prefill the dead volume space, including all lines leading up to the waste collector. The apparatus is left for one hour before running the experiment to reach thermal equilibrium and ensure that the pipe surfaces are wetted with *n*-heptane.

Deposition Procedure

After the start-up procedure is completed, solvent and pre-diluted bitumen are injected separately to the static mixer each at a fixed volumetric rate set to reach the target composition (50, 65, 75 and 90 wt% *n*-heptane) and total flow rate. The mixture flows through the capillary tube and the pressure drop across the tube is monitored. If the pressure gauge reaches its maximum limit (70 kPa), the Quizix Pump Q52000 is used to measure the pressure above this point. The pump pressure is converted to a differential pressure by subtracting the system pressure and the frictional losses resulting from the piston movement in the cylinder. After passing through the test section, the mixture is directed to a waste collector cylinder, and it remains there until the end of the experiment.

After reaching the specified run time, the pumps are turned off to stop flow. The oven is turned off and its doors are opened. The ball valves located at the inlet and outlet of the capillary tube are closed and cold water is sprayed over the tube to facilitate the cooling process. Pump 1 is disconnected from the solvent cylinder and connected to the cyclohexane feed.

Within 20 minutes of shutting the pumps off, the ball valves are opened and approximately 15 cm^3 of cyclohexane at room temperature is injected at 1 cm^3/min to remove any undeposited material in the capillary tube. Then, the ball valves at either end of the capillary tube are closed, isolating

the test section from the rest of the apparatus, and the capillary tube is removed from the apparatus to measure the mass and location of the deposits. The tube removal procedure is done by slowly loosening the nut at the outlet end and allowing the fluid inside the tube to depressurize before removing the tube from the apparatus, the residual fluid is drained, and the tube is set aside for the measurements described in the next section. The rest of the apparatus is disassembled and cleaned with toluene, including the differential pressure transducer legs.

Measurement of Solvent Content in Deposit

After removing the capillary tube from the apparatus, its mass is monitored over time to find the deposit mass and solvent content of the deposit. The drying process of the deposit involves two stages, as is shown in Figure 3.2a. In the initial stage, the cyclohexane that is coating the deposit and tube evaporates. In the second stage, the solvent inside the deposit diffuses out and evaporates until the final (dry) mass of the deposit is reached. The data for each stage was fitted with a linear segment, and the solvent within the deposit was determined by calculating the intercept of the fitted lines, as shown in Figure 3.2b. The wet deposit mass is then calculated from the mass of solvent in the deposit and the dry mass of the deposit. It was assumed that this solvent content was equivalent to the original *n*-heptane content of the deposit.

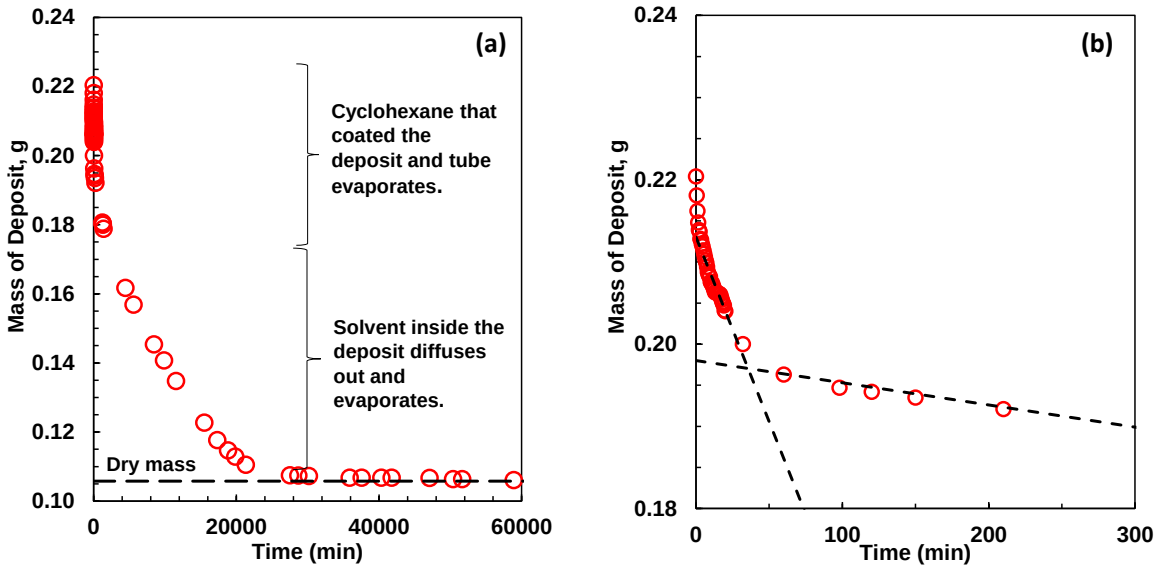

Figure 3.2. Solvent drying curve for experiment at 75 wt% heptane and 50°C for: a) entire drying process and b) initial 300 min of drying process.

Mass and Location of Deposit

Once the deposit is completely dry, the capillary tube is cut into four equal segments. The mass of each segment is measured, and the mass of deposit is determined from the difference between the mass of each segment and the mass of the capillary tube in each segment. The capillary tube mass is calculated from the length of the segment and the nominal mass/length of tube. The average mass/length is calculated from the known masses of the individual components used to construct the capillary tube. The deposit masses are then corrected based on the total mass lost during the cutting procedure averaged over each segment.

3.3 Design Considerations for the Vertical Flow Apparatus

3.3.1 Selection of Experimental Parameters

Pipe Dimensions

A capillary tube inner diameter of 1.7 mm was chosen to facilitate laminar flow. In addition, the diameter is small enough that the measured pressure drops are detectable within the limits of the pressure gauge. Smaller diameter tubes were found to have too many irregularities in the manufacturing of the pipe, leading to inconsistent results with different tubes. Smaller tubes also give smaller deposits such that the error in the mass measurements exceeded the magnitude of the measurement. It was not practical to increase the inner diameter of the tube with this apparatus. The next size up is 4 mm. At this size, the required sample volumes would be large and a much longer tube would be required to obtain a measurable pressure drop. The capillary tube length is limited to 30 cm to ensure it remains straight and fits within the oven's ceiling height.

Flow Rate

The minimum volumetric flow rate for this study was set to match the previous horizontal flow study and was 2 cm^3/min at standard conditions. This rate was selected because it is low enough to ensure that deposition occurs and to enable accurate measurements of the deposited mass in the capillary tube. The velocity of the fluid through the 1.75 mm ID capillary tube is 82.9 cm/min at standard conditions. The velocities at the experimental conditions were within 2% of this value.

With the vertical flow experiments, the velocity must be high enough to prevent the precipitated asphaltenes from settling and blocking the inlet. Casas *et al.* (2017) measured the settling velocity of precipitated asphaltene flocs in mixtures of bitumen and *n*-heptane to be between 0.1 and 0.4

cm/min at 21°C. Kosior *et al*. (2016) measured the settling velocity of asphaltene flocs in mixtures of bitumen and *n*-pentane to be 11.3 cm/min at 50°C. Considering that the settling rates in n-pentane diluted with bitumen are approximately two orders of magnitude higher than in the bitumen diluted with *n*-heptane (Duran *et al.*, 2019), the settling rate estimated for precipitated asphaltenes in a mixture of n-heptane and bitumen at 50°C is estimated to be approximately 0.1 cm/min. The experimental velocity of 84.6 cm/min far exceeds the asphaltene settling velocity and, therefore, settling is not expected to be a factor in these experiments.

Solvent Content

The solvent contents were selected to assess the effect of both the solvent content and the concentration of precipitated asphaltenes. Duran *et al*. (2019) measured asphaltene precipitation yields from mixtures of bitumen and *n*-heptane and calculated the concentration of precipitated asphaltenes, as shown in Figure 3.3. The concentration of precipitated particles reached a maximum at approximately 75 wt% *n*-heptane. Therefore, *n*-heptane contents of 65, 75 and 90 wt% were chosen to include a low precipitate concentration just above the onset, the maximum precipitate concentration, and a low precipitate concentration at a high *n*-heptane content.

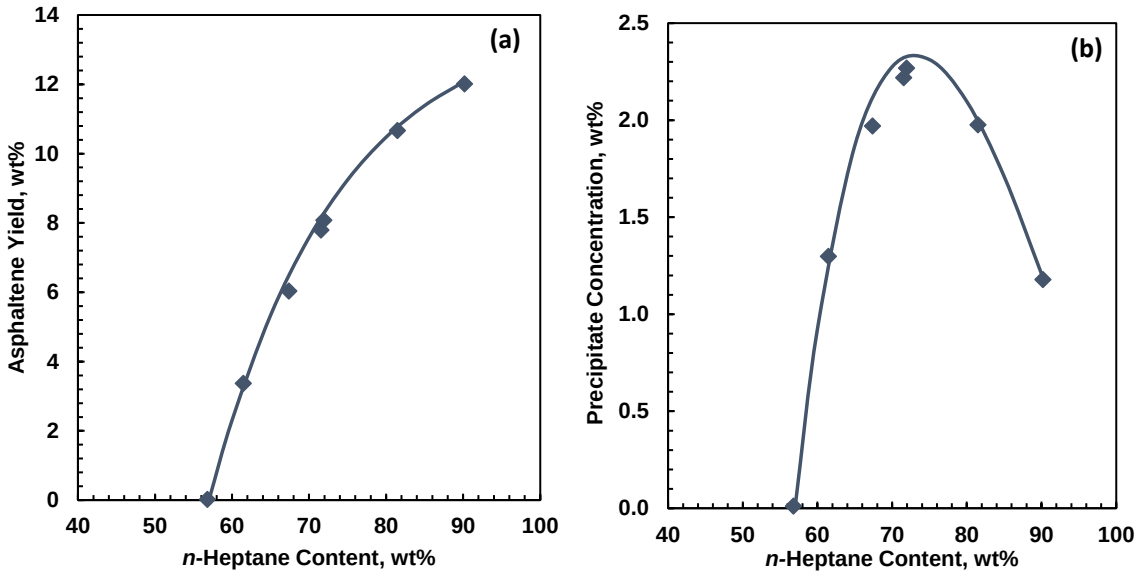

Figure 3.3. Asphaltene yield (a) and precipitate concentration (b) for WC-B-A3 bitumen diluted with n-heptane at 21ºC after 24 hours contact time. The symbols are data; the lines are empirical equations fitted to the yield data and provided as visual aids. Adapted from Duran *et al*. (2018).

3.3.2 Temperature Gradient Inside Oven

The experiments are intended to be isothermal but in practice temperature gradients may arise inside the oven. A significant temperature gradient could alter the temperature of the fluid flowing through the capillary tube and affect the flow pattern and deposition behavior. The Blue M Ultra-Temp Series Industrial Oven was used as an air bath in these experiments. The oven operates by passing air through a floor heater and up one wall of the oven. It flows from ports in the wall across the oven to the opposite wall, and then back to the heater for recirculation. The temperature was measured using a thermocouple at three different vertical points in the chamber to determine if a significant temperature gradient was present. The measurements were taken for set point temperatures 50°C, 90°C, and 130°C and the temperature gradients were 0.01°C/cm, 0.02°C/cm, and 0.06°C/cm, respectively, with the hottest air at the top of the chamber. The impact of the maximum temperature different on the viscosity and density of the fluid was less than 2%. In addition, the fluids would become less dense at greater heights and therefore the flow would remain stable.

3.4 Processing of Pressure Data

The differential pressure gauge has an offset which may shift as the experiment begins and the fluid's composition changes in the tube. The initial offset was measured during the start-up procedure when heptane was used to fill the apparatus lines and ranged between 0.32 and 0.70 kPa. The differential pressure was adjusted to an initial differential pressure of zero. The reported pressures are then the pressure drop exceeding the initial pressure drop and are termed the excess pressure drop. Figures 3.4a and 3.4b show the excess pressure drop at 50°C for a run with no precipitation (50:50 H/B) and a run with precipitation (75:25 H/B), respectively. As expected, the excess pressure drop with no precipitation remains near zero. However, the excess pressure drop with precipitation increases over time, indicating deposition in the capillary tube. The data may appear scattered but in fact is showing repeated pressure spikes associated with deposition and plugging.

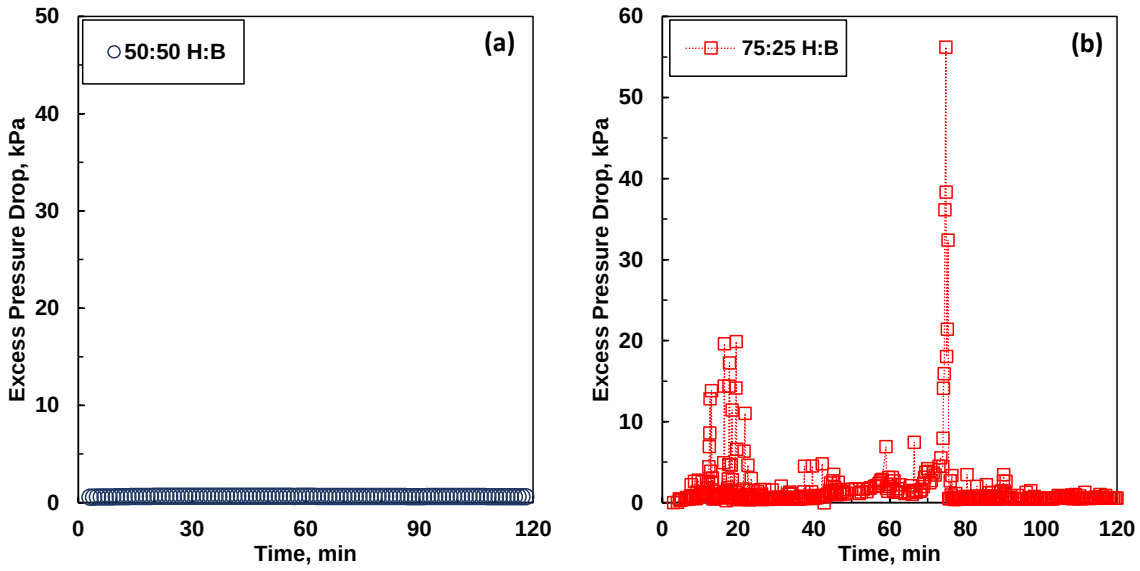

Figure 3.4. Excess pressure drop over time in a 30 cm capillary tube at 2.0 cm³/min and 50°C: a) below the onset of precipitation (50:50 H:B); b) above the onset (75:25 H:B).

3.5 Properties Obtained from Other Sources

Other information required for the experimental design and analysis include the onset of asphaltene precipitation and the density and viscosity of mixtures of bitumen and *n*-heptane. These properties were measured previously or determined from tuned correlations as described below.

3.5.1 Asphaltene Yields and Onsets

Asphaltene yields (amount of asphaltenes portioning to the heavy phase) in mixtures of *n*-heptane and bitumen were previously measured gravimetrically at ambient conditions by (Do *et al.*, 2022), following the bench top procedure at ambient conditions from (Johnston *et al*., 2017).

The onset of asphaltene precipitation (*n*-heptane content at which precipitation occurs) was determined by fitting the measured yield using the following empirical expression proposed by (Johnston *et al*., 2017):

$$Y = B_1[1 - \exp(-C_1(w_{C7} - w_{onset}))] \quad (3.1)$$

where Y is the asphaltene yield wt%, w_{C7} is the *n*-heptane content, w_{onset} is the *n*-heptane content at the onset of the asphaltene-rich phase, and B_1 and C_1 are constants. The constants and the onset composition are adjusted to minimize the least square error. The uncertainty of the fitted onset

based on the uncertainty of the yield data is ±0.6 wt% solvent. The method is illustrated in Figure 3.5a.

Yields at higher temperatures were predicted by (Do *et al.*, 2022) using the Modified Regular Solution (MRS) Model. The MRS model is an activity coefficient model that assumes that the mixture is in liquid-liquid equilibrium between two phases: a heavy phase rich in asphaltene and a light phase rich in solvent (Ramos-Pallares and Yarranton, 2020). Details of the modeling are provided in Appendix B. Figure 3.5b shows the modeled C5-asphaltene and bitumen yields at the conditions considered in this thesis.

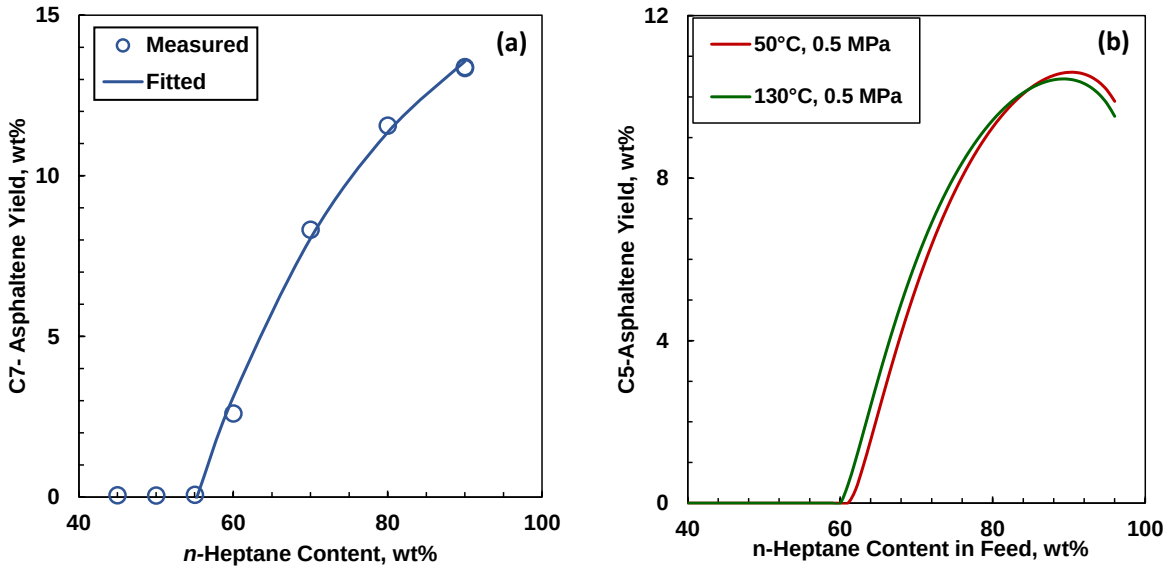

Figure 3.5. Asphaltene yield curve (a) at 21°C and 0.1 MPa and (b) MRS predicted yields at 50°C and 130°C, and 0.5 MPa for WC-B-A3 bitumen diluted with n-heptane. Adapted from Do, (2021).

3.5.2 Density of Mixtures of Bitumen and n-Heptane

The densities of the WC-B-A3 bitumen and *n*-heptane mixtures were predicted using the excess volume mixing rule (Saryazdi *et al.*, 2013), given by:

$$\rho_{mix} = \left[\frac{w_{C7}}{\rho_{C7}} + \frac{w_{bit}}{\rho_{bit}} - w_{C7}w_{bit}\left(\frac{1}{\rho_{C7}} + \frac{1}{\rho_{bit}}\right)\beta_{C7-bit}\right]^{-1} \quad (3.2)$$

where ρ_{mix} is the mixture density, ρ_{C7} is the density of *n*-heptane, and ρ_{bit} is the density of the WC-B-A3 bitumen, w_{C7} is the weight fraction of *n*-heptane in the mixture, w_{bit} is the weight fraction of bitumen in the mixture, and β_{C7-bit} is the density binary interaction parameter between

the solvent and bitumen. The last term on the right-hand side of the expression is the excess density of mixing.

The effective density of *n*-heptane was calculated using the following correlation, (Saryazdi *et al*., 2013):

$$\rho_{C7} = (a_1 + a_2 T) + [(b_1 + b_2 T)P] \quad (3.3)$$

where ρ_{C7} is the effective density of *n*-heptane, a_1, a_2, b_1, and b_2 are parameters specific to the fluid, *T* is the absolute temperature in K, and *P* is the pressure in MPa. The effective density is the density of a component when it is part of a liquid mixture. It is used in the mixing rule when components are gases or near their critical condition in their native state. For a component that is a liquid far from its critical point, the effective density is equal to the component density in its native state. The parameters specific for *n*-heptane are listed in Table 3.3.

Table 3.3. Effective density parameter for n-heptane (Saryazdi et al. 2013). Effective density parameter for *n*-heptane (Saryazdi *et al*., 2013).

Parameter	a_1 kg/m^3	a_2 kg/(m^3·K)	b_1 kg/(m^3·MPa)	b_2 kg/(m^3·MPa·K)
n-heptane	918.603	-0.79155	-0.17738	0.002692

The density of the WC-B-A3 bitumen, previously measured by Grimaldo-Aguilar (2018), was fitted with the following expression (Saryazdi *et al*., 2013):

$$\rho_{bit} = (A - BT)exp\{Cexp(DT)[P - 0.1]\}$$

where *A, B, C,* and *D* are fitting parameters. The parameter values are provided in Table 3.4.

Table 3.4. Fitting parameters for WC-B-A3 bitumen in density correlation (Do et al., 2022).

Parameter	*A* kg/m^3	*B* kg/(m^3·K)	*C* 1/MPa	*D* 1/K
n-heptane	1196.2	0.63743	0.00014	0.00433

The binary interaction parameter was determined using the following expression (Saryazdi *et al*., 2013):

$$\beta_{C7-bit} = \beta_{C7-bit}^{298} + 8.74 \times 10^{-5}(T - 298) \quad (3.4)$$

$$\beta_{C7-bit}^{298} = -0.092 \left| 0.435 - 2\left(\frac{|v_{C7298} - v_{bit298}|}{(v_{C7298} + v_{bit298})}\right)\right| + 0.022 \quad (3.5)$$

where β_{C7-bit}^{298} is the binary interaction parameter between *n*-heptane and bitumen at 298 K, v_{C7298} and v_{bit298} are the specific volume of heptane and bitumen respectively at 298 K.

The predicted densities for the *n*-heptane-bitumen mixtures at the experimental conditions encountered in this thesis are provided in Table 3.5. On average, the predicted mixture densities are expected to be within 0.7 kg/m³ of the actual value for the range of temperatures and pressures used in this thesis.

Table 3.5. Density and viscosity of WC-B-A3 bitumen and n-heptane (C7) mixtures.

C7 Content (wt%)	Temperature (°C)	Density (kg/m³)	Viscosity (mPa·s)
65	50	756.2	1.094
75	50	727.7	0.719
90	50	687.9	0.423
65	130	694.7	0.463
75	130	665.5	0.334
90	130	625.0	0.222

3.5.3 Viscosity of Mixtures of Bitumen and n-Heptane

The Expanded fluid Viscosity Model (Yarranton and Satyro, 2009; Motahari *et al.* 2013; Ramos-Pallares *et al.*, 2016) was used to calculate the viscosity of pure fluids and mixtures. The viscosity of the fluid μ is determined as a departure from dilute gas viscosity μ_D, and it is based on the empirical observation that the viscosity of the fluid decreases as it expands from a compressed state of infinite viscosity.

$$\mu - \mu_D = 0.165(\exp(c_2\beta) - 1) \quad (3.6)$$

where *T* is the temperature in K, μ is in mPa·s, μ_D is the dilute viscosity, c_2 is a parameter specific to the fluid, and β is a correlating parameter. In this study, the dilute gas viscosity is negligible

compared with the liquid density and was neglected. The correlating parameter is related to the fluid expansion and is given by:

$$\beta = \frac{1}{exp\left[\left(\frac{\rho_S^*}{\rho}\right)^{0.65} - 1\right] - 1} \tag{3.7}$$

where ρ is the fluid density and ρ_s^* is the compressed state density given by:

$$\rho_S^* = \frac{\rho_S^0}{\exp\left(-c_3 P\right)} \tag{3.8}$$

where ρ_s^0 is the compressed state density of the fluid vacuum c_3 is the pressure dependency constant specific to the fluid, and *P* is the pressure in kPa.

The fluid-specific parameters for *n*-heptane and the WC-B-A3 bitumen are listed in Table 3.6. The parameters for *n*-heptane were obtained from Ramos-Pallares *et al.* (2016). The parameters for the bitumen were obtained by fitting Eq. 3.6 to experimental data collected by Grimaldo-Aguilar (2018). The model fit the bitumen viscosity with an absolute average deviation of 2.8%, within the measurement error of 5% reported by Grimaldo-Aguilar (2018).

Table 3.6. Expanded Fluid Model fluid-specific parameters (Do, 2021).

Component	ρ_s^0 kg/m^3	c_2	c_3 10^{-3} MPa^{-1}
n-heptane	857.8	0.2130	0.17
WC-B-A3	1061.2	0.63743	0.34

To determine the viscosity of a mixture, the mixture is treated as a single component fluid but with fluid-specific parameters calculated from its individual components. The mixture parameters are determined with the following mixing rules (Motahari *et al.*, 2013):

$$\rho_{s,mix}^0 = \left[\frac{w_{C7}}{\rho_{C7}^0} + \frac{w_{bit}}{\rho_{bit}^0} - w_{C7}w_{bit}\left(\frac{1}{\rho_{C7}^0} + \frac{1}{\rho_{bit}^0}\right)\alpha_{C7bit}\right]^{-1} \tag{3.9}$$

$$\frac{c_{2,mix}}{\rho_{s,mix}^0} = \left[\frac{w_{C7}c_{2,C7}}{\rho_{C7}} + \frac{w_{bit}c_{2,bit}}{\rho_{bit}} - w_{C7}w_{bit}\left(\frac{c_{2,C7}}{\rho_{C7}} + \frac{c_{2,bit}}{\rho_{bit}}\right)\alpha_{C7bit}\right] \tag{3.10}$$

$$c_{3,mix} = \left[\frac{w_{C7}}{c_{3,C7}} + \frac{w_{bit}}{c_{3,bit}}\right]^{-1} \tag{3.11}$$

where w_{C7} is the weight fraction of *n*-heptane in the mixture, w_{bit} is the weight fraction of bitumen in the mixture, ρ_{bit} is the density of bitumen, ρ_{C7} is the density of *n*-heptane, and α_{C7bit} is the

viscosity binary interaction parameter. The binary interaction parameter is determined from the following correlation:

$\Delta SG_{norm} \leq 0.165$: $$\alpha_{C7bit} = 0.021 \quad (3.12)$$

$\Delta SG_{norm} > 0.165$: $$\alpha_{C7bit} = 0.038304 - 0.10478\Delta SG_{norm} \quad (3.13)$$

where

$$\Delta SG_{norm} = \frac{2|SG_{C7} - SG_{bit}|}{SG_{C7} + SG_{bit}} \quad (3.14)$$

The predicted viscosities for the *n*-heptane-bitumen mixtures at the experimental conditions encountered in this thesis were provided in Table 3.5. On average, the predicted mixture viscosities are expected to be within 14% of the actual value (Ramos-Pallares, 2016).

Chapter 4: Results Glassy Particle Regime

This chapter explores asphaltene deposition in a bitumen and *n*-heptane system in vertical flow. The measured excess pressure drops, deposit mass, and solvent content of the deposit are presented for experiments conducted at 50°C where asphaltenes form glassy particles. The effects of capillary tube length, solvent composition, flow rate, and pipe orientation on asphaltene deposition in vertical flow are discussed. Finally, the deposition results in vertical flow are compared with previous results for horizontal flow from Do *et al.* (2022).

4.1 Typical Deposition Experiment

Figure 4.1a shows the excess pressure drop profile for a mixture of 75 wt% *n*-heptane and 25 wt% bitumen (75:25 H:B) in a 30 cm vertical capillary tube at 50°C and a flow rate of 2.0 cm^3/min. At first glance, the data appears highly scattered but in fact, there were intermittently occurring pressure drop spikes. Each pressure drop spike consisted of an exponential increase in pressure drop over time followed by an almost instantaneous decrease to a very low excess pressure drop. For the first 80 min, there were approximately 0.3 spikes/min and the baseline pressure drop (bottom of spikes) increased gradually over time. At 80 minutes, a large spike reset the baseline pressure drop, followed by a 40 min spike-free period of gradually increasing pressure drop, and then, finally, by another spiky period with 0.09 spikes per minute. Figure 4.2b compares two runs at the same conditions and demonstrates that the observed trends were qualitatively repeatable in terms of their baseline trend and the frequency of spikes. The overall shape and pattern of the graphs were alike although the exact timing and magnitude of the spikes varied.

The mass and distribution of the deposit was measured at the end of the experiment and therefore corresponded to the final pressure spike in Figure 4.1. Table 4.1 shows that the deposit was located mainly in the middle of the tube and that its wet mass wet mass occupied 40% of the tube volume. The deposit had a solvent content of 79 wt%, as listed in Table 4.2. The high solvent content of the deposit suggests that the deposit had a highly porous structure that may have been formed from aggregated particles of asphaltenes. Note that in general, the mass and wet volume of the deposit depended on when the experiment was stopped; the larger the excess pressure drops at the end of the experiment, the larger the deposit.

The gradual increase in the baseline pressure drops and the location of the deposit is consistent with the gradual accumulation of a deposit along the length of the tube that restricted the tube's inner diameter. The pressure drop spikes are consistent with temporary blockage. It is hypothesized that floating porous clusters of asphaltene particles become trapped in the porous deposit. The obstruction causes the upstream pressure to spike until it is sufficient to blow out the obstruction. The destruction of the obstruction randomly removes some or all the surrounding deposit such that the pressure drop does not always return to the baseline. Random cycles of plugging and blowout occur as a result.

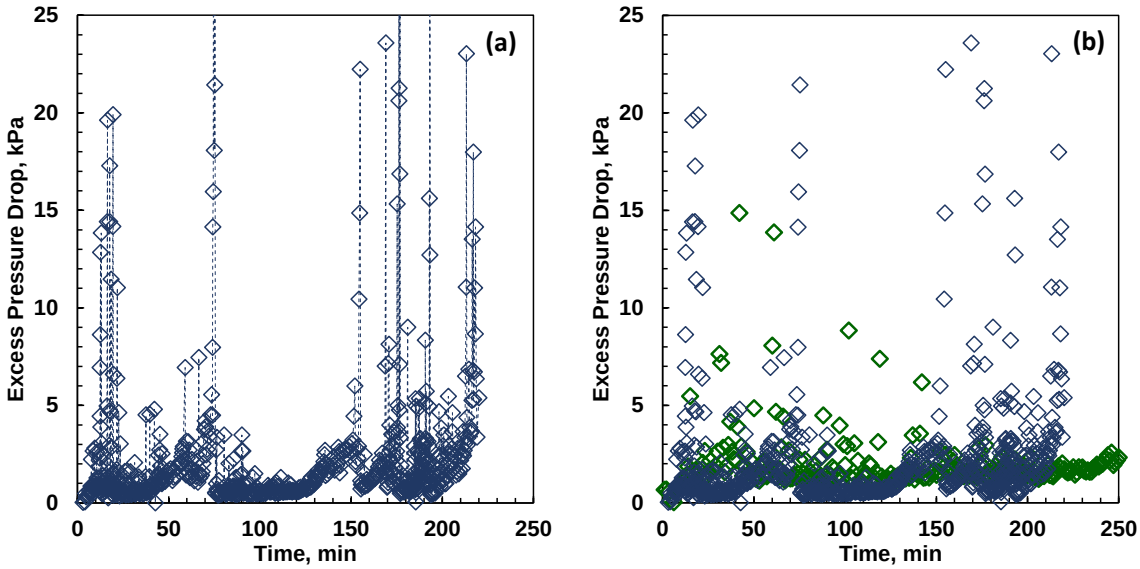

Figure 4.1. Excess pressure drop profile for a mixture of 75 wt% heptane and 25 wt% bitumen (H:B = 75:25 w/w) flowing at 2.0 cm³/min in a 30 cm (1.75 mm I.D.) capillary tube at 50°C. The uncertainty of the pressure is ±0.33 kPa.

Table 4.1. The total mass of dried deposit and tube volume occupied by wet mass in a (1.75 mm I.D) capillary tube at 50°C. The uncertainties of the total and segment masses are ± 5 mg and ± 7 mg. The dashed entries correspond to deposits that were too small to measure the mass distribution.

H:B Ratio w/w	Tube Length cm	Flow Rate cm³/min	1st mg	2nd mg	3rd mg	4th mg	Total mg	Tube Occupied %
65:35	30	2	-	-	-	-	13	19
75:25	30	2	-1.0	10.9	9.4	5.6	25	31
90:10	30	2	-	-	-	-	6	17

75:25	15	2	-	-	-	-	9	28
75:25	3	2	-	-	-	-	4	58
75:25	30	4	-	-	-	-	9	23
75:25	30	8	-	-	-	-	15	29

Table 4.2. Solvent content of deposits in a (1.75 mm I.D) capillary tube at 50°C. The uncertainty of the solvent content is ± 10 wt%.

H:B Ratio w/w	Tube Length cm	Flow Rate cm^3/min	Solvent Content of Deposit wt%
65:35	30	2	81
75:25	30	2	79
90:10	30	2	84
75:25	15	2	84
75:25	3	2	78
75:25	30	4	88
75:25	30	8	82

4.2 Effect of Capillary Tube Length

One way to test the proposed deposition mechanism of the localized deposit is by looking at different tube lengths. If the detectable deposition is caused by temporary blockages, the excess pressure drop across the capillary should show similar spikes and little change in the baseline regardless of the capillary tube length. On the other hand, if asphaltenes form a uniform deposit along the entire length of the tube, the pressure drop will increase proportionally with the tube length. Figure 4.2 shows that the length of the test section did not affect the pressure drop profile, consistent with a localized blockage.

The total mass of the deposit in the capillary tubes for a 75:25 H:B feed is presented in Table 4.1. For the 3 and 15 cm tubes, there was insufficient deposit mass to determine its distribution. The 3 cm tube was too small to do so. In the 15 cm tube, the experiment ended near the bottom of a pressure spike when the deposit was small. The small size of the deposit in the 15 cm tube (only 36% of the tube volume) argues against a uniform deposit. Table 4.2 shows that the solvent content of the deposit was the same in all cases, within the uncertainty of the measurement (±10 wt%). In other words, highly porous deposits were observed in all cases.

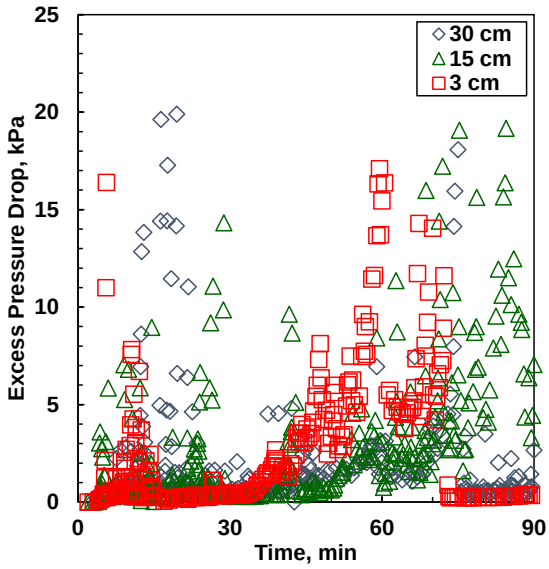

Figure 4.2. Excess pressure drop profile at 50°C and 2.0 cm³/min in a 1.75 mm I.D. capillary tube at 50°C with different capillary tube lengths. Only the first 90 min are shown for ease of comparison. The uncertainty of the pressure is ± 0.33 kPa.

4.3 Effect of H:B Ratio of the Feed

The results displayed up until now are for a feed with an H:B ratio of 75:25 w/w. As indicated by Do *et al.* (2022) altering the H:B ratio has a significant impact on asphaltene deposition, through its effect on particle concentration and adhesion forces. Each factor is discussed below.

Higher amounts of precipitate increase the supply of potentially depositing material and may lead to faster deposition rates (Vilas Bôas Fávero *et al*., 2016). However, as the size of the precipitated particles increases beyond a critical size, they become less likely to form deposits because fluid can transport them away due to their inertia (Eskin *et al*., 2011; Eskin *et al*., 2012; Hoepfner *et al.*, 2013). Duran *et al.* (2019) studied the concentration of asphaltene-precipitated particles and aggregates in mixtures of bitumen and *n*-heptane. The primary particles had a diameter between 200 nm to 1.5 μm. They assumed that the diameter of the primary particles was independent of the H:B ratio. In this case, the number of primary particles is proportional to the concentration of precipitated asphaltenes, which reached a maximum at an H:B ratio of approximately 75:25 w/w, as was shown in Section 3.3. These primary particles flocculate into aggregates within the first 30 seconds after precipitation (Ferworn *et al*., 1993; Maqbool *et al*., 2011; Duran *et al*., 2018). For

diluted bitumen with *n*-heptane, the number and size of aggregates increased with increasing H:B ratio up to approximately 80:20 w/w. At higher H:B ratios, the size of the aggregates reached a plateau and the number of aggregates decreased. If the concentration of the aggregates dominates the deposition process, the deposition rate would be expected to peak at an H:B ratio of 80:20 w/w. If the size of the aggregates determines the probability of deposition, then the deposition rate would reach a minimum at a 65:35 H:B ratio.

The adhesion force between the particles and the tube surface is related to the attractive forces between particles because the tube surface is almost certainly coated with a molecular layer of adsorbed asphaltenes (Alboudwarej *et al.*, 2005). Zhang *et al*. (2016) performed surface force measurements, showing that the bond strength between asphaltene films in solutions of *n*-heptane and toluene increased as the *n*-heptane content increased. Greater adhesion forces between the particles and tube surface accelerate deposition. Therefore, if adhesion forces dominate, deposition is expected to increase as the H:B ratio increases, and the medium becomes less compatible with the asphaltenes.

In this thesis, the deposition rate was not measured directly. Instead, it was assessed indirectly from the increase in pressure drop over time. Figure 4.3 illustrates the excess pressure drop for experiments conducted with three different H:B ratios. The baseline pressure drop increased at the same rate over time for all three H:B ratios. The baseline deposition indicated how much of the local deposit was removed after a blockage was displaced. The consistent results suggest that the material near the tube wall had similar properties at all H:B ratios.

In contrast, the frequency of the pressure spikes increased as the H:B ratio increased; specifically, 0.09, 0.15, and 0.36 spikes per minute at H:B ratios of 65:35, 75:25, and 90:10 w/w, respectively. In other words, blockage occurred more rapidly at higher H:B ratios. The spike rate did not reach a maximum at the maximum asphaltene particle concentration at an H:B of 75:25 w/w. Instead, the spike rate increased monotonically as the H:B ratio increased. It appears that the deposits built up more rapidly at higher H;B ratios, consistent with greater adhesion. Another possible explanation is that the deposits became localized at higher H:B ratios, causing more rapid local build up and more frequent blockages. In addition, the aggregates at H:B of 65:35 were expected

to be smaller than at the higher ratios (Duran *et al*., 2018), potentially reducing the blockage frequency.

Table 4.1 shows the total mass of the deposit in the capillary tube at the three different *n*-heptane compositions. The absolute masses for the deposits differed because the experiments ended at different points in the cycles of deposition and erosion in each case. For the H:B ratios of 65:35 and 90:10 w/w, there was insufficient deposit mass to determine its location. Table 4.2 shows that the solvent content of the deposit was approximately 81 wt% in all cases, consistent with highly porous deposits.

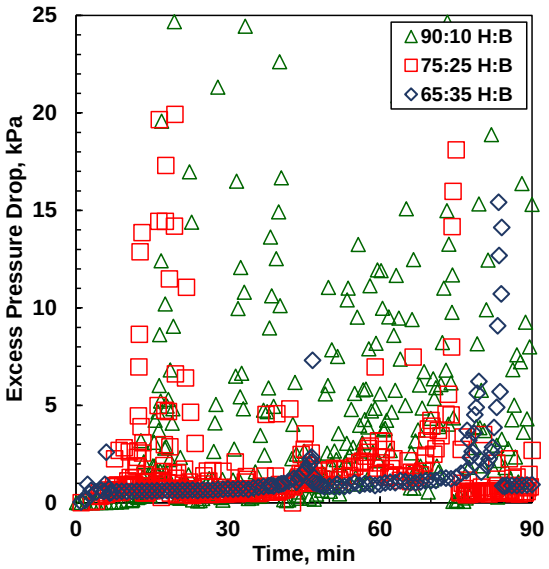

Figure 4.3. Effect of feed composition on the excess pressure drop profile in a 30 cm (1.75 mm I.D.) capillary tube at 50 °C and 2.0 cm3/min. Only the first 90 min are shown for ease of comparison. The uncertainty of the pressure is ± 0.33 kPa.

4.4 Effect of Flow Rate

The flow rate can impact deposition in several competing ways including the following (Do *et al.*, 2022):

- A higher flow rate conveys more particles within a given time which can increase the deposition rate.
- A higher flow rate (higher Reynolds number) can enhance diffusion and increase the deposition rate.

- A higher flow rate gives a higher velocity which causes more erosion due to the increased shear. Higher shear leads to a smaller deposit. Therefore, a higher flow rate can reduce the steady-state deposition rate.
- A higher velocity reduces the thickness of the boundary layer. If only the asphaltenes in the boundary layer form the deposit, a higher flow rate can decrease the deposition rate.

In this thesis, asphaltene deposition was investigated at flow rates of 2.0 cm^3/min, 4.0 cm^3/min, and 8.0 cm^3/min. For a clean pipe the Reynold numbers were 26, 55, and 103, respectively, and the corresponding shear rates were 55, 117, and 221 1/s. Since the mass of particles entering the tube depends on the flow rate, the runs performed at different flow rates were plotted against cumulative injection instead of elapsed time, as shown in Figure 4.4. The baseline pressure drop increased at the same low rate for all three flow rates indicating that the fraction of the feed forming the deposit was independent of the flow rate for the investigated range. However, the frequency of the excess pressure drops spikes decreased as the flow rate increased. A possible explanation is that the deposits become localized at low flow rates, causing more rapid local build-up and frequent blockages. At high flow rates, the deposit may have spread out more, requiring more volume injected to create a blockage. In addition, higher shear rates may lead to less porous aggregates with lower effective diameters and less potential to create a blockage. Hence, the changes in flow rate did not appear to change the deposition rate but did change the potential to form blockages.

Table 4.6. shows the mass distribution of the deposit at the different flow rates. The effect of flow rate on the amount of deposition is inconclusive, as the absolute masses for the deposits are dependent on the endpoints in each experiment, and the endpoints are dictated by the cycles of deposition and erosion. Table 4.7 shows that the solvent content of the deposit is similar across all test sections. The difference is within the uncertainty of the measurement (±10 wt%).

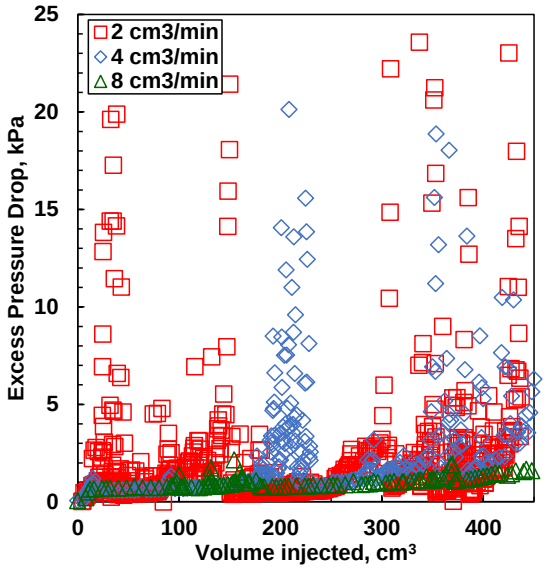

Figure 4.4. Excess pressure drops as a measure of elapsed time in terms of the volume injected in a 30 cm (1.75 mm I.D.) capillary tube for a 75:25 H:B mixture at 50 °C. The uncertainty of the pressure is ± 0.33 kPa.

4.5 Comparison with Horizontal Flow

In a previous study, asphaltene deposition in horizontal flow was investigated at the same conditions examined in this thesis (Do *et al.*, 2022). In horizontal flow, asphaltene particles and aggregates settle orthogonally to the flow direction and are expected to deposit mainly on the bottom of the tube. In vertical flow, they settle opposite to the flow direction and are expected to deposit all around the inner wall of the tube. To assess the impact of the flow orientation, the results for vertical flow from this thesis were compared with data from Do *et al*.

Figure 4.5 compares the excess pressure drops over time in vertical and horizontal flow at 2 cm^3/min in a 30 cm tube at three different H:B ratios. The pattern of pressure drops in horizontal and vertical flow were qualitatively similar with generally upward trending baselines and intermittently distributed pressure drop spikes. The baseline trends were similar in both flow orientations. The frequency of the pressure spikes was higher in vertical than horizontal flow, particularly at an H:B of 75:25 w/w. The relative velocity of the asphaltene aggregates is expected to be lower in vertical flow because gravity force acts opposite to the flow direction. The lower velocity may allow blockages to occur more readily.

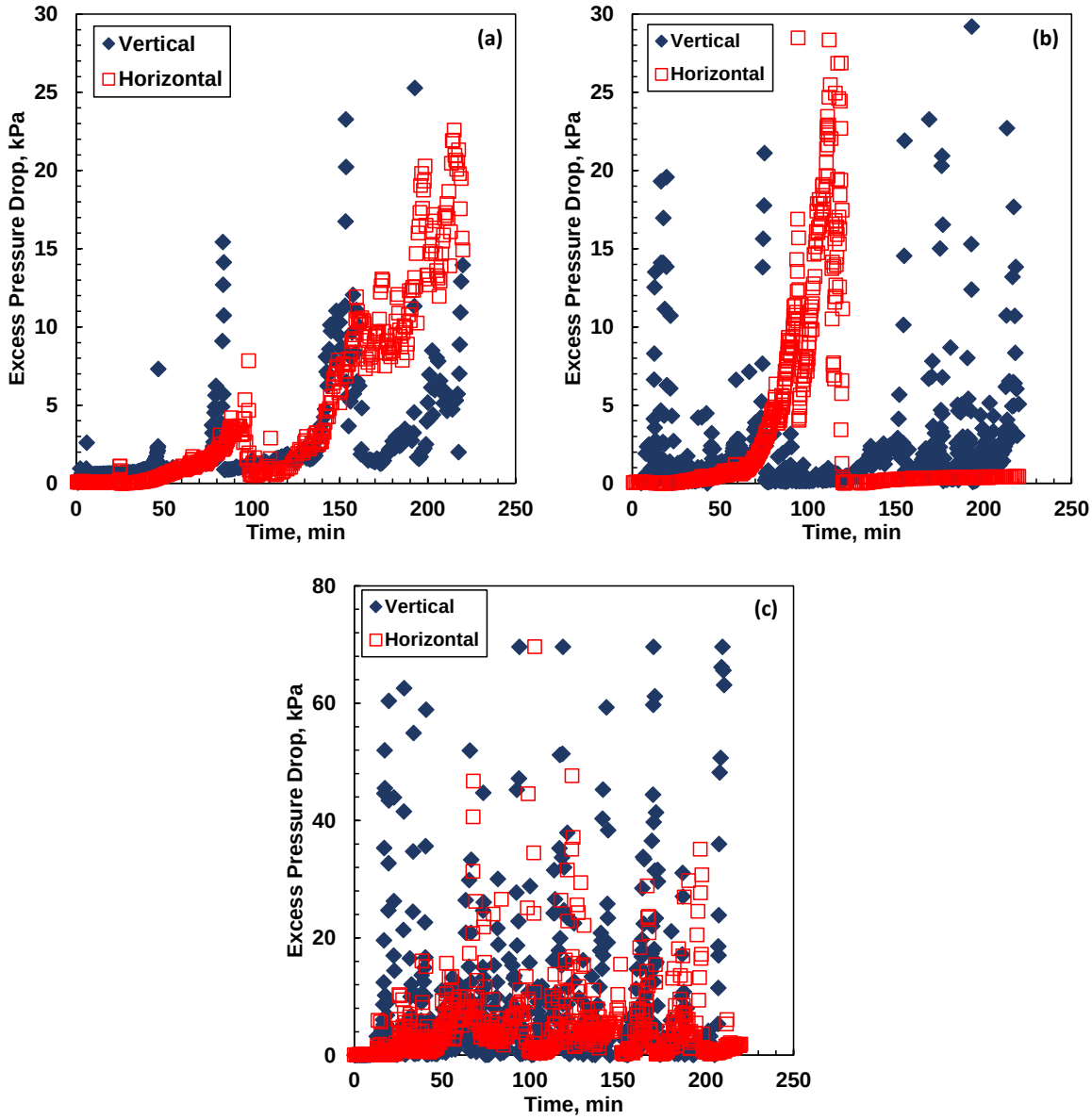

Figure 4.5. Comparison of excess pressure drop profiles at 50°C in a 30 cm capillary tube at a flow rate of 2.0 cm³/min: a) H:B = 65:35 w/w; b) H:B = 75:25 H:B w/w; c) H:B = 90:10 w/w. The uncertainty of the pressure is ± 0.33 kPa.

Do *et al.* (2022) also observed that asphaltene deposition in horizontal flow in the glassy particle regime resulted in localized deposits rather than uniform deposits. The deposit formed from the inlet and occupied up to ¾ of the tube. The deposits were found to be highly porous, with approximately 85 wt% solvent content. The deposits formed in vertical flow were very similar to the horizontal flow deposits. Unfortunately, the vertical distribution of the mass could not be

evaluated in most cases. However, due to the small size of the deposit, which only occupies a small section of the capillary tube, it is evident that it is a localized deposit.

In conclusion, the buildup of localized highly porous deposits with cycles of blockage and blowout occurred in both horizontal and vertical flow. The only notable difference was a higher frequency of blockages in vertical flow.

4.6 Summary

In the glassy particle regime for both horizontal and vertical flow, highly porous deposits formed with cycles of blockage and blowout. The deposits were localized and occupied at most 40% of the tube volume with solvent contents of 82 ±10 wt%.

Blockages occurred more frequently at higher H/B ratios, consistent more rapid deposition resulting from higher adhesion forces. Increased asphaltene aggregate size at higher H/B ratios may also increase the blockage rate. Blockages occurred more frequently in vertical flow compared to horizontal flow. In addition, the frequency of the blockages decreased at higher flow rates. Both observations suggest that blockage occurred more frequently at lower shear rates. The blockage occurred more frequently at higher H:B ratios. A possible explanation is that more localized deposits formed at higher H/B ratios.

Chapter 5: Results Liquid Droplet Regime

In the liquid droplet regime, a liquid-heavy phase accumulates in the tube and the process is therefore described here as accumulation instead of deposition. This chapter presents the measured excess pressure drop, accumulated mass of the heavy phase, and solvent content of the accumulation for vertical flow in a bitumen and *n*-heptane system at 130°C, where the asphaltene-rich phase comes out of the solution as liquid droplets. The impact of solvent content (H:B ratio), flow rate, and capillary tube length on asphaltene accumulation are discussed. Finally, the results for vertical flow are compared with previous results for horizontal flow from Do *et al.* (2022).

5.1 Typical Accumulation Experiment

Figure 5.1 shows the excess pressure drop for a mixture of 75 wt% *n*-heptane and 25 wt% bitumen (H:B = 75:25 H:B w/w) in a 30 cm vertical capillary tube at 130°C and a flow rate of 2.0 cm^3/min. Figure 5.1a shows that the excess pressure drop increased exponentially for approximately 30 minutes and then cycled between 40 and 70 kPa. The excess pressure drops spikes tend to appear at nearly regular intervals of 0.44 spikes per minute. Figure 5.1b shows that the bottom end of the pressure cycles decreased over time until, at 100 min, the bottom end reached almost zero. After 100 min, the pressure cycles all spanned a range of 0 to 70 kPa. Figure 5.1b shows the pressure drop behavior was qualitatively repeatable. For ease of visualization, only pressure drop data up to 100 minutes will be considered henceforth unless otherwise noted. The mass distribution data was collected at the end of each run, typically at 210 minutes.

Table 5.1 shows the mass distribution of the material along the capillary tube after the tube was dried and cut into four equal segments. The accumulated material was uniformly and annularly distributed along the length of the capillary tube. Table 5.2 shows that the accumulated material had an average solvent content of 44 wt% at 75:25 H:B. The heptane content is consistent with heavy phase compositions reported in phase behavior experiments performed with mixtures of bitumen and *n*-pentane (Johnston *et al.,* 2017). Hence, the heavy phase is the annular fluid. The accumulated material occupied between 41 to 100% of the pipe volume on a wet basis. The higher volume fractions corresponded to higher final pressure drops.

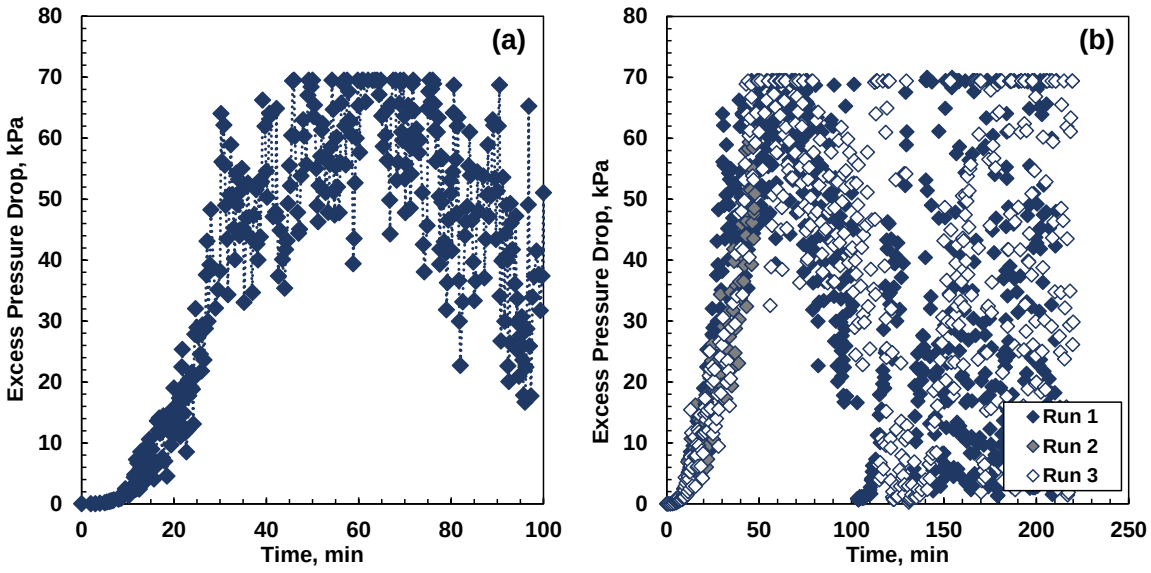

Figure 5.1. Excess pressure drop over time for a mixture of 75 wt% n-heptane and 25 wt% bitumen (75:25 H:B) flowing at 2.0 cm³/min in a 30 cm (1.75 mm I.D.) capillary tube at 130°C: a) example profile up to 100 min; b) comparison of three runs for the complete duration. The uncertainty of the pressure is ± 0.33 kPa.

Table 5.1. Mass distribution of dried deposit at 130°C. The uncertainty of the masses is ± 7 mg.

H:B w/w	Tube Length cm	Flow rate cm³/min	1st mg	2nd mg	3rd mg	4th mg	Total mg	Volume Occupied %
75:25	30	2.0	47	44	14	-4	101	41
75:25	30	2.0	92	53	48	48	242	83
75:25	30	2.0	14	46	6	11	77	57
75:25	15	2.0	87	-	-	89	176	100
75:25	3	2.0	-	-	-	-	28	34
65:35	30	2.0	21	9	4	-2	31	75
90:10	30	2.0	63	72	65	25	224	87
75:25	30	4.0	44	42	4	12	102	39
75:25	30	8.0	84	79	71	90	324	88
75:25	30	4.0	81	87	74	80	322	100

Table 5.2. Solvent content of deposits at 130°C. The uncertainty of the solvent content is ± 10 wt%.

H:B w/w	Tube Length cm	Flow rate cm^3/min	Solvent Content of Deposit wt%
75:25	30	2.0	40
75:25	30	2.0	40
75:25	30	2.0	51
75:25	15	2.0	30
75:25	3	2.0	31
65:35	30	2.0	66
90:10	30	2.0	38
75:25	30	4.0	40
75:25	30	8.0	31
75:25	30	4.0	37

There is a high viscosity contrast between the asphaltene-rich heavy phase and the solvent-rich light phase. Therefore, it is likely that a core annular flow regime was established. The mixture likely entered the capillary tube as a dispersion, but the heavy phase started to accumulate at the tube wall. Eventually, an annulus of the heavy-phase was formed and grew thicker causing the exponential rise in pressure drop. As the heavy phase accumulated, the effective diameter for the light phase flow decreased and the light phase velocity increased. The difference in the velocity and viscosity of the core and annulus is expected to create waves at the interface (Bannwart, 1998). It appears that the wave crests eventually connected with each other to create a plug. Each time a plug formed it was eventually blown out, leading to cycles of accumulation and blowout.

The reason for the change in the bottom pressure drop of the pressure cycles is less clear. It is known that wavy annular flow can be disturbed with an increase in the velocity of the core and can evolve towards slug flow (Bannwart *et al*., 2004). The change in behavior between 30 to 100 min may be such a transition. It appears that once slug flow was established at 100 min, the flow regime remained as slug flow. A possible explanation for the bottom cycle pressure trend and the persistence of slug flow is that some of the annular heavy phases were left attached to the wall of the capillary tube after each pressure spike. The amount of residual heavy phase volume could be significant because the pressure drop only becomes detectable when the annular phase occupies

approximately 13% of the pipe volume. This annular material may have originally contained some entrained solvent and have a modest viscosity, leading to small slugs which can be displaced without much disturbing the annulus. Over time the entrained material in the annulus may be displaced, leaving a more viscous phase that leads to larger slugs.

External factors were also considered as an explanation for the change in the flow regime. One possible external factor is that backflow occurred after 100 minutes. Backflow refers to a reversal in the direction of flow. In the apparatus used for asphaltene deposition with the vertical flow, there is a change in diameter from 1.7 mm ID to 4.6 mm ID at the exit of the capillary tube. This change in diameter results in a significant increase in the pipe size. However, at the minimum flow rate used in this thesis, the fluid velocity would be 84.6 cm/min, making backflow unlikely. In fact, the high velocity and pipe diameter increase would likely promote flow in the intended direction. Another possibility is that the heavy phase accumulated before the capillary inlet and occasionally releases clumps into the capillary tube. The clumps could cause a blockage and pressure spike. However, the mass of the heavy phase required to fill the fittings before the inlet is too high to be accumulated within the time of the experiment. Therefore, it was concluded that the changes in the flow regime were a natural evolution of the flow regime in vertical flow through the capillary tube.

5.2 Effect of Capillary Tube Length

In the glassy particle region, the deposit was localized, and the pressure drop was independent of the length. In contrast, in the liquid droplet regime, the deposition mechanism is heavy phase accumulation along the length of the capillary tube, and therefore the pressure drop is expected to be proportional to the tube length.

Figure 5.2a shows the excess pressure drop over time for a 75:25 H:B feed flowing at 2 cm^3/min in three different tube lengths. In all cases, the excess pressure drops increased with time as the heavy phase accumulated and eventually exhibited periodic fluctuations. As expected, the maximum pressure drop increased as the tube length increased. Figure 5.2.b shows that the pressure gradients for the three runs were almost identical over time, indicating that the liquid holdup developed similarly for all cases and that the accumulation was spread along the tube

length. Table 5.1 confirms that the mass of the deposit was the same in each tube section for the 15 and 30 cm tubes. There are only two entries for the 15 cm tube because it was cut in half not quarters. The 3 cm tube was too short to measure the distribution. Table 5.2 shows that the solvent content of the deposit was similar for the three runs with a value of approximately 34 wt%.

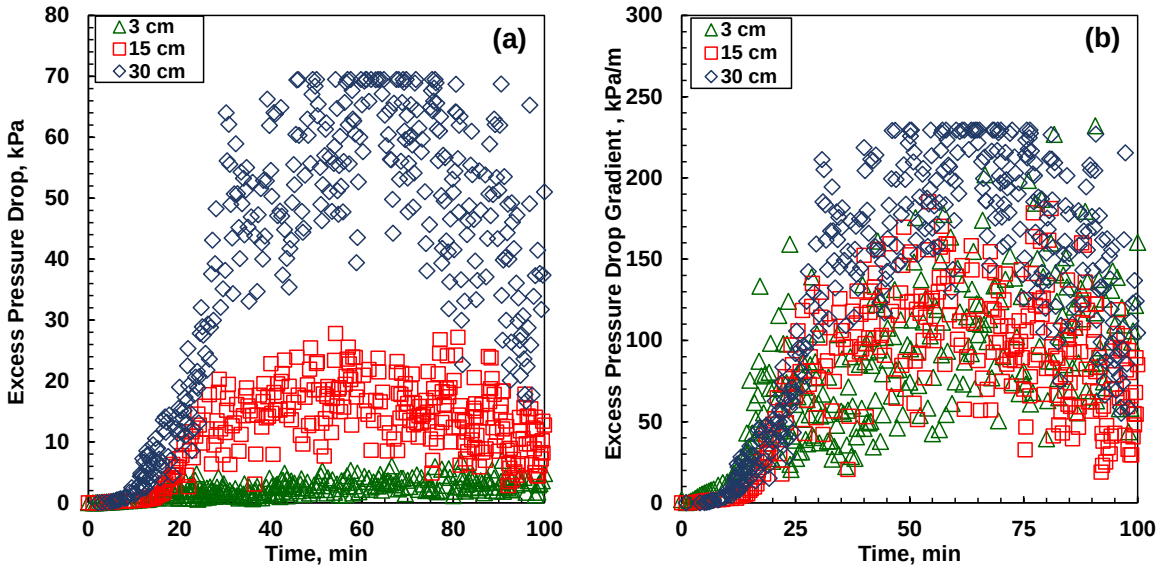

Figure 5.2. Effect of capillary tube length on: a) excess pressure drop profile; b) pressure gradient profile; 75:25 H:B mixture at 130°C and a flow rate of 2.0 cm³/min. The uncertainty of the pressure is ± 0.33 kPa.

5.3 Effect of H:B Ratio of the Feed

The H:B ratio of the feed can impact heavy phase accumulation in several ways. A key factor is that the H:B ratio of the feed determines the heavy phase concentration in the mixture. It has been shown that the amount of heavy phase formed at a given H:B ratio is insensitive to temperature (Perez-Claro, 2019). Therefore, the maximum in heavy phase content is expected to occur near the maximum in asphaltene yield observed at 20°C (see Figure 3.3); that is, at an H:B ratio of 75:25 w/w. If the heavy phase content is the dominant factor in the accumulation, the maximum accumulation rate would also occur at an H:B ratio of 75:25 w/w. Another factor is that an increase in the H/B ratio leads to stronger attraction forces between droplets, and droplets and walls, resulting in more rapid accumulation. In this case, the most rapid accumulation would be expected at the highest H:B ratio. The viscosity ratio of the two-phase also impacts the type of flow regime

and transitions from one flow regime to another. The most viscous light phase, and therefore the lowest viscosity ratio, occurs at an H:B ratio of 65:25.

Figure 5.3 shows the excess pressure drop over time with three different H:B ratios in a 30 cm tube and a flow rate of 2 cm^3/min. The first exponential increase in pressure drop occurred at 25 min for the 75:25 H:B and 90:10 H:B feeds but not until after 100 min for the 65:25 H:B feed (not shown in the figure). Hence, the accumulation rate was low for a 65:25 H:B feed and high for both the 75:25 and 90:10 H:B feeds. It appears that several factors determine the accumulation rate. At 65:25 H;B, the viscosity contrast between the light and heavy phases was at its lowest. In this case, the lower velocity, lower shear, and similar densities of the light phase and heavy phase would decrease the rate at which the droplets reach the wall, leading to the dispersed flow regime persisting longer with a much slower transition to annular flow. At the higher H:B ratios, the viscosity contrast was significant, and core annular flow may have been established quickly. The accumulation rate peaked at the expected H:B ratio of 75:25. The accumulation nonetheless remained high at the 90:10 H:B feed even though the heavy phase content was low, likely because the attractive forces between the droplets was high.

Tables 4.1 and 4.2 show the mass distribution and solvent content of the deposits, respectively, for the three feeds. For the 75:25 H:B and 90:10 H:B feeds, the heavy phase occupied almost all of the tube. In both cases, the solvent content of the heavy phase was approximately 40 wt%, as expected. However, the 65:35 H:B feed showed less uniform mass distribution along the tube and a higher solvent content of 66 wt%. In this case, the accumulated mass was low suggesting that core annular flow was not yet established. The higher solvent content suggests that there was some entrainment of the light phase in the initially localized accumulation.

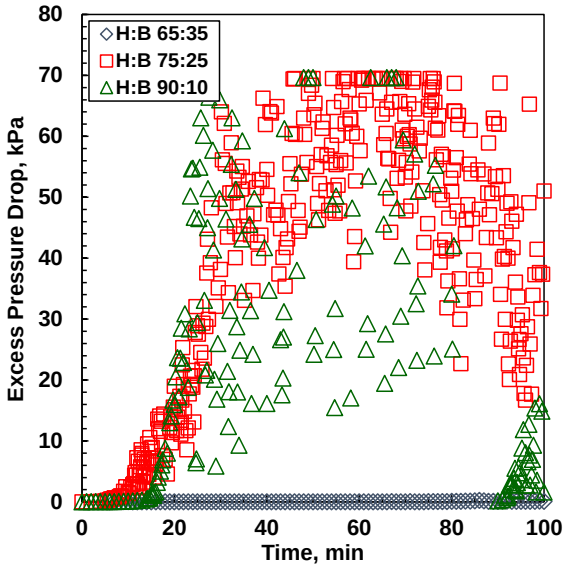

Figure 5.3. Effect of feed composition on the excess pressure drop profile in 30 cm (1.75 mm I.D.) capillary tube at 130 °C and 2.0 cm3/min. Only the first 100 min are shown for ease of comparison. The uncertainty of the pressure is ± 0.33 kPa.

5.4 Effect of Flow Rate

The flow rate can impact heavy phase accumulation in several ways. A higher flow rate increases the amount of heavy phase entering the tube per time, which can lead to a higher accumulation rate. In addition, higher flow rates produce higher velocities and shear forces that promote dispersed flow which could lead to lower accumulation or deposition rather than accumulation. Since the velocity can impact the accumulation rate, it can impact the timing of the transition from one flow regime to another.

Figure 5.4 compares the excess pressure drop for 2.0, 4.0, and 8.0 cm^3/min for an H:B ratio of 75:25 w/w in a 30 cm capillary tube. The Reynolds numbers were 50, 107, and 201, respectively, and the corresponding shear rates were 55, 117, and 221 1/s. Figure 5.4a shows that the initial exponential increase in pressure drop over time was independent of the flow rate, suggesting that the increase in shear rate counteracted the increase in the heavy phase entering the capillary tube per time. Figure 5.4b shows how the pressure drop increases more rapidly versus cumulative injection at lower flow rates, confirming that a higher fraction of the heavy phase accumulates at lower shear. The subsequent pressure drop cycles were similar at 2 and 4 cm^3/min (approximately 0.4 spikes per minute), suggesting little difference in the flow regimes and flow transitions.

However, at 8 cm³/min, the initial exponential increases ended sooner, and the pressure drop cycles were less frequent. It appears that the transition from core annular flow to plugging or slug flow was sensitive to the flow rate. Table 5.1 shows that, in all cases, the heavy phase was uniformly spread through the tube. Table 5.2 shows that the solvent content of the heavy phase was again consistent with the heavy-phase compositions in the literature.

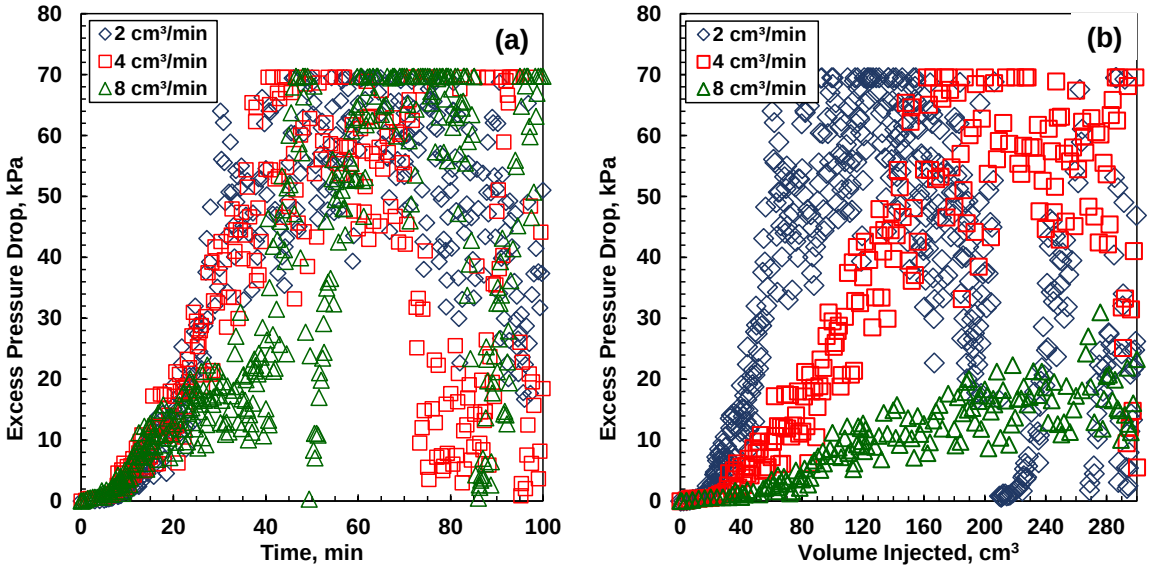

Figure 5.4. Effect of feed flow rate on the excess pressure drop profile for a 75:25 H:B in a 30 cm (1.75 mm I.D.) capillary tube at 130 °C: a) versus time; b) versus volume injected. The uncertainty of the pressure is ± 0.33 kPa.

5.5 Comparison with Horizontal Flow

In a previous study, heavy phase accumulation in the liquid droplet regime was investigated for horizontal flow (Do *et al.*, 2022). The nature of the accumulated heavy phase was the same in horizontal and vertical flow. In both cases, the heavy phase was distributed throughout the length of the tube. The solvent content of the heavy phase was approximately 30 wt% in the horizontal flow compared with approximately 40 wt% in the vertical flow. The difference was within the uncertainty of the measurement (±10 wt%). Note that in the horizontal flow experiments, pressure spikes were observed that exceeded the maximum differential pressure limit of the transducer (70 kPa). In these cases, the pump displacement pressure was used to measure the differential pressures above 70 kPa, after adjustment for the back pressure and the friction losses caused by the piston in the cylinder.

Although the heavy phase is the same for the horizontal and vertical flow experiments, there may be some differences in how the heavy phase accumulated. In horizontal flow, the droplets of the heavy phase settle perpendicularly to the flow direction, which allows the liquid droplets to coalesce and accumulate at the bottom of the tube. On the other hand, in vertical flow, they settle in the opposite direction of the flow and are expected to accumulate on all sides of the inner wall of the tube.

Figure 5.5 compares the excess pressure drops over time in vertical and horizontal flow at 2 cm^3/min in a 30 cm tube at three different H:B ratios. The full duration of each run is shown to facilitate the comparison. At an H:B of 65:35 w/w, the pressure drop profiles versus time for horizontal and vertical flow were very similar; that is, the accumulation rate was the same despite the different orientation. The similarity raises the possibility that the settling rate of the heavy phase was low and the accumulation took place all around the tube circumference in both cases. A low settling rate is plausible at the relatively low H:B ratio because the contrast between the phase densities is at its lowest. There is also a relatively low concentration of heavy phase and a lower driving force for coalescence than at the higher H:B ratios. Hence, the droplets are likely to stay dispersed. The flow regime in the horizontal orientation was originally interpreted as stratified flow but may in fact be annular.

At an H:B ratio of 75:25 w/w, the contrast in phase densities is significant and stratified flow is likely in the horizontal orientation. In this case, the initial accumulation occurred much more rapidly in vertical versus horizontal flow and there was more frequent pressure drop spikes. The velocity of the heavy phase droplets relative to the tube wall and to the light phase will be lower in vertical flow than in horizontal flow. It is possible that accumulation occurred more rapidly with the lower relative velocity which would allow more time for coalescence and adherence. The lower relative velocity may also facilitate plugging, leading to more frequent pressure drop spikes.

At an H:B of 90:10 w/w, the initial accumulation rate was similar for the two orientations. There was more frequent pressure drop spikes in vertical flow, but the maximum pressure drop tended to be lower after 100 min. In this case, the forces driving coalescence and adherence may have

been strong enough to cause rapid accumulation even in the horizontal configuration. The low relative velocity of the heavy phase would still facilitate more rapid plugging in vertical flow.

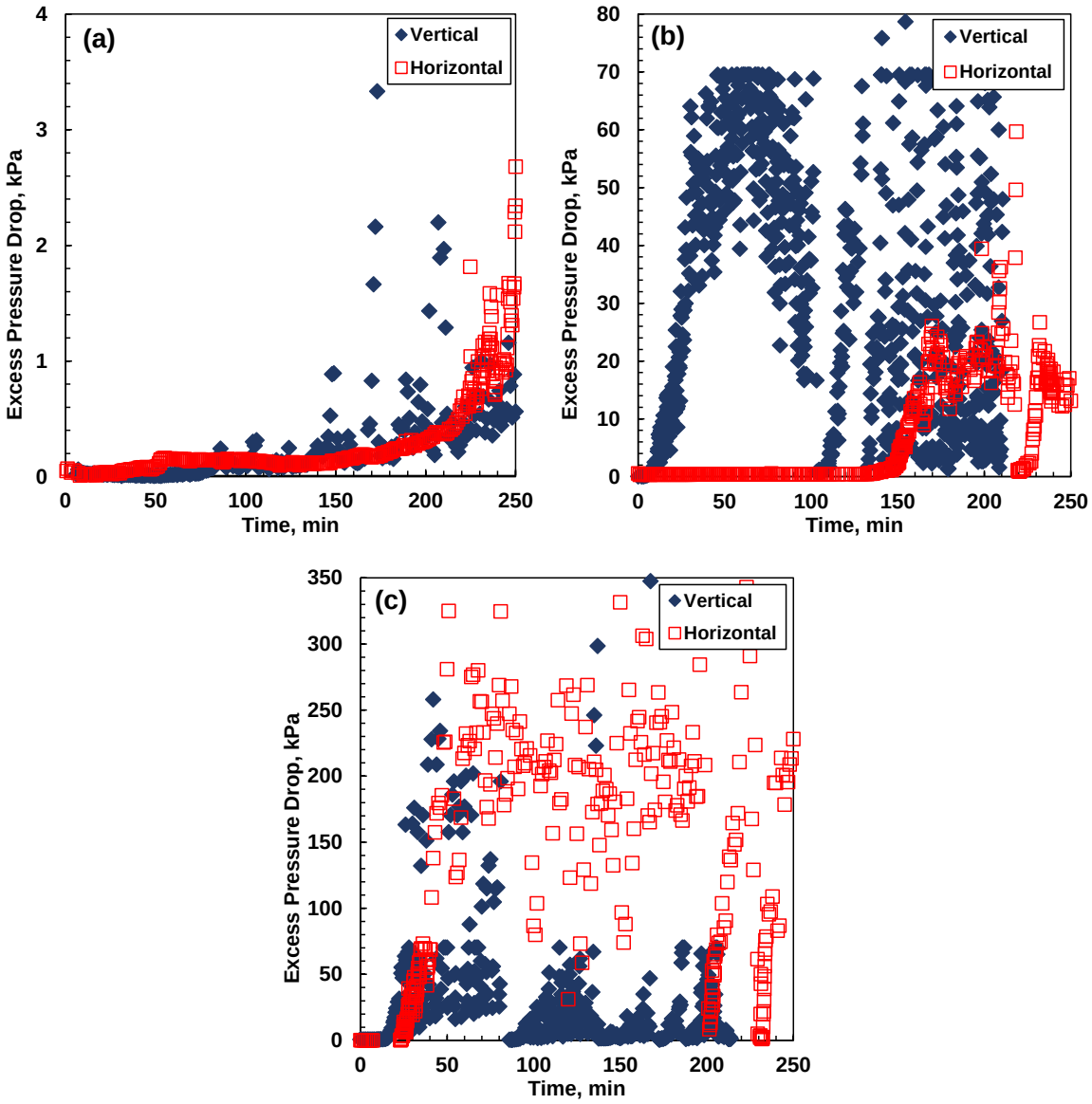

Figure 5.5. Comparison of excess pressure drop profiles at 130 °C in a 30 cm (1.75 mm I.D.) capillary tube at 2.0 cm^3/min: (a) 65:35 H:B mixture; (b) 75:25 H:B; (c) 90:10 H:B mixture. Note the y-axis scale for panel (a) is different than the other two panels. The uncertainty of the pressure is ± 0.33 kPa.

5.6 Summary

In the liquid flow regime for vertical flow, the fluid likely entered the capillary tube as a dispersed phase, but the heavy phase gradually accumulated at the tube wall. A core-annular flow regime

was established, and the heavy phase hold up increased monotonically, leading to an exponential increase in pressure drop until the liquid holdup reached 80%. The heavy phase accumulation reduced the effective diameter for the light phase flow and therefore the velocity of the light phase increased. The velocity contracts between the light and heavy phase created waves at the interface. The wave crests periodically connected creating a slug flow condition with cycles of pressure build up and blow out. The heavy phase layer usually contains around 40% of solvent ± 10%, which is in line with previously reported equilibrium heavy phase compositions (Johnston *et al.*, 2017).

The heavy phase accumulation in both horizontal and vertical flow appeared to have the same nature. It accumulated throughout the entire length of the tube and had a solvent content of approximately 30 wt% in horizontal flow and about 40 wt% in vertical flow, with a measurement uncertainty of ±10 wt%. However, there may be some variations in how the heavy phase accumulated. In horizontal flow, the droplets of the heavy phase settle perpendicularly to the flow direction, allowing them to coalesce and gather at the tube's bottom. In contrast, in vertical flow, the droplets settle in the opposite direction of the flow and can accumulate on all sides of the tube's inner wall.

Chapter 6: Conclusions and Recommendations

This thesis explored whether the mechanisms of asphaltene deposition differ when the flow is horizontal or vertical in both the glassy particle (50°C) and liquid droplet (130°C) regimes. The main contribution was to confirm that the mechanism for flow disruption changes from particle deposition below the glass transition to heavy phase accumulation in the multiphase flow above the glass transition. In addition, it was shown that porous annular deposits occurred in the glass particle regime while core-annular flow and slugging occurred in the liquid droplet regime with the heavy phase accumulating in the annulus.

6.1 Conclusions

Glassy Particle Regime

The deposition mechanism in the glassy particle regime for vertical flow was similar to horizontal flow in the sense that porous deposits were formed with cycles of blockage and blowout. These deposits were localized, occupying a maximum of 40% of the tube volume with solvent contents of 82 ±10 wt%. For both horizontal and vertical flow, the baseline deposition rate was similar for all feed H:B ratios, and no dominant deposition mechanism (particle flux, particle transport, or adhesion) was identified. The only notable difference was a higher frequency of blockages in vertical flow.

In horizontal flow, the frequency of the blockages (pressure spikes) was similar for the 65:35 and 75:25 H/B feeds but was higher for the 90:10 H/B feed. Vertical flow experienced more blockages than horizontal flow with a frequency that increased as the H:B ratio increased. One explanation is that the deposition rate increased as the H/B ratio increased (consistent with greater adhesion forces), leading to more rapid build-up and consequently more frequent blockage. Another possibility is that the larger asphaltene aggregate sizes at the higher H:B ratios are more likely to form blockages. Blockages may occur more rapidly in vertical flow because the relative velocity of the aggregates to the deposit is lower due to gravity forces.

The blockages occurred more frequently at lower flow rates, that is, at lower shear rates. A possible explanation is that the deposits become localized at low shear, causing more rapid local build-up and more frequent blockage. At high shear, the deposit may have spread out more, requiring more volume injected to create a blockage. This effect may also explain the higher blockage rate at higher H:B ratios. As the H:B ratio increases, the fluid viscosity decreases, and therefore so does the shear rate. A lower shear rate leads to more frequent blockage.

Liquid Droplet Regime

The deposition mechanism in the liquid droplet flow regime was observed to be similar for both horizontal and vertical flow. The heavy phase accumulated throughout the entire length of the tube and had a solvent content of approximately 30 wt% in horizontal flow and about 40 wt% in vertical flow, with a measurement uncertainty of ±10 wt%, The solvent content is consistent with previously reported equilibrium heavy phase compositions (Johnston *et al.*, 2017).

In horizontal flow, the flow regime was interpreted as the stratified flow of a light-phase emulsion over a heavy-viscous liquid that likely included entrained solve. For this orientation, the heavy phase droplets settled perpendicular to the flow, allowing them to coalesce and gather at the tube bottom (Do, *et al.* 2022).

In vertical flow, the flow regime was interpreted as dispersed flow at the inlet with a gradual accumulation of the heavy phase along the tube wall. In this orientation, the droplets settled in the opposite direction of the flow and accumulated all around the annulus. Hence, core-annular flow developed. The heavy phase hold-up increased, causing a subsequent rise in pressure drop until the holdup reached 80%. As the heavy phase accumulated, it reduced the effective diameter of the light phase flow, causing the velocity of the light phase to increase and create waves at the interface between the two phases. These waves connected periodically, resulting in slug flow with cycles of pressure build-up and blow-out.

6.2 Recommendations

Flow patterns in two-phase flow are dictated by the balance of inertial, gravity, buoyant, and interfacial forces. Some models have been developed for the hold-up and pressure drop in the liquid-liquid core annular flow and its transition to wavy-annular. This model may be useful in predicting the accumulation of asphaltene in the liquid regime. However, some properties of the two phases are needed, such as the interfacial forces between the light phase and heavy phase and the viscosity of each phase. It is recommended to:

- measure the viscosity of the asphaltene-rich heavy phase in the liquid regime. The HOPP research group is currently working on this by separating the two phases in an oven at high temperatures, passing the sample through a viscometer, and measuring the pressure drop with a pressure gauge. This pressure drop can then be correlated with viscosity.
- measure interfacial tension at high temperatures using the pendant drop method. With this technique, a droplet of one liquid (the asphaltene-rich heavy-phase) is suspended from a needle surrounded by another liquid (the light phase). The shape of the droplet is governed by a balance of the gravity and interfacial forces; hence, the interfacial tension can be determined from the profile of the droplet. A drop shape analysis apparatus suitable for above ambient temperature and pressure would be required.

Current additives used in the industry to mitigate asphaltene deposition are designed for the glass particle regime. It is recommended to evaluate the impact of these additives on asphaltene accumulation in the liquid droplet regime.

It would be useful to determine the chemical composition of the asphaltene deposit inside the pipe to better determine its properties. For example, the asphaltene and solvent content could be used to confirm that a heavy phase formed the deposit at high temperatures. For glassy deposits, an elemental and mass spectrometry analysis may provide insights into potential chemical treatments. In the current apparatus, the mass of the deposits is too small for most such analyses. Either a larger apparatus or multiple runs could be performed to obtain sufficient sample.

It is recommended to evaluate large tube diameters in order to scale results to the field. The tests would require longer tubes and therefore would be limited to horizontal flow in order to fit in the oven.

References

Abraham, T., Christendat, D., Karan, K., Xu, Z., and Masliyah, J. (2002). Asphaltene—Silica interactions in aqueous solutions: Direct force measurements combined with electrokinetic studies. *Industrial and Engineering Chemistry Research*, 41(9), 2170–2177. https://doi.org/10.1021/ie0107690

Abubakar, A., Al-Wahaibi, Y., Al-Wahaibi, T., Al-Hashmi, A., Al-Ajmi, A., and Eshrati, M. (2015). Effect of low interfacial tension on flow patterns , pressure gradients and holdups of medium-viscosity oil / water flow in horizontal pipe. *Experimental Thermal and Fluid Science*, 68, 58–67. https://doi.org/10.1016/j.expthermflusci.2015.02.017

Abudu, A., and Goual, L. (2009). Adsorption of crude oil on surfaces using quartz crystal microbalance with dissipation (QCM-D) under flow conditions. *Energy and Fuels*, 23(3), 1237–1248. https://doi.org/10.1021/ef800616x

Adams, J. J. (2014). Asphaltene adsorption, a literature review. *Energy and Fuels*, 28(5), 2831–2856. https://doi.org/10.1021/ef500282p

Agrawala, M., and Yarranton, H. W. (2001). An asphaltene association model analogous to linear polymerization. *Industrial and Engineering Chemistry Research*, 40(21), 4664–4672. https://doi.org/10.1021/ie0103963

Ahmed, S. A., and John, B. (2018). Liquid—Liquid horizontal pipe flow—A review. *Journal of Petroleum Science and Engineering*, 168(April), 426–447. https://doi.org/10.1016/j.petrol.2018.04.012

Akbarzadeh, K., Alboudwarej, H., Svrcek, W. Y., and Yarranton, H. W. (2005). A generalized regular solution model for asphaltene precipitation from n-alkane diluted heavy oils and bitumens. *Fluid Phase Equilibria*, 232(1–2), 159–170. https://doi.org/10.1016/j.fluid.2005.03.029

Akbarzadeh, K., Eskin, D., Ratulowski, J., and Taylor, S. (2011). Asphaltene deposition measurement and modeling for flow assurance of subsea tubings and pipelines. *Proceedings of the Annual Offshore Technology Conference*, 1, 256–264. https://doi.org/10.4043/22316-ms

Alboudwarej, H., Beck, J., Svrcek, W. Y., Yarranton, H. W., and Akbarzadeh, K. (2002). Sensitivity of asphaltene properties to separation techniques. *Energy and Fuels*, 16(2), 462–469. https://doi.org/10.1021/ef010213p

Alboudwarej, H., Pole, D., Svrcek, W. Y., and Yarranton, H. W. (2005). Adsorption of asphaltenes on metals. *Industrial and Engineering Chemistry Research*, 44(15), 5585–5592. https://doi.org/10.1021/ie048948f

Alhosani, A., and Daraboina, N. (2020). Unified Model to Predict Asphaltene Deposition in Production Pipelines. *Energy and Fuels*, 34(2), 1720–1727. https://doi.org/10.1021/acs.energyfuels.9b04287

Al-Wahaibi, T., Al-Wahaibi, Y., Al-Ajmi, A., Al-Hajri, R., Yusuf, N., Olawale, A. S., and Mohammed, I. A. (2014). Experimental investigation on flow patterns and pressure gradient through two pipe diameters in horizontal oil–water flows. *Journal of Petroleum Science and Engineering*, 122, 266–273. https://doi.org/10.1016/j.petrol.2014.07.019

Al-Wahaibi, T., Yusuf, N., Al-Wahaibi, Y., and Al-Ajmi, A. (2012). Experimental study on the transition between stratified and non-stratified horizontal oil-water flow. *International Journal of Multiphase Flow*, 38(1), 126–135. https://doi.org/10.1016/j.ijmultiphaseflow.2011.08.007

Angeli, P., and Hewitt, G. F. (1999). Pressure gradient in horizontal liquid-liquid flows. *International Journal of Multiphase Flow*, 24(7), 1183–1203. https://doi.org/10.1016/S0301-9322(98)00006-8

Angeli, P., Hewitt, G.F., 1998. Pressure gradient in horizontal liquid–liquid flows. *Int. J. Multiphas. Flow* 24, 1183–1203.

Ashtari, M., Carbognani Ortega, L., Lopez-Linares, F., Eldood, A., and Pereira-Almao, P. (2016). New Pathways for Asphaltenes Upgrading Using the Oxy-Cracking Process. *Energy and Fuels*, 30(6), 4596–4608. https://doi.org/10.1021/acs.energyfuels.6b00385

B.-Y. Zhu, T. Gu, Reverse hemimicelle formation of 1-decanol from heptane at the solution/graphite interface, *Colloids and Surfaces* 46 (1990) 339–345. https://doi.org/10.1016/0166-6622(90)80175-4.

Bai, R., Chen, K., and Joseph, D. D. (1992). Lubricated pipelining: Stability of core—Annular flow. Part 5. Experiments and comparison with theory. *Journal of Fluid Mechanics*, 240(March), 97–132. https://doi.org/10.1017/S0022112092000041

Balabin, R. M., Syunyaev, R. Z., Schmid, T., Stadler, J., Lomakina, E. I., and Zenobi, R. (2011). Asphaltene adsorption onto an iron surface: Combined near-infrared (NIR), Raman, and AFM study of the kinetics, thermodynamics, and layer structure. *Energy and Fuels*, 25(1), 189–196. https://doi.org/10.1021/ef100779a

Bambinek, K., Przyjazny, A., and Boczkaj, G. (2023). Compatibility of Crude Oil Blends─Processing Issues Related to Asphaltene Precipitation, Methods of Instability Prediction─A Review. *Industrial and Engineering Chemistry Research*, 62(1), 2–15. https://doi.org/10.1021/acs.iecr.2c02532

Bannwart, A. C. (1998). Wavespeed and volumetric fraction in core annular flow. International *Journal of Multiphase Flow*, 24(6), 961–974. https://doi.org/10.1016/S0301-9322(98)00019-6

Bannwart, A. C. (2001). Modeling aspects of oil-water core-annular flows. *Journal of Petroleum Science and Engineering*, 32(2–4), 127–143. https://doi.org/10.1016/S0920-4105(01)00155-3

Bannwart, A. C., Rodriguez, O. M. H., Carvalho, C. H. M., Wang, I. S., and Vara, R. M. O. (2004). *Flow Patterns in Heavy Crude Oil-Water Flow*. 126(September). https://doi.org/10.1115/1.1789520

Barrera, D. M., Ortiz, D. P., and Yarranton, H. W. (2013). Molecular weight and density distributions of asphaltenes from crude oils. *Energy and Fuels*, 27(5), 2474–2487. https://doi.org/10.1021/ef400142v

Broseta, D., Robin, M., Savvidis, T., Fejean, C., Durandeau, M., and Zhou, H. (2000). Detection of Asphaltene Deposition by Capillary Flow Measurements. *SPE Journal*, 1–9. https://doi.org/10.2523/59294-ms

Calles, J. A., Dufour, J., Marugán, J., Peña, J. L., Giménez-Aguirre, R., and Merino-García, D. (2008). Properties of asphaltenes precipitated with different n-Alkanes. A study to assess the most representative species for modeling. *Energy and Fuels*, 22(2), 763–769. https://doi.org/10.1021/ef700404p

Casas, Y. (2017). Settling Rates of Asphaltenes and Solids from Diluted Bitumen. 168. https://doi.org/10.11575/PRISM/27763

Castellanos Díaz, O., Modaresghazani, J., Satyro, M. A., and Yarranton, H. W. (2011). Fluid Phase Equilibria Modeling the phase behavior of heavy oil and solvent mixtures. *Fluid Phase Equilibria*, 304(1–2), 74–85. https://doi.org/10.1016/j.fluid.2011.02.01

Chacón-Patiño, M. L.; Smith, D. F.; Hendrickson, C. L.; Marshall, A. G.; Rodgers, R. P. Advances in Asphaltene Petroleomics. Part 4. Compositional Trends of Solubility Subfractions Reveal that Polyfunctional Oxygen-Containing Compounds Drive Asphaltene Chemistry. *Energy and Fuels*, 2020, 34, 3013−3030.

Chaisoontornyotin, W., Haji-Akbari, N., Fogler, H. S., and Hoepfner, M. P. (2016). Combined Asphaltene Aggregation and Deposition Investigation. *Energy and Fuels*, 30(3), 1979–1986. https://doi.org/10.1021/acs.energyfuels.5b02427

Cortes, F. B., Montoya, T., Acevedo, S., Nassar, N. N., and Franco, C. A. (2016). Adsorption-desorption of n-C7 asphaltenes over micro- and nanoparticles of silica and its impact on wettability alteration. *CTyF - Ciencia, Tecnologia y Futuro*, 6(4), 89–106. https://doi.org/10.29047/01225383.06

da Silva Oliveira E, Neto Á, Júnior, V;Castro, E, de, Menezes S de (2014) Study of Brazilian asphaltene aggregation by nuclear magnetic resonance spectroscopy. *Fuel* 117:146–151

Dickie, J. P.; Yen, T. F. Macrostrucutres of asphaltic fractions by various instrumental methods. *Anal. Chem.* 1967, 39, 1847–1852.

Do, N., Gomez, M. A., Schoeggl, F. F., and Yarranton, H. W. (2022). Investigation of Asphaltene Deposition in Horizontal Flow above and below the Heavy-Phase Glass Transition. *Energy and Fuels*, 36, 14113–14127. https://doi.org/10.1021/acs.energyfuels.2c02957

Ducker, W. A., Senden, T., Pashley, R. M. (1992). Measurement Of Forces In Liquids Using a Force Microscope. *Langmuir*, 7(8), 1831-1836. https://doi.org/10.1021/la00043a024

Duran, J. A., Casas, Y. A., Xiang, L., Zhang, L., Zeng, H., and Yarranton, H. W. (2018). Nature of Asphaltene Aggregates. *Energy and Fuels*, 33(5), 3694–3710. https://doi.org/10.1021/acs.energyfuels.8b03057

Duran, J. A., Schoeggl, F. F., and Yarranton, H. W. (2019). Kinetics of asphaltene precipitation/aggregation from diluted crude oil. *Fuel*, 255(July), 115859. https://doi.org/10.1016/j.fuel.2019.115859

Elseth, G. (2001). An experimental Study of Oil/Water Flow in Horizontal Pipes.

Eskin, D., Ratulowski, J., Akbarzadeh, K., and Lindvig, T. (2009). An approach to the prediction of wax and asphaltene deposition in a pipeline based on Couette device experimental data. 85–97. https://doi.org/10.2495/MPF090081

Eskin, D., Ratulowski, K., Akbarzadeh, K., and Andersen, S. (2011). Modeling of Asphaltene Deposition in a Production Tubing. *AIChE Journal*, 58(9), 2936–2948. https://doi.org/10.1002/aic.12800

Fahim, M. A., Al- Sahhaf, T. A., and Elkilani, A. 2009. Fundamentals of Petroleum Refining. Amsterdam, *The Netherlands: Elsevier*.

Ferworn, K.A., Svrcek, W.Y., Mehrotra, A.K., 1993. Measurement of asphaltene particle size distributions in crude oils diluted with n-heptane. Industrial and Engineering Chemistry Research 32, 955.

Gray, M. R., Tykwinski, R. R., Stryker, J. M., and Tan, X. (2011). Supramolecular assembly model for aggregation of petroleum asphaltenes. *Energy and Fuels*, 25(7), 3125–3134. https://doi.org/10.1021/ef200654p

Gray, M. R., Yarranton, H. W., Chacón-Patiño, M. L., Rodgers, R. P., Bouyssiere, B., and Giusti, P. (2021). Distributed Properties of Asphaltene Nanoaggregates in Crude Oils: A Review. *Energy and Fuels*, 35(22), 18078–18103. https://doi.org/10.1021/acs.energyfuels.1c01837

Gray, M.R. (2015). Upgrading Oilsands Bitumen and Heavy Oil

Grimaldos Aguilar, F. A. (2018). Measurement of Liquid-Liquid Diffusion in Solvent-Bitumen Systems.

Guan, Q., Yap, Y. F., Goharzadeh, A., Vargas, F. M., and Chapman, W. G. (2017). Asphaltene Deposition in Wellbores / Pipelines. *IEEE*.

Guo, J., Yang, Y., Zhang, S., Zhang, D., Cao, C., Ren, B., Liu, L., Xing, Y., and Xiong, R. (2018). Journal of Petroleum Science and Engineering Heavy oil-water fl ow patterns in a small diameter vertical pipe under high temperature / pressure conditions. *Journal of Petroleum Science and Engineering*, 171, 1350–1365. https://doi.org/10.1016/j.petrol.2018.08.021

H. Foroughi, M. Kawaji, Viscous oil–water flows in a microchannel initially saturated with oil: Flow patterns and pressure drop characteristics, *Int. J. Multiph. Flow*.

Hanafizadeh, P., Hojati, A., and Karimi, A. (2015). Experimental investigation of oil-water two phase flow regime in an inclined pipe. *Journal of Petroleum Science and Engineering*, 136, 12–22. https://doi.org/10.1016/j.petrol.2015.10.031

Hoepfner, M. P., Limsakoune, V., Chuenmeechao, V., Maqbool, T., and Scott Fogler, H. (2013). A fundamental study of asphaltene deposition. *Energy and Fuels*, 27(2), 725–735. https://doi.org/10.1021/ef3017392

Hong, E., and Watkinson, A. P. (2009). Precipitation and fouling in heavy oil-diluent blends. *Heat Transfer Engineering*, 30(10–11), 786–793. https://doi.org/10.1080/01457630902744143

Huang, Z., Lee, H. S., Senra, M., and Fogler, H. S. (2011). A fundamental model of wax deposition in subsea oil pipelines. *AIChE Journal*, 57(11), 2955–2964. https://doi.org/10.1002/aic

Ibarra, R., Matar, O. K., Markides, C. N., and Zadrazil, I. (2015). An experimental study of oil-water flows in horizontal pipes. *BHR Group - 17th International Conference on Multiphase Technology* 2015, November, 169–184.

Israelachvili, J., Min, Y., Akbulut, M., Alig, A., Carver, G., Greene, W., Kristiansen, K., Meyer, E., Pesika, N., Rosenberg, K., and Zeng, H. (2010). Recent advances in the surface forces apparatus (SFA) technique. *Reports on Progress in Physics*, 73(3), 036601. https://doi.org/10.1088/0034-4885/73/3/036601

Johnston, K. A., Schoeggl, F. F., Satyro, M. A., Taylor, S. D., and Yarranton, H. W. (2017). Phase behavior of bitumen and n-pentane. *Fluid Phase Equilibria*, 442, 1–19. https://doi.org/10.1016/j.fluid.2017.03.001

Kord S, Mohammadzadeh O, Miri R, Soulgani BS. Further investi- gation into the mechanisms of asphaltene deposition and per- meability impairment in porous media using a modified ana- lytical model. *Fuel*. 2014;117:259–68. https ://doi.org/10.1016/j. fuel.2013.09.038.

Kosior, D., Ngo, E., and Dabros, T. (2016). Determination of the Settling Rate of Aggregates Using the Ultrasound Method during Paraffinic Froth Treatment. *Energy and Fuels*, 30(10), 8192–8199. https://doi.org/10.1021/acs.energyfuels.6b01714

Kuang, J., Tavakkoli, M., Yarbrough, J., Wang, J., Jain, S., Ashtekar, S., Abdallah, D. S., Punnapala, S., and Vargas, F. M. (2018). Investigation of Asphaltene Deposition at High Temperature and under Dynamic Conditions. *Energy and Fuels*, 32(12), 12405–12415. https://doi.org/10.1021/acs.energyfuels.8b03318

Kurup, A. S., Vargas, F. M., Wang, J., Buckley, J., Creek, J. L., Subramani, H. J., and Chapman, W. G. (2011). Development and application of an asphaltene deposition tool (ADEPT) for well bores. *Energy and Fuels*, 25(10), 4506–4516. https://doi.org/10.1021/ef200785v

Kurup, A. S., Wang, J., Subramani, H. J., Buckley, J., Creek, J. L., and Chapman, W. G. (2012). Revisiting asphaltene deposition tool (ADEPT): Field application. *Energy and Fuels*, 26(9), 5702–5710. https://doi.org/10.1021/ef300714p

Liu, F., Hickman, S., Maqbool, T., Pauchard, V., and Banerjee, S. (2020). Study of Asphaltene Deposition onto Stainless-Steel Surfaces Using Quartz Crystal Microbalance with Dissipation. *Energy and Fuels*, 34(8), 9283–9295. https://doi.org/10.1021/acs.energyfuels.0c00663

Mancilla-Polanco, A., Johnston, K., Richardson, W. D. L., Schoeggl, F. F., Zhang, Y., Yarranton, H. W., and Taylor, S. D. (2019). *Phase Behavior of Heavy-Oil / Propane Mixtures. SPE Journal*, February 2017, 596–617.

Maqbool, T., Raha, S., Hoepfner, M. P., and Fogler, H. S. (2011). Modeling the aggregation of asphaltene nanoaggregates in crude oil-precipitant systems. *Energy and Fuels*, 25(4), 1585–1596. https://doi.org/10.1021/ef1014132

Mendoza de la Cruz, J. L., Castellanos-Ramírez, I. V., Ortiz-Tapia, A., Buenrostro-González, E., Durán-Valencia, C. de los A., and López-Ramírez, S. (2009). Study of monolayer to multilayer adsorption of asphaltenes on reservoir rock minerals. *Colloids and Surfaces A: Physicochemical and Engineering Aspects*, 340(1–3), 149–154. https://doi.org/10.1016/j.colsurfa.2009.03.021

Mofidi, A. M., Edalat, M. (2006). A simplified thermodynamic modeling procedure for predicting asphaltene precipitation. https://doi.org/10.1016/j.fuel.2006.05.019 *Fuel*, 85(17–18), 2616–2621.

Moir, M. E. *The Quantum Mechanics of Asphaltene Aggregation. In Chemistry Solutions to Challenges in the Petroleum Industry*; Parviz, R., Ovalles, C., Zhang, Y., Adams, J. J., Eds.; American Chemical Society (ACS): Washington, D.C., 2019; ACS Symposium Series, Vol. 1320, Chapter 5, pp 89−111, DOI: 10.1021/ bk-2019-1320.ch005.

Motahhari, H., Satyro, M. A., Taylor, S. D., and Yarranton, H. W. (2013). Extension of the expanded fluid viscosity model to characterized oils. *Energy and Fuels*, 27(4), 1881–1898. https://doi.org/10.1021/ef301575n

Mullins, O. C. (2010). The modified yen model. *Energy and Fuels*, 24(4), 2179–2207. https://doi.org/10.1021/ef900975e

Mullins, O. C. (2011). The asphaltenes. Annual Review of Analytical Chemistry, 4, 393–418. https://doi.org/10.1146/annurev-anchem-061010-113849

Murgich, J. (2002). Intermolecular forces in aggregates of asphaltenes and resins. *Petroleum Science and Technology*, 20(9–10), 983–997. https://doi.org/10.1081/LFT-120003692

Mydlarz-Gabryk, K., Pietrzak, M., and Troniewski, L. (2014). Study on oil-water two-phase upflow in vertical pipes. *Journal of Petroleum Science and Engineering*, 117, 28–36. https://doi.org/10.1016/j.petrol.2014.03.007

Nabzar, L., and Aguilera, M. E. (2008). The Colloidal Approach. A promising Route for Asphaltene Deposition Modeling. *Oil and Gas Science and Technology*, 63(1), 21–35. https://doi.org/10.2516/ogst

Natarajan, A., Kuznicki, N., Harbottle, D., Masliyah, J., Zeng, H., and Xu, Z. (2014). Understanding mechanisms of asphaltene adsorption from organic solvent on mica. *Langmuir*, 30(31), 9370–9377. https://doi.org/10.1021/la500864h

Nguyen, D. D., Daneshfar, R., Dehaghani, A. H. S., and Su, C. H. (2020). The effect of shear rate on aggregation and breakage of asphaltenes flocs: Experimental study and model-based analysis. *Journal of Molecular Liquids*, 325. https://doi.org/10.1016/j.molliq.2020.114861

Ortega-Rodriguez, A., Cruz, S. A., Garcia-Cruz, I., and Lira-Galeana, C. (2016). Study of the Adhesion Force of Asphaltene Aggregates to Metallic Surfaces of Fe and Al. *Energy and Fuels*, 30(5), 3596–3604. https://doi.org/10.1021/acs.energyfuels.5b02065

Osundare, O. S., Falcone, G., Lao, L., and Elliott, A. (2020). Liquid-liquid flow pattern prediction using relevant dimensionless parameter groups. *Energies*, 13(17). https://doi.org/10.3390/en13174355

Paniagua Fernandez. (2021). Determination of Solubility Parameter of Methane in Heavy Oil. University of Calgary.

Paolinelli, L. D., Rashedi, A., Yao, J., and Singer, M. (2018). Study of water wetting and water layer thickness in oil-water flow in horizontal pipes with different wettability. *Chemical Engineering Science*, 183, 200–214. https://doi.org/10.1016/j.ces.2018.03.023

Parsaei, R., Kazemzadeh, Y., and Riazi, M. (2020). Study of Asphaltene Precipitation during CO2 Injection into Oil Reservoirs in the Presence of Iron Oxide Nanoparticles by Interfacial Tension and Bond Number Measurements. *ACS Omega*, 5(14), 7877–7884. https://doi.org/10.1021/acsomega.9b04090

Perez Claro, Y. A., Schoeggl, F. F., Taylor, S. D., and Yarranton, H. W. (2019). Phase Behavior of Mixtures of Bitumen and n-Butane. *Energy and Fuels*, 33(9), 8530–8543. https://doi.org/10.1021/acs.energyfuels.9b02113

Piroozian, A., Hemmati, M., Ismail, I., Manan, M. A., Rashidi, M. M., and Mohsin, R. (2017). An experimental study of flow patterns pertinent to waxy crude oil-water two-phase flows. *Chemical Engineering Science*, 164, 313–332. https://doi.org/10.1016/j.ces.2017.02.026

Rahmani, N. H. G. (2005). Shear-induced growth of asphaltene aggregates. Library and Archives Canada = Bibliothèque et Archives Canada.

Rahmani, N. H. G., Dabros, T., and Masliyah, J. H. (2005). Settling properties of asphaltene aggregates. *Energy and Fuels*, 19(3), 1099–1108. https://doi.org/10.1021/ef0496707

Ramírez-Corredores, M. M. (2017). Asphaltenes. *The Science and Technology of unconventional oils: Finding refining opportunities. Elsevier* ; Academic Press, an imprint of Elsevier.

Ramirez-Jaramillo, E., Lira-Galeana, C., and Manero, O. (2006). Modeling asphaltene deposition in production pipelines. *Energy and Fuels*, 20(3), 1184–1196. https://doi.org/10.1021/ef050262s

Ramos-Pallares, F., and Yarranton, H. W. (2020). Extending the Modified Regular Solution Model to Predict Component Partitioning to the Asphaltene-Rich Phase. *Energy and Fuels*, 34(5), 5213–5230. https://doi.org/10.1021/acs.energyfuels.9b03489

Rastegari, K., Svrcek, W. Y., and Yarranton, H. W. (2004). Kinetics of asphaltene flocculation. *Industrial and Engineering Chemistry Research*, 43(21), 6861–6870. https://doi.org/10.1021/ie049594v

Rodriguez, O. M. H., and Bannwart, A. C. (2006). Experimental study on interfacial waves in vertical core flow. *Journal of Petroleum Science and Engineering*, 54(3–4), 140–148. https://doi.org/10.1016/j.petrol.2006.07.007

Rudrake, A., Karan, K., and Horton, J. H. (2009). A combined QCM and XPS investigation of asphaltene adsorption on metal surfaces. *Journal of Colloid and Interface Science*, 332(1), 22—31. https://doi.org/10.1016/j.jcis.2008.12.052

Sabbagh, O., Akbarzadeh, K., Badamchi-Zadeh, A., Svrcek, W.Y., and Yarranton, H.W. (2006) *Energy and Fuels*, 20 (2): 625–634

Saryazdi, F., Motahhari, H., Schoeggl, F. F., Taylor, S. D., and Yarranton, H. W. (2013). Density of hydrocarbon mixtures and bitumen diluted with solvents and dissolved gases. *Energy and Fuels*, 27(7), 3666–3678. https://doi.org/10.1021/ef400330j

Seifried, C. M., Crawshaw, J., and Boek, E. S. (2013). Kinetics of asphaltene aggregation in crude oil studied by confocal laser-scanning microscopy. *Energy and Fuels*, 27(4), 1865–1872. https://doi.org/10.1021/ef301594j

Semple, K. M.; Cyr, N.; Fedorak, P. M.; Westlake, D. W. Characterization of asphaltenes from Cold Lake heavy oil: Variations in chemical structure and composition with molecular size. Can. *J. Chem*. 1990, 68 (7), 1092−1099

Shirokoff, J. W., Siddiqui, M. N., and Ali, M. F. (1997). Characterization of the structure of Saudi crude asphaltenes by X-ray diffraction. *Energy and Fuels*, 11(3), 561–565. https://doi.org/10.1021/ef960025c

Sirota, E. B. (2005). Physical structure of asphaltenes. *Energy and Fuels*, 19(4), 1290–1296. https://doi.org/10.1021/ef049795b

Solaimany-Nazar, A. R., and Rahimi, H. (2008). Dynamic determination of asphaltene aggregate size distribution in shear induced organic solvents. *Energy and Fuels*, 22(5), 3435–3442. https://doi.org/10.1021/ef800173s

Soleimani-Khormakala, H., Torkaman, M., and Bahrami, M. (2018). The Effect of Shear Rate on Aggregation and Fragmentation of Asphaltene Aggregates. *Journal of Dispersion Science and Technology*, 40(6), 836–845. https://doi.org/10.1080/01932691.2018.1485579

Speight, J. G. (2004). Asphaltenes and the Structure of Petroleum. *Petroleum Chemistry And Refining*, 59(5), 117–134. https://doi.org/10.1201/9781482229349-11.

Speight, J. G. (2006). The Chemistry and Technology of Petroleum. In CRC (4th ed.). https://doi.org/10.1201/b16559

Speight, J. G. (2019). Heavy Oil, Extra Heavy Oil, and Tar Sand Bitumen. *In Heavy Oil Recovery and Upgrading* (pp. 3–47). Elsevier. https://doi.org/10.1016/b978-0-12-813025-4.00001-5

Strausz, O. P., and Lown, E. M. (2003). The Chemistry of Alberta Oil Sands, Bitumens and Heavy Oils. Calgary: Alberta Energy Research Institute.

Tharanivasan - A.K., Asphaltene precipitation from crude oil blends , conventional oils, and oils with emulsified water, Dr. Thesis (in Philosophy), University of Calgary, Canada, 211 P.2012,

Ting, P. D., Hirasaki, G. J., and Chapman, W. G. (2003). Modeling of asphaltene phase behavior with the SAFT equation of state. *Petroleum Science and Technology*, 21(3–4), 647–661. https://doi.org/10.1081/lft-120018544

Vargas, F. M., Creek, J. L., and Chapman, W. G. (2010). On the development of an asphaltene deposition simulator. *Energy and Fuels*, 24(4), 2294–2299. https://doi.org/10.1021/ef900951n

Vilas Bôas Fávero, C., Hanpan, A., Phichphimok, P., Binabdullah, K., and Fogler, H. S. (2016). Mechanistic Investigation of Asphaltene Deposition. *Energy and Fuels*, 30(11), 8915–8921. https://doi.org/10.1021/acs.energyfuels.6b01289

Vuong, D. H., Zhang, H.-Q., Sarica, C., and Li, M. (2009). Experimental Study on High Viscosity Oil/Water Flow in Horizontal and Vertical Pipes. *In SPE Annual Technical Conference and Exhibition* (p. SPE-124542-MS). https://doi.org/10.2118/124542-MS

W.G. Chapman, K.E. Gubbins, G. Jackson, M. Radosz. SAFT: Equation-of-state solution model for associating fluids, *Fluid Phase Equilibria*, Volume 52, 1989,Pages 31-38, ISSN 0378-3812, https://doi.org/10.1016/0378-3812(89)80308-5.

Wang, J., Buckley, J. S., and Creek, J. L. (2004). Asphaltene deposition on metallic surfaces. *Journal of Dispersion Science and Technology*, 25(3), 287–298. https://doi.org/10.1081/DIS-120037697

Wang, S., Liu, J., Zhang, L., Masliyah, J., and Xu, Z. (2010). Interaction forces between asphaltene surfaces in organic solvents. *Langmuir*, 26(1), 183–190. https://doi.org/10.1021/la9020004

Watkinson, A. P. (2007). Deposition from crude oils in heat exchangers. *Heat Transfer Engineering*, 28(3), 177–184. https://doi.org/10.1080/01457630601064413

Xie, K., and Karan, K. (2005). Kinetics and thermodynamics of asphaltene adsorption on metal surfaces: A preliminary study. *Energy and Fuels*, 19(4), 1252–1260. https://doi.org/10.1021/ef049689+

Xing, C., Hilts, R. W., and Shaw, J. M. (2010). Sorption of athabasca vacuum residue constituents on synthetic mineral and process equipment surfaces from mixtures with pentane. *Energy and Fuels*, 24(4), 2500–2513. https://doi.org/10.1021/ef901297e

Yarranton, H.W., Alboudwarej, H., Jakher, R., "Investigation of Asphaltene Association with Vapour Pressure Osmometry and Interfacial Tension Measurements," Ind. Eng. Chem. Res., 39, (2000), 2916-2924.

Yarranton, H.W., Masliyah, J.H., 1996. Molar mass distribution and solubility modeling of asphaltenes. *A.I.Ch.E. Journal* 42 (12), 3533–3543.

Yarranton, H.W., Ortiz, D.P., Barrera, D.M., Baydak, E.N., Barre, L., Eyssautier, J., Zeng, H., Xu, Z., Dechaine, G., Becerra, M., Shaw, J.M., McKenna, A.M., Mapolelo, M.M., Bohne, C., Yang, Z., Oake, J., "On the Size Distribution of Self-Associated Asphaltenes," *Energy and Fuels*, 27, 2013, 5083-5106.

Zahabi, A., Gray, M. R., and Dabros, T. (2012). Kinetics and properties of asphaltene adsorption on surfaces. *Energy and Fuels*, 26(2), 1009–1018. https://doi.org/10.1021/ef2014698

Zanganeh, P., Ayatollahi, S., Alamdari, A., Zolghadr, A., Dashti, H., Kord, S., 2012. Asphaltene deposition during CO 2 injection and pressure depletion: a visual study. *Energy Fuels* 26, 1412–1419. https://doi.org/10.1021/ef2012744.

Zhang, L. Y.; Lawrence, S.; Xu, Z. H.; Masliyah, J. H. Studies of Athabasca Asphaltene Langmuir Films at Air-Water Interface. *J. Colloid Interface Sci*. 2003, 264 (1), 128−140

Zhang, L., Shi, C., Lu, Q., Liu, Q., and Zeng, H. (2016). Probing Molecular Interactions of Asphaltenes in Heptol Using a Surface Forces Apparatus: Implications on Stability of Water-in-Oil Emulsions. *Langmuir*, 32(19), 4886–4895. https://doi.org/10.1021/acs.langmuir.6b01000

Appendix A: Static Mixer

A static mixer was developed in a previous study (Do *et al*., 2022). The purpose of the static mixer is to promote effective mixing between the prediluted bitumen and *n*-heptane streams. The static mixer is made up of two concentric tubes: a ¼" tube (6.35 mm ID) on the outside and a 1/8" capillary tube (1.75 mm ID) inside, as shown in Figure A.1. Each tube has slits in the ends, and the tube is crimped in to create a venturi effect, which creates a crossflow between the two streams. The fluid with the higher velocity flows through the interior tube and the other through the annular space creating a velocity difference that promotes mixing.

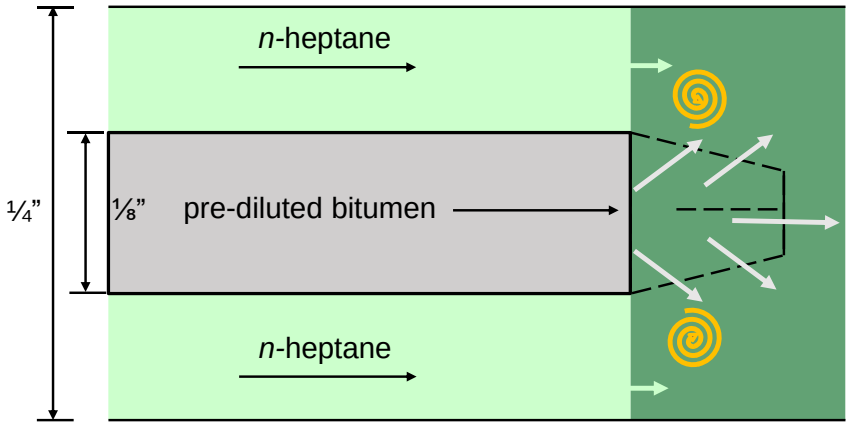

Figure A.1. Schematic of the static mixer. From (Do, 2021).

Do *et al*. (2022) verified the efficiency of the mixing process by measuring the asphaltene yield at the mixer exit and comparing it with the expected equilibrium yield. Poor mixing will generate zones of high solvent content that lead to excess precipitation. There is a hysteresis in asphaltene redissolution and therefore not all of the excess precipitation will reverse when equilibrium is attained. Hence, poor mixing will result in a higher than equilibrium asphaltene yield.

The equilibrium yield was determined as follows. Asphaltenes yields were gravimetrically at room conditions using the procedure from Johnston *et al.* (2017) at three different contact times: 24 hours, five hours, and 30 minutes. The asphaltene yields were then extrapolated to 1 min, the contact time of the static mixer, to obtain a baseline for complete mixing. The asphaltene yields at the distinct contact times and the extrapolated baseline is shown in Figure A.2.

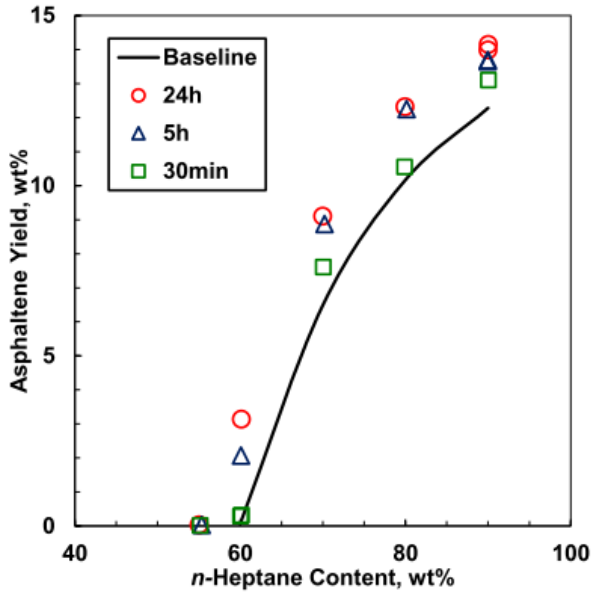

Figure A.2. Asphaltene yield data from *n*-heptane diluted bitumen at three different contact times, and the extrapolated baseline for 1 min contact time (Do *et al*., 2022).

The asphaltene yields in the light phase at the exit from the static mixer were measured in ambient conditions. To do so, the Asphaltene Deposition Apparatus was modified as follows. The lines connecting the static mixer to the differential pressure gauge and other equipment were eliminated. The outlet of the static mixer exposed to the atmosphere was angled downward slightly to facilitate the sample collection process, as shown in Figure A.3. Two samples were collected for solvent compositions ranging from 65 to 90 wt% of the fluid mixture. Two samples were collected for each solvent composition in a 30 mL centrifuge tube. After filling each tube for approximately one minute, the tubes were immediately centrifuged at 4000 rpm for five minutes to separate the heavy phase from the light phase. A sample of the light phase was taken and placed into a separate clean tube. The tubes were then placed inside an 80°C oven for 14 days to evaporate all the solvent in the sample, leaving behind a residue of bitumen (Do *et al.* 2022), and the asphaltene yields were determined from a material balance.

It was found that the asphaltene yields obtained at the outlet of the static mixer were consistent with the extrapolated baseline obtained from benchtop tests to within the experimental error of ±1.0 wt%, based on a 90% confidence interval, as shown in Figure A.4. Hence, there is complete mixing between the prediluted bitumen and solvent by the exit of the static mixer.

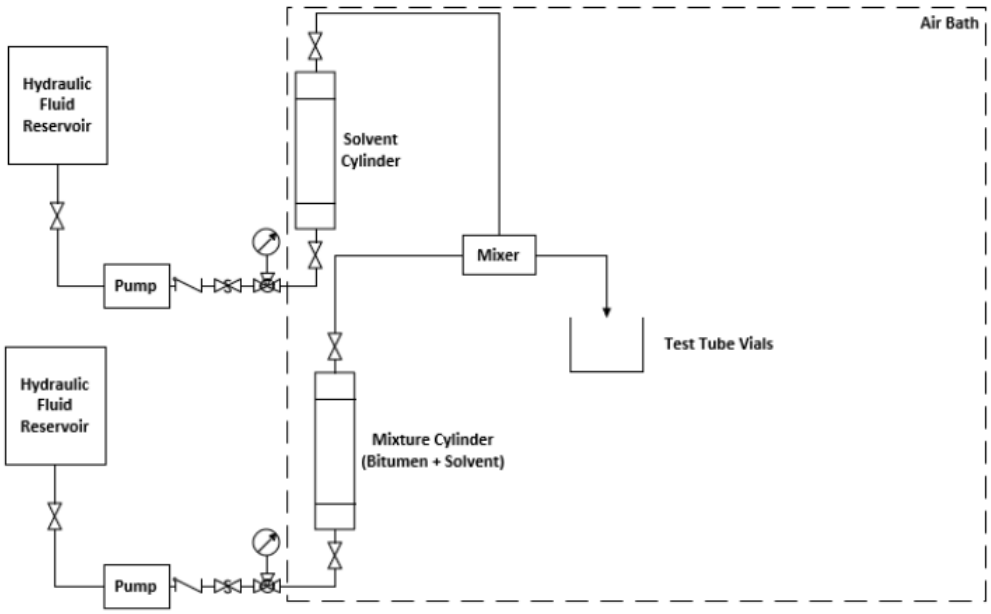

Figure A.3. Modified asphaltene deposition apparatus to measure asphaltene yields from static mixer. Adapted from (Do *et al*., 2022).

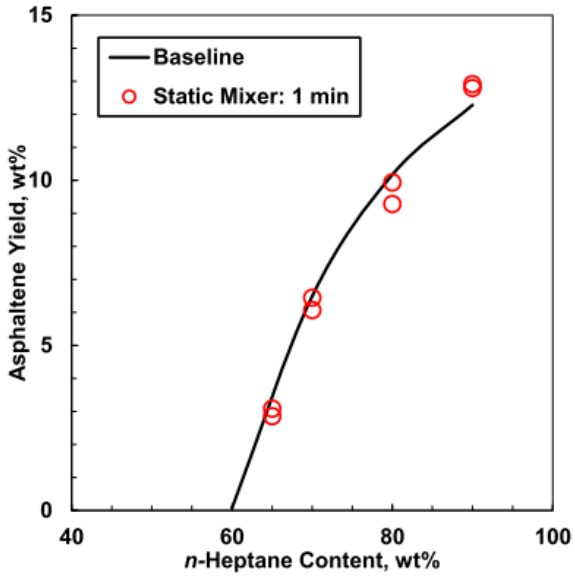

Figure A.4. Comparison of asphaltene yield obtained from static mixer and extrapolated baseline Adapted from (Do *et al.*, 2022),

Appendix B: Modelling of Asphaltene Yield

The Modified Regular Solution (MRS) model was used to predict the asphaltene yield, amount of asphaltene portioning to the heavy phase (Alboudwarej *et al*. 2003; Akbarzadeh *et al*. 2005; Ramos-Pallares and Yarranton, 2020). Briefly, the MRS model is an activity coefficient model for a liquid-liquid equilibrium between the asphaltene rich heavy phase and the solvent-rich light phase. The partition coefficient for a component in the mixture at equilibrium is given by:

$$K_i = \frac{x_i^H}{x_i^L} = \frac{\gamma_i^L}{\gamma_i^H} \tag{B1}$$

where K_i is the partition coefficient for component *i* in the mixture, *x* is the mole fraction, γ is the activity coefficient, and superscript *L* and *H* represent the light and heavy phase.

In the MRS theory, the activity coefficient of component *i* results from an enthalpic contribution arising from a regular solution and an entropic contribution caused by mixing molecules of different sizes. For the light, the activity coefficient is given by:

$$\ln \gamma_i^L = \ln\left(\frac{v_i}{v^L}\right) + 1 - \frac{v_i}{v^L} + \frac{v_i}{RT}(\delta_i - \delta^L)^2 \tag{B.2}$$

where *v* is the molar volume, *R* is the universal gas constant, *T* is the absolute temperature, and δ is the solubility parameter. For the heavy phase, the activity coefficient consists only of the enthalpic component from a regular solution with an ideal entropy of mixing as shown below:

$$\ln \gamma_i^H = \frac{v_i}{RT}(\delta_i - \delta^H)^2 \tag{B.3}$$

The molar volume of the light or heavy phase is given by:

$$v^\alpha = \sum x_i^\alpha v_i \tag{B.4}$$

The solubility parameter of the light or heavy phase is given by:

$$\delta^\alpha = \sum \phi_i^\alpha \delta_i \tag{B.5}$$

where ϕ_i^α is the volume fraction of a component in either the heavy or light phase , calculated as follows:

$$\phi_i^\alpha = \frac{x_i^\alpha v_i}{v^\alpha} \tag{B.6}$$

The inputs for the model are feed composition, molar volume, density and molecular weight, and solubility parameter of each component: bitumen and *n*-heptane. The bitumen is characterized into pseudo-components corresponding to SARA fractions with the asphaltene fraction defined as the

n-pentane insoluble fraction of the oil (C5-asphaltenes). The properties for *n*-alkanes are available from other sources (Yarranton and Ramos-Pallares, 2020). To use the model at a given temperature and pressure, it is necessary to determine the density and solubility parameter of the precipitant and each pseudo-component at those conditions.

The densities of each of the C5-asphaltene pseudo-components is calculated as follows:

$$\rho_{A,i} = \rho_{A,i}^0 - \left(3.1635 - 0.00239\rho_{A,i}^0\right)(T - 298.15) \quad \text{(B.7)}$$

where $\rho_{A,i}$ is the density of the pseudo-component *i* at the temperature of the system *T*, subscript "*A*" indicates any C5-asphaltene pseudo-component and $\rho_{A,i}^0$ is the density of asphaltene pseudo-component *i* at the standard conditions (25°C and 0.1 MPa) and was calculated as follows:

$$\rho_{A,i}^0 = 1047 + 151.4\left[1 - exp\left(-9w_{A,i}\right)\right] \quad \text{(B.8)}$$

where $w_{A,i}$ is the cumulative mass fraction of pseudo-component *i*.

The solubility parameter for each C5-asphaltene pseudo-component is calculated as follows:

$$\delta_{A,i} = \delta_{A,i}^0 - 0.0191(T - 298.15) \quad \text{(B.9)}$$

where $\delta_{A,i}$ is the solubility parameter of the pseudo-component *i* at the temperature of the system T, and $\delta_{A,i}^0$ is the solubility parameter for each C5-asphaltene pseudo-component at standard conditions (25°C and 0.1 MPa) determined from the following empirical distribution (Powers *et al.* 2016):

$$\delta_{A,i}^0 = \delta_{min}^0 + (\delta_{max}^0 - \delta_{min}^0)w_{A,i}^{1.2} \quad \text{(B.10)}$$

where subscripts "*max*" and "*min*" represent the maximum and minimum solubility parameter of the distribution, and $w_{A,i}$ is the mass fraction of pseudo-component *i*. The values of δ_{min}^0 and δ_{max}^0 are determined by fitting the model to experimental yield data. The tuned values of δ_{min}^0 and δ_{max}^0 were calculated previously by (Do *et al.* 2022) and are 19.65 $MPa^{0.5}$ and 20.08 $MPa^{0.5}$, respectively.

After obtaining the solubility parameter, the model can be applied to determine the liquid-liquid equilibrium at different conditions. According to Yarranton and Ramos-Pallares (2021), the MRS model has been able to predict C5-asphaltene and bitumen yields from mixtures of *n*-alkanes with

carbon numbers greater than 4 to within ±1 wt% and ±2 wt% respectively. Figure 3.5 in Chapter 3 shows the modeled C5-asphaltene yields at the experimental conditions considered in this thesis.